UNIVERSITY OF OKLAHOMA

GRADUATE COLLEGE

Development and Application of a Unified Framework for Meso to Synoptic Scale Error Growth Diagnosis and Weather Extremes in Global Numerical Weather Prediction

A DISSERTATION

SUBMITTED TO THE GRADUATE FACULTY

in partial fulfillment of the requirements for the

Degree of

DOCTOR OF PHILOSOPHY

By

SAMUEL P. LILLO
Norman, Oklahoma
2021

Development and Application of a Unified Framework for Meso to Synoptic Scale Error Growth Diagnosis and Weather Extremes in Global Numerical Weather Prediction

A DISSERTATION APPROVED FOR THE
SCHOOL OF METEOROLOGY

BY THE COMMITTEE CONSISTING OF

Dr. David B. Parsons, Chair

Dr. Steven Cavallo

Dr. Jason Furtado

Dr. Elinor Martin

Dr. Nikola Petrov

Dedication

To my mom, dad, and sister.

And every teacher I've had along the way.

Acknowledgments

Not unlike many people who enter the field of meteorology, I have been obsessed with weather since I was five years old. I knew my career path would be in meteorology, but it was not until grad school that I realized all the different routes that one could take in this field, and the role that the rest of life events could play in determining a career path. I am confident that I would be wandering lost at the moment, stuck at one of the intersections or off the road altogether if it weren't for my advisor, David Parsons. His enthusiasm for good science is contagious and it was impossible to not be energized by his presence in the office. Every discussion, ranging from science, to Rutgers sports, or ragging on the Red Sox, to anything New Jersey, and life in general, made the foundation of my graduate school experience. These moments were invaluable, but additionally Dave played a pivotal role in getting me on track to complete this dissertation and earn my doctoral degree. He was there for every hurdle, and I cannot thank him enough.

Steven Cavallo, Jason Furtado, and Elinor Martin, all patient members of my committee, further enhanced my grad school experience. Coming into a school that at the time was known primarily for its severe weather research, I was worried that my love for the larger scale dynamics wouldn't be cultivated. Instead, I was extremely fortunate to have these three amazing scientists join the faculty, with their extensive knowledge and enthusiasm for synoptic to planetary scales and subseasonal-to-seasonal forecasting. Discussions with Steven in our group meetings was often the highlight of the week. The applied statistics and climate dynamics classes I took taught by Jason and Elinor were exceptionally valuable. I would also like to thank Nikola Petrov for serving on my committee throughout every administrative hurdle.

On the subject of administrative hurdles, I had amazing assistance throughout my curvy path toward a doctoral degree. This absolutely would not have been possible without the help of David Parsons, Christie Upchurch, Danika Hines Barnett, Ashley Herndon,

Lindsey Johnston, Jeffrey Basara, and Sherri Irvin. I think I gave them every challenge possible and they were there for me every step of the way.

Much of the work on this dissertation was done, and not done, in the original Arctic and Antarctic Research Group (AAARG) office, including Dylan Lusk, James Russell, Nicholas Szapiro, and Christopher Riedel. Beginning with office basketball games that got us scolded for being too loud, and ending with croquet games spanning the entire 5th floor, there was never any shortage of entertainment with this group. Science discussions were also always fruitful. And I honestly miss the midnights in the office working on assignments that of course were procrastinated to the last minute.

Outside of the office, Jacob Carlin, Nicholas Szapiro, Leah Holland, Sean Waugh and Kyle Thiem became my family away from home in Oklahoma. In Colorado, Manda Chasteen and Bo Huang who had accompanied me at OU, became my quarantine family, along with members of the Boulder Pub Run Club; because nothing compares to running and beer for mental health support. These people were my support group in the final stretches of dissertation writing and the defense.

Throughout my graduate studies, I have thought of every incredible influential teacher and class that I had the great fortune of experiencing. The teachers and schools in my home town of Keene, New Hampshire hold a very special place in my heart. They cultivated my passion for science and math from an early age. My Keene High School science education was especially enhanced by David Lybarger, John Odgers, Cliff Lerner. Additionally I have to thank the entire community of my home town which encouraged a nerdy kid with a snowday prediction website.

Last and certainly not least, thank you Mom and Dad; Penelope and Peter Lillo; and my sister, Sara Lillo. My mom spent two decades as a tutor at an elementary school, and my dad was a manager at a circuit board company. They worked so that I could go to school, and then they came home and provided a loving, encouraging and academic environment for me to grow up in. Puzzles and games, scientific curiosity, and letting me

watch The Weather Channel for hours every day, was how I got where I am now. Mom and Dad, you have been incredibly supportive along the entire way; thank you so much. Finally my sister Sara paved the way for me to take risks. I didn't think I would leave New Hampshire until she moved to Chicago and I realized there was a world to explore. She has had an incredible journey herself, and I have looked up to her the entire way. Sara is now a doctoral student in sociology and for the last few years has been integral support as we run the academic marathon together. I wish you the best of luck in all the amazing things you will do in your life.

Table of Contents

List of Figures

Abstract

While the average skill of medium-range numerical weather prediction (NWP) has steadily improved over the last three decades, there is still considerable variance in day-to-day forecast performance. Much of this variance is contained within a long tail in the distribution that is skewed toward cases with very low skill, often referred to as forecast busts or dropouts. These forecast busts in global models are typically focused on sub-continental scales and can be associated with poorly-predicted high-impact weather events, motivating efforts to understand why these busts occur, how they could be anticipated, and how forecast systems could be improved to reduce their occurrence. This study is a systematic investigation of the variability in both upscale error growth and error propagation in global NWP. Our approach utilizes a framework for diagnosing error growth that begins with a prognostic equation for potential vorticity (PV) error in which non-linear terms have been mathematically eliminated. Following adiabatic flow, a wave equation is derived for the wind and PV error from which diagnostics for wave amplitude, wave activity flux (WAF), and Rossby wave source are defined. These diagnostics are then applied to ten years of deterministic ECMWF forecasts.

Our results show that in the first 24 hours the largest rotational errors at the tropopause are over the central US, and to a lesser extent eastern Asia, during the spring and summer. These errors subsequently expand downstream within the respective waveguides. During the winter, initial error growth shifts to the eastern Pacific. The difference between good an bad medium range deterministic forecasts for Europe is associated with error growth over North Atlantic. To further investigate this issue, MPAS forecast runs are presented for cases during increased MCS activity over the central US during June 2015. This period coincided with the PECAN (Plains Elevated Convection at Night) field campaign and also included multiple forecast busts in the ECMWF model. Applying the PV error tendency equation allows for a detailed examination of contributions to initial upscale error growth that transitions to synoptic-scale error wave activity. The complete framework of PV error

tendency and wave dynamics provides insight into preferred modes of error growth and propagation, and atmospheric configurations that are susceptible to forecast busts.

Two recent extreme weather events; a winter storm over Mexico in 2016 and a cold air outbreak over the Midwest in 2019; are investigated from the context of multiple scales. The Mexico winter storm occurred during an historic El Niño while the internal mid-latitude variability disagreed with canonical Niño climatology. An unprecedented surge of mid-latitude Rossby wave activity played a major role in the severity and predictability of this and other events that winter. The 2019 cold air outbreak was the result of a tropopause polar vortex (TPV) transported out of the Arctic into the United States. Here we look at the sensitivity of the forecast to the initial strength of the TPV by using perturbed simulations with MPAS. The evolution of the structure of the TPV is explained through different sources of diabatic heating, and we find high sensitivity of the cold air outbreak severity and position to the TPV strength. A full climatology of TPV tracks is compared against cold air outbreaks in the United States to establish their connection.

Chapter 1

Introduction

1.1 Numerical Weather Prediction

The concept of forecasting the future state of the atmosphere was first proposed by Bjerknes (1904). This seminal work identified the two conditions necessary for numerical weather prediction (NWP), that to this day are the overarching subjects that dictate model performance: 1) "a sufficiently accurate knowledge of the state of the atmosphere at the initial time," and 2) "a sufficiently accurate knowledge of the laws according to which one state of the atmosphere develops from another."

In 1922, Lewis Fry Richardson published a detailed outline (Richardson 1922) to turn this concept of NWP into a reality. The application of his process to produce a forecast was, however, a failure. Richardson attempted to predict surface pressure changes by way of the continuity equation. The forecast was foiled by largely canceling terms in the calculation of divergence which results in a high sensitivity to numerical and observational errors. Not until the 1940s would there be another pursuit to produce an NWP forecast. Shuman (1989) provides a thorough historical review of the development of NWP over the subsequent several decades. What follows is a summary of this review.

Upon the invention of the first electronic computer completed in 1945, Jules Charney founded the Meteorology Research Group dedicated to solving the problem of NWP. In 1949, Charney proposed a single level equivalent-barotropic model for the prediction of large-scale motions at the 500 hPa level (Charney 1949). In 1954, the Joint Numerical Weather Prediction Unit (JNWPU) was founded as a collaboration between the U.S. Weather Bureau, the Air Weather Service, and the Naval Weather Service. The JNWPU later divided into separate organizations, including the National Meteorological Center (NMC). A year later, the JNWPU adopted the Princeton three-level model and produced the

first operational NWP products. By 1960, these products were besting the skill of manual forecasts (Shuman 1989). The 1960s also featured the development of the first operational baroclinic model (Cressman 1963) and a six-layer model (Shuman and Hovermale 1968).

Increasing grid resolution in the models during the 1970s helped to decrease the error due to finite differencing and led to significant improvements in forecast skill (Shuman 1989). During this time, the models were producing regional forecasts out to three days. The first global model was made operational in 1974 with nine layers and a 2.5^o by 2.5^o latitude-longitude grid spacing (Stackpole 1978). Around this same time, global spectral models were gaining more attention (Bourke 1972; Bourke 1974; McAvaney et al. 1978) in which horizontal variation of variables are represented by a finite Fourier series. At a time when grid resolution was very coarse, the spectral method allowed for much more accurate calculations of the primitive equations, through the use of global functions instead of finite differencing. The NMC also began running forecast models to longer lead times. Medium-range NWP beyond 96 hours made progress in the 1970s through studies of error growth in the planetary-scale forecast (Lambert and Merilees 1978), and in the late 1980s the NMC was running the Medium Range Forecast (MRF) global model operationally out to ten days (Caplan and White 1989).

Improvements to NWP performance, beyond those attributed to model resolution and numerical techniques, came with the representation of unresolved physical processes through parameterization schemes. These processes include radiative, convective, and diffusive effects (Bauer et al. 2015) that act on scales as small as the molecular level. While these scales cannot be explicitly modeled in NWP that covers the globe, the physics impact the larger resolvable scales and thus the accuracy by which a model represents the evolution of the atmosphere. Parameterization schemes provide the aggregate momentum and heating tendencies implicitly from these important unresolvable processes.

In addition to the increased sophistication of the physics and dynamics of models, there has been tremendous advancement in how observations are used to initialize models. Lorenz (1963) showed how forecasts can be highly sensitive to minuscule changes in the initial conditions, thus demonstrating the importance of ideal representation of those initial conditions from the available data. Bengtsson et al. (1981) provides a thorough history of early data assimilation methods. The challenges in initializing a model include highly-variable observation density, asynchronous data, and maintaining physical relationships and balances in the model space. Simple interpolation techniques for a single time step can result in significant errors. Instead it is desirable to adjust existing model space using new data. One technique is known as variational data assimilation which minimizes a cost function to optimize initial conditions using a "first guess" short term forecast from the model (Rabier and Liu 2003). The three dimensional variational (3DVAR) algorithm does this for a single point in time. This restriction became problematic as the availability and use of satellite data exploded, which is asynchronous and not ideally incorporated with 3DVAR. Four dimensional variational data assimilation system (4DVAR; Lewis and Derber 1985; Courtier et al. 1994) provided a solution, by comparing observations at their given time to the full trajectory of the short term forecast.

Still, initial conditions will be imperfect. Following Lorenz's conclusion that the nonlinear atmosphere system will have a finite limit of predictability that is a function of the initial state, there emerged a necessity for quantifying the forecast uncertainty that grew from initial condition uncertainty. The solution was model ensembles, which run several simulations using small perturbations in the initial conditions. Another leading data assimilation technique is the ensemble Kalman filter (EnKF; Evensen 1994; Daley 1992) which takes into account the uncertainty in the short term forecast with a probability distribution (prior) and uses observations and their associated uncertainty to produce updated initial conditions and corresponding probability distribution (posterior). EnKF also has the ability to use flow-dependent background error covariances which is an advantage over the

variational methods. 4DVAR and EnKF are two particular techniques that, combined with the growth of computational capabilities, have paved the way for improved NWP performance. There is also the problem of model imperfections that are introduced by all of the limitations and approximations discussed above. Ensembles can thus be formed by mixing the parameterization schemes they employ, the parameters within those schemes, and even the order in which they are called (Donahue and Caldwell 2018). Once again we run into the limitation of computational resources that dictates the size of the ensemble; how many members with unique combinations of perturbed initial conditions and model physics. And as models become more sophisticated, there is a greater need for robust ensembles. The valuable application of ensembles in assessing predictability and forecast confidence will be discussed in the next section.

1.2 Predictability

With the growing complexity of forecast models through the decades, there is particular importance in understanding the source and behavior of errors, defined as a deviation of the forecast from the verifying atmosphere. One of the first systematic studies of error in NWP was Cressman and Hubert (1957). While the focus is on sources of numerical errors that were more problematic 60 years ago, the discussion on error growth and impact in the context of synoptic features is still very relevant today. Edward Lorenz made significant impacts in the field of predictability. Lorenz (1963) used a simple model of atmospheric convection to demonstrate how small errors could lead to a degradation of predictability across the whole domain. Lorenz (1969) introduced deterministic chaos and "the butterfly effect." Using a spectral turbulence model, he showed that errors on small spatial scales grow (and saturate) faster than on large scales, thus eventually overwhelming the entire system. Lorenz (1982) further discussed limits to the predictability of weather systems using 100 days of forecasts from the European Centre for Medium Range Forecasts (ECMWF). By comparing the growth of differences in successive forecasts, he estimated the effective

limitations of error growth within a one-day period on the rest of the forecast. Simmons et al. (1995) applied the Lorenz 1982 methodology to perform a study of forecasts between 1980 and 1994. By extrapolating the improvements in the one day forecast over the period of study, they used Lorenz's error growth model to predict the extent to which improvements may be made to medium range forecast skill, at different levels of the troposphere and across a range of spatial scales.

The limit of predictability is given by the time interval for two initially similar states of the atmosphere to diverge beyond some threshold variance. This limit varies by scales of atmospheric motion. For example, we can predict the placement of synoptic troughs and ridges several days in advance, but the predictability of individual thunderstorms is confined to minutes to hours. There are two types of predictability assessments for NWP. The first is the limit to which a given NWP system can accurately predict a future state of atmosphere. This is referred to as practical predictability (Melhauser and Zhang 2012), and is what we commonly see assessed for individual deterministic forecast models in terms of anomaly correlation coefficient (ACC; Eq. 2.21) or root mean square error (RMSE; Eq. 2.22). Through improvements in observations, data assimilation, computing power, and the model itself, practical predictability has steadily increased over decades (Fig. 1.1).

The second type of predictability limit is known as intrinsic predictability, which is the limit to which the atmosphere can be accurately predicted given an optimal forecast system and optimal initial conditions (Lorenz 1969). Intrinsic predictability is assessed using ensembles; for example, identical-twin experiments which are two or more model runs initialized with minor perturbations (Tribbia and Baumhefner 2004; Zhang et al. 2007a; Selz and Craig 2015; Judt 2018). The spread in the ensemble, or the error between the control and perturbed runs in an identical-twin experiment, is in indication of the predictability of that particular atmospheric flow configuration. As such, intrinsic predictability is an inherent characteristic of the atmosphere and not modifiable by a given NWP system.

Model ensembles give insight into the intrinsic predictability of given forecast scenario by the spread amongst the different members. Smaller spread indicates that the perturbations in the initial conditions and in the model have little effect on the evolution of the forecast suggesting high predictability. In operations, this is used to invoke higher confidence in the forecast. One metric for examining the performance of an ensemble is the spread-error ratio which compares the inferred intrinsic predictability to practical predictability. For operational purposes, it is desired to have a spread-error ratio close to unity. An ensemble with a ratio less than one, i.e. less spread than error, is said to be underdispersed. A ratio greater than one is overdispersed. The former is a great challenge in NWP, where computational resources limit the possible number of members of an ensemble system. The latest ECMWF ensemble spread-error ratio is near unity (Rodwell et al. 2018), but this relationship can vary across individual events. Particularly, events involving intense convection are associated with underdispersed ensemble forecasts due to the approximations in convective parameterization (Clarke et al. 2019b). For any given forecast, the ability of an ensemble to anticipate its own error is a great utility, and is typically assessed by the correlation of spread to error. The strength of the spread-error relationship varies by lead-time, and is greatest after the first few days but before both the spread and error begin to saturate on planetary scales (Whitaker and Loughe 1998; Scherrer et al. 2004; Hopson 2014). As such, the medium-range forecast would typically come with the greatest a priori knowledge of expected performance. It is the instances in which ensembles portray high confidence but deterministic NWP fails that are the most negatively impactful, and dangerous, in operations.

1.3 The Medium-Range Bust Problem

Assessment of the performance of NWP is often done through a running time-mean of hemisphere-wide statistics. Upgrades made in NWP have improved overall forecast statistics, for example increasing global annually-averaged 500 hPa height ACC as shown in

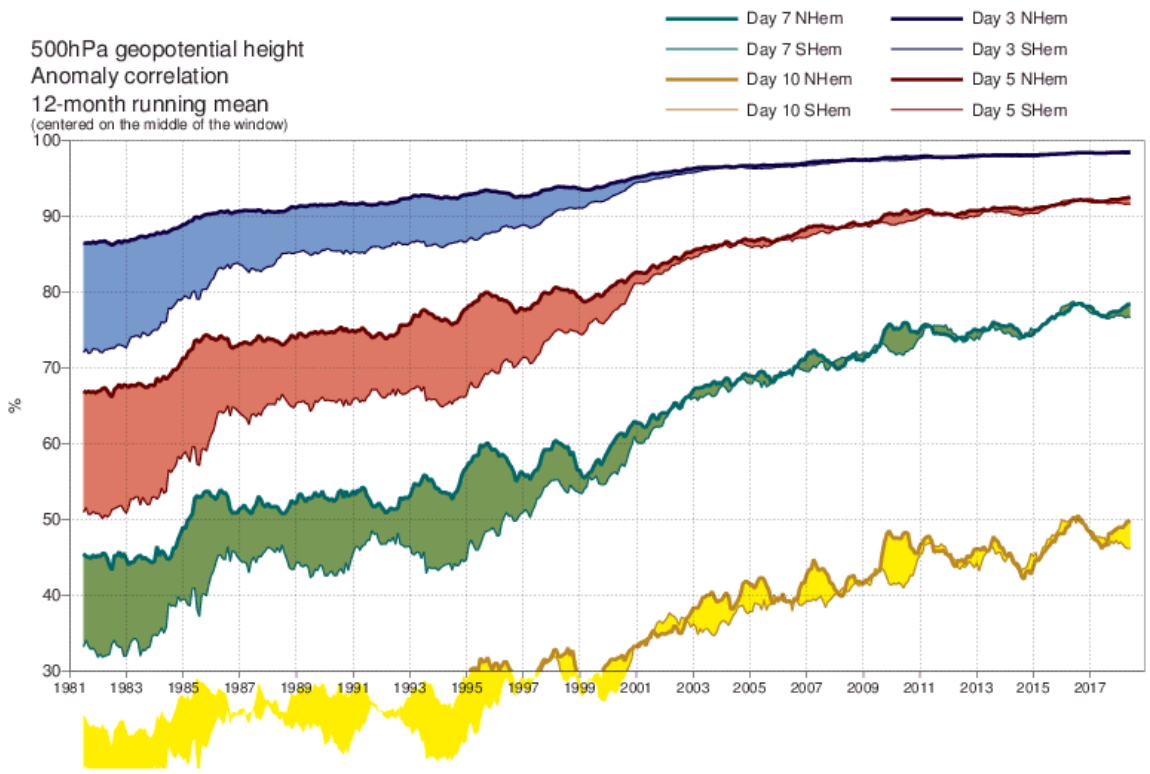

Figure 1.1: Anomaly correlation of ECMWF 500 hPa height forecasts. Figure from .

Fig. 1.1. One great achievement in this century has been the convergence of forecast performance in the southern hemisphere to being nearly identical to the northern hemisphere. In the last ten years, day-5 forecasts have risen above 90% ACC, day-7 forecasts are nearing 80%, and even day-10 forecasts are exhibiting potential as they near 50% ACC (Fig. 1.1). This achievement is due in large part to advancing the use of satellite data with 4DVAR (Bauer et al. 2015).

Although medium-range forecast skill of Numerical Weather Prediction (NWP) has increased substantially over the last three decades (e.g., Thorpe 2004; Shapiro et al. 2010), individual forecasts can still experience large error. Dropouts, or busts, are particularly evident as outliers falling well below the long-term mean performance of model forecasts. Often these situations are noticed by the public as large and perceptible differences from anticipated temperatures or precipitation. Of even greater importance are occasions when these busts result in a failed forecast of a high impact weather event, such as a winter storm or heavy rainfall.

While NWP has experienced improved overall forecast statistics, for example increasing global annually-averaged 500 hPa height ACC, bust events remain. These incidents of low skill are represented by the tail in the skewed Poisson distribution of forecast performances. In the medium-range forecast period, bust events are typically focused in subcontinental domains as NWP error grows and clusters on synoptic scales (Boer 1994; Tribbia and Baumhefner 2004; Ngan and Eperon 2012). Figure 1.2 depicts ACC scores over Europe during a bust event that was the subject of the case study in Rodwell et al. (2012). Six-day forecasts from the leading model centers during this 30-day period performed with an ACC averaging around 80%. However there is an abrupt drop in performance between 8 April and 11 April. All models approach or fall below 0% ACC, which corresponds to a greater than 90^o phase error.

Individual forecast failures often gain attention and become topics of case studies (e.g., Rodwell et al. 2012, Grazzini and Isaksen 2002), however, it is difficult to gain insight

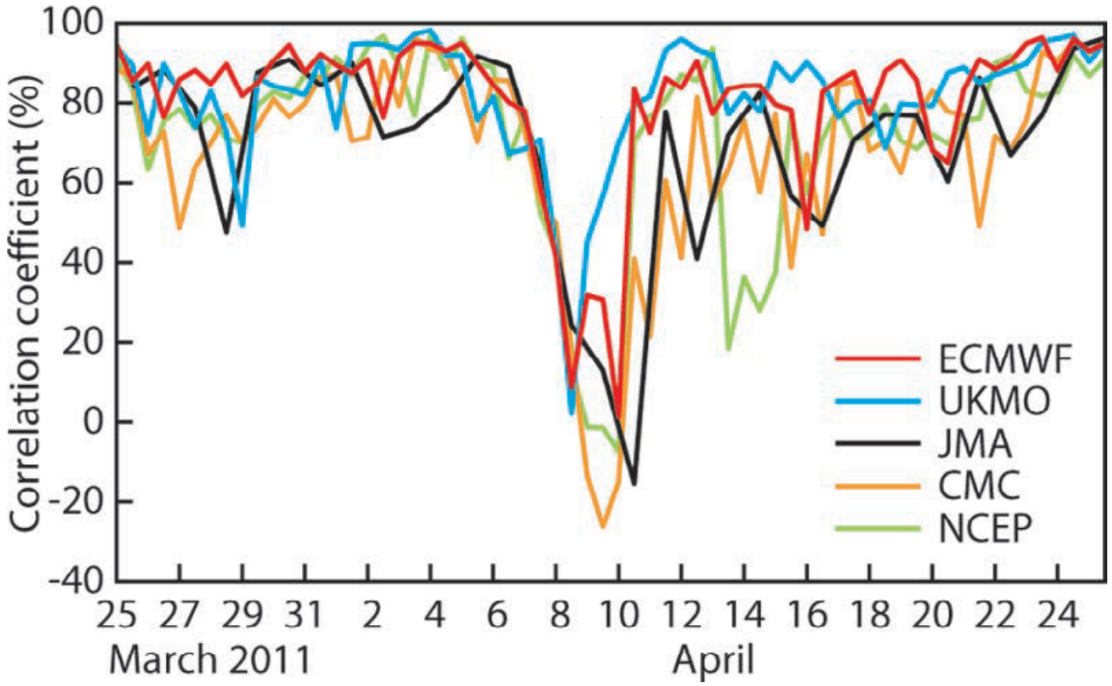

Figure 1.2: Anomaly correlation coefficient for day-6 forecasts of 500 hPa heights over Europe from leading forecast model centers. Dates correspond to the time of model initialization. Figure from Rodwell et al. (2013).

into the weaknesses of a modeling system through a few cases. There has been a recent effort to systematically study bust cases, with a focus on sub-continental domains (e.g. Rodwell et al. 2013, hereafter Rodwell). Rodwell evaluated hundreds of cases in ERA-Interim re-forecasts and proposed that an upstream convective environment over the central U.S. was one mechanism responsible for 6-day busts over Europe. Short-term mesoscale errors originate from difficulties in handling convection in the model and these errors can subsequently grow upscale and be communicated downstream.

Rodwell focused on the effect of potential vorticity modification by errors in convective heating, and Gray et al. (2014) and Clarke et al. (2019a) elaborated on this effect of errors in mesoscale convective systems (MCSs) affecting the structure and propagation of Rossby waves downstream. Stensrud and Anderson (2001) demonstrated an example of upscale influence of convection in which persistent MCS activity in the mid-latitudes can force a Rossby wave response that influences the planetary pattern remote from the source. It follows then that errors associated with the original mesoscale features have the capacity to be communicated remotely through the Rossby wave response (Lillo and Parsons (2017), Parsons et al. (2019a)) resulting in poor predictive skill. Clarke et al. (2019a) further specified the relative importance of the upper-level perturbations associated with MCSs; greater influence on synoptic scales results from perturbations near the tropopause rather than perturbations at any other level. As demonstrated by Lillo and Parsons, errors introduced by the mesoscale divergent wind at jet level impinge on the potential vorticity field and result in a wave response that amplifies downstream. A review discussion of Rossby wave activity and the relationship to predictability is provided at the end of this chapter.

Many of the studies referenced above focus on continental convection. Lillo and Parsons (2017) discuss another phenomenon on the same spatial scale as MCSs with even deeper heating profiles and longer duration: the tropical cyclone (TC). Unlike MCSs, the influential radius of TCs is typically well equatorward of the mid-latitude westerlies. However occasionally TCs recurve poleward, usually in the western part of ocean basins, and

interact with the westerly jet stream. As the TC encounters increasing vertical wind shear, it undergoes substantial structural changes and assumes extratropical characteristics (Harr and Elsberry 2000; Jones et al. 2003). The immense diabatic heating and canopy of upper level divergent wind impinging on the mid-level westerlies presents forecasting challenges in both the short term and with the downstream wave response at longer lead times (Riemer et al. 2008; Riemer and Jones 2010; Archambault et al. 2013b, 2015). Lillo and Parsons (2017) shows a peak in the frequency of day-6 bust cases over Europe during the core of the Atlantic hurricane season, and a greater occurrence of recurving Atlantic TC tracks preceding these busts. Both continental convective systems and tropical cyclones are examples of mesoscale features that impact synoptic flow and predictability.

1.4 Scales of Atmospheric Motion

A theme of this study is the propensity for interaction across different scales of the atmosphere. It has been shown that the atmosphere is not a uniform spectrum of processes on all wavelengths, but rather has preferred scales (Vinnichenko 1970; Fiedler and Panofsky 1970). Specifically, spectral peaks in kinetic energy are observed on the synoptic scale and microscale, with a distinct gap where mesoscale phenomena are observed. Synoptic and microscale motions are driven by distinct types of instabilities. In between, mesoscale systems act as a channel for kinetic energy derived from these instabilities to interact.

Fluid flows with fully developed turbulence that is homogeneous and isotropic have the specific characteristic of a power-law curve in the horizontal kinetic energy spectrum (Kolmogorov 1941; Obukhov 1949). The atmosphere does not exhibit fully developed homogeneous and isotropic turbulence. However, specific features as well as domains large enough in space and long enough in time can satisfy this condition.

The first complete investigation of the atmospheric kinetic energy spectrum covering the entire range of mesoscale and synoptic scale motions was presented in Nastrom and

Gage (1983), Nastrom et al. (1984), and Nastrom and Gage (1985), based on wind measurements taken by aircraft during the Global Atmospheric Sampling Program (GASP). These data are shown plotted in the kinetic energy spectrum in Fig. 1.3, with the horizontal scale on the x-axis (wavelength on the top axis, wavenumber on the bottom axis), and the kinetic energy on the y-axis. The solid line is a functional fit by Lindborg (1999) to aircraft observations during Measurement of Ozone and Water Vapor by Airbus In-Service Aircraft (MOZAIC); in impressive agreement with the GASP data. This plot reveals two distinct regimes of power-law behavior (appearing linear in log-log space), along with the overall characteristic of the downward energy cascade toward smaller scales. The two regimes in Fig. 1.3 are a $k^{-5/3}$ fit for flow wavelengths of 300 km and smaller (meso-β and meso-γ scales), and a k^{-3} fit for flow wavelengths of around 1000 km and larger (synoptic to planetary scales).

The significance of the power-law slope in the atmospheric kinetic energy spectrum is that this same behavior is characteristic of self-similar systems (Pope and Pope 2000). This quality is observed, for example, in cumulus fields. In fully-formed isotropic turbulent flow with a static kinetic energy spectrum, self-similarity is exhibited across the inertial range, which spans the scales between where energy is injected and where energy is dissipated. Within the inertial range, energy is conserved and propagated across scales by non-linear interactions between eddies. On the peripheries of the inertial range, energy is injected at the largest scales by differential meridional heating, cascades toward smaller scales, and dissipates through eddy-breakup and viscosity (Richardson 1922). While energy injection occurs at the largest scales through baroclinic instability and is cascaded directly (Tung and Orlando 2003; Tulloch and Smith 2006), it can also be injected on small scales (e.g. through the release of convective instability, and the outflow from resulting thunderstorms) and cascaded inversely (Gage 1979; Lilly and Petersen 1983).

Synoptic-scale and larger flows are quasi-two-dimensional which is consistent with the assumption of hydrostatic balance valid for horizontal length scales that are much larger

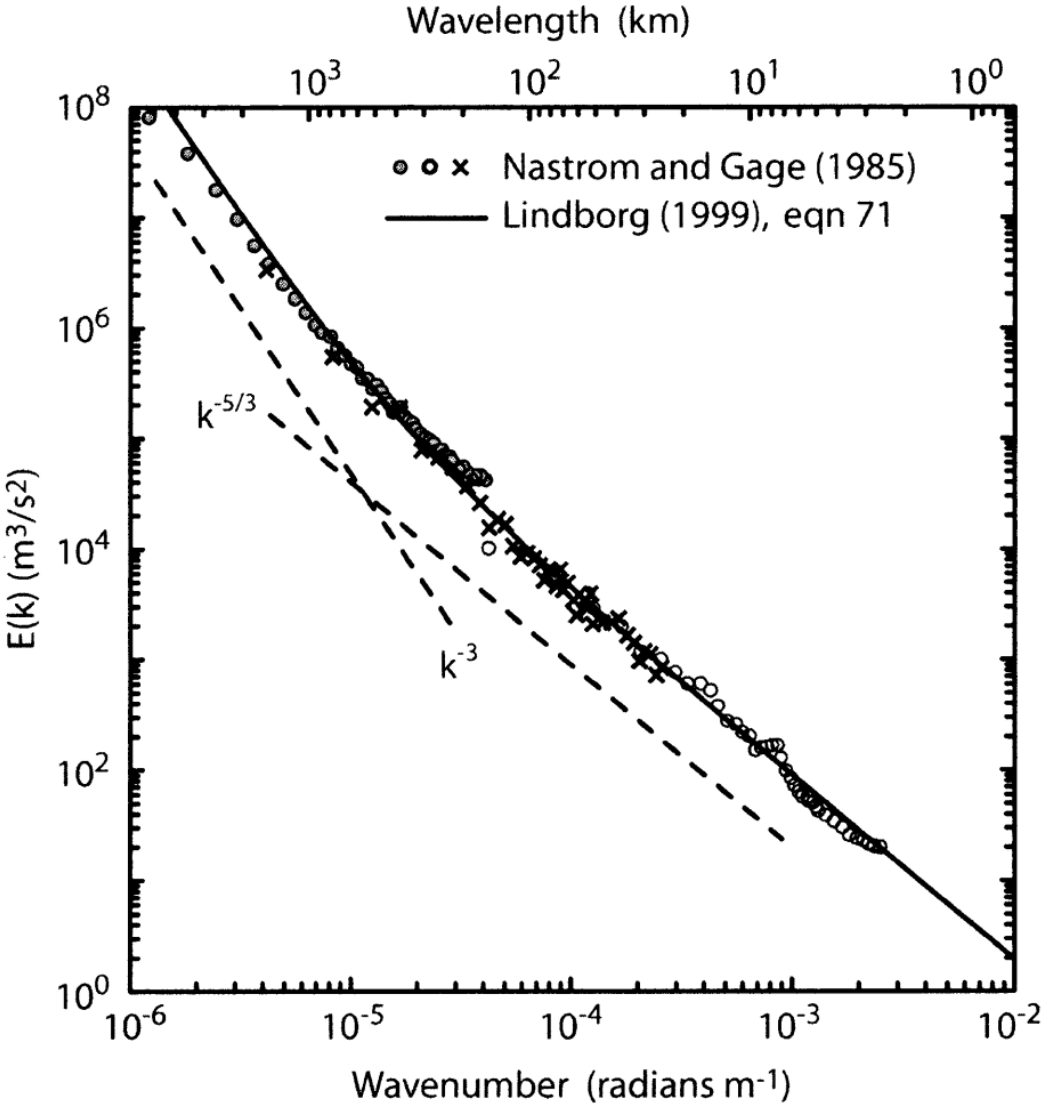

Figure 1.3: The horizontal kinetic energy spectrum from Nastrom and Gage (1985) derived from GASP (scatter points), and the functional fit by Lindborg (1999) derived from MOZAIC (solid line). Reference slopes for $k^{-5/3}$ and k^{-3} given by dashed lines. Figure from Skamarock (2004).

than the vertical length scale. As such, flow is approximately horizontal and non-divergent and conserves enstrophy (the square of vorticity) in addition to energy. The kinetic energy spectrum for these scales has been found to follow a k^{-3} slope (Nastrom and Gage 1985), which has been supported using barotropic two-dimensional (Kraichnan 1967) and quasi-geostrophic (Charney 1971) frameworks. This particular slope and energy cascade is a resulting characteristic of horizontal waves and vortices originating at the largest scales and breaking down into smaller vortices (Boer and Shepherd 1983).

The $k^{-5/3}$ spectral slope is predicted by three-dimensional turbulence theory which applies to cloud-scale. The mesoscale range is more complicated and involves both rotational and divergent components of the flow from eddies and inertia-gravity waves (IGWs) interacting non-linearly (Gkioulekas 2006). The divergent and rotational components of the flow share similar magnitudes in the meso-β and meso-γ scales, and both with spectral slopes near $k^{-5/3}$. However at larger scales, it is the rotational component that features the turn to a k^{-3} spectral slope while the divergent component remains near $k^{-5/3}$ (e.g. Judt 2018). For this reason, especially near the intersection of the two inertial subranges, it is of interest to employ a Helmholtz decomposition to extract the irrotational and nondivergent components of the flow. This decomposition is pertinent in the next section, which discusses the assessment of error growth in NWP and limits of predictability as evaluated in kinetic energy spectra.

The observed kinetic energy spectrum is shaped by mechanisms for scale-interaction in atmospheric flows. These same mechanisms thus also dictate how errors evolve in numerical simulations of the atmosphere. For this reason, one particular point of interest is the "kink" that demarcates the transition between the $k^{-5/3}$ and the k^{-3} regimes of the kinetic energy spectrum (Fig. 1.3).

$$T_d = (t_2 - t_1)\left[\frac{ln(2)}{ln\left(\frac{E(t_2)}{E(t_1)}\right)}\right] \tag{1.1}$$

The doubling time for error decreases by decreasing scale of the flow. Error at the lowest resolvable scale in a model will grow exponentially the fastest. The result is that increasing model resolution does not linearly increase the limits of predictability. This invites two considerations. The first is the source of the initial error. The second is the shape of the background kinetic energy spectrum and dominant scale interactions that dictate how error evolves. The implication of the intrinsic predictability limit is that regardless of improvements to NWP and increases in resolution, error will always develop at the smallest scales and grow upscale eventually contaminating the entire forecast and rendering zero useful skill beyond a certain lead-time.

While atmospheric flows are inherently chaotic and error saturates quickly at small scales and grows upward, this does not eliminate the potential for longer predictability at those small scales. Both constant and periodic forcing, such as that from terrain or diurnal and annual cycles in solar radiation, should add predictive skill particularly on synoptic and planetary scales. Reliable forcing mechanisms such as these allow for the possibility of skillful seasonal and climate forecasts. In addition, this error reduction can cascade downscale, extending predictability limits with mesoscale features. Synoptic forcing features that have mesoscale structure, such as fronts, also add predictability at smaller scales. This downscale cascade of predictability is what allows convection-resolving models (CRM) such as the High Resolution Rapid Refresh (HRRR) to have skill for several hours of lead time (Anthes 1986).

For a given forecast bust event, this invites the question to what degree was there a failure of the NWP system, and to what degree did the flow evolution have an inherently low predictability. Finally, what aspects of the flow evolution contributed to reduced intrinsic predictability. These are the questions that motivate this work, and will be addressed in Chapter 2.

1.5 Rossby Waves

Limits in the predictability of atmospheric flow emerge from errors that saturate quickly at small scales of motion and subsequently grow at successively larger scales. Convection is the primary mechanism responsible for the initial growth of forecast error (Zhang et al. 2003, 2002, 2003, 2007a; Selz and Craig 2015; Sun and Zhang 2016; Judt 2018; Parsons et al. 2019b). It is from this stage that, as shown in Fig. 1.4 from Bierdel (2017) and demonstrated in Lillo and Parsons (2017), errors grow through the mesoscale with a divergent flow component expanding spatially. The divergent flow impinges on the synoptic background flow and leads to a displacement in the jet stream, developing rotational errors and a wave response within the jet.

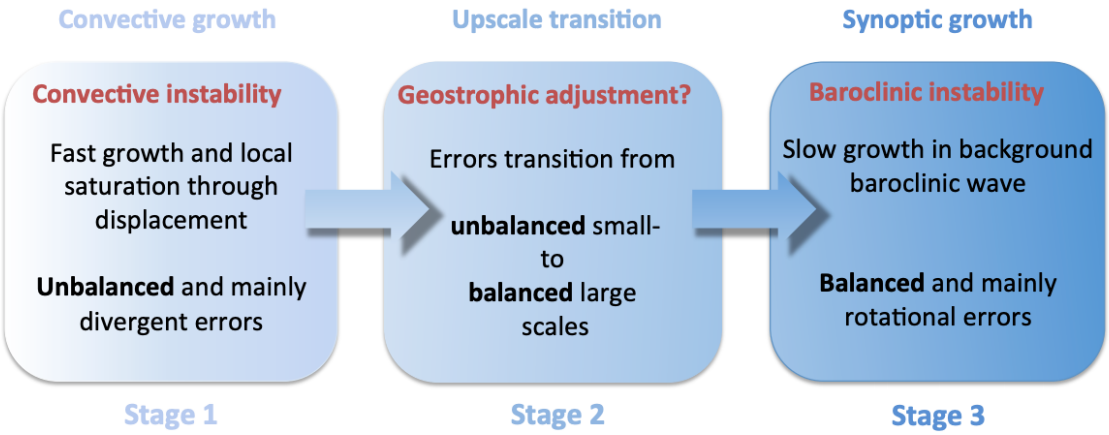

Figure 1.4: Schematic from Figure 1.8 of Bierdel (2017) showing the three-stage conceptual error growth model described by Zhang et al. (2007b).

The existence of this response, known as a Rossby wave (Rossby 1939; Haurwitz 1940), is a result of a perturbation on a background gradient of potential vorticity (PV, Hoskins et al. 1985). While the source perturbation has the capacity to produce wave responses in a wide spectrum of wavenumbers, it is the background state that dictates which wavenumbers are evanescent and which are favored to progress. Analogous to geometric optics, the background basic state flow pattern can be considered as a refractive medium in which

Rossby wave activity of varying wavenumbers propagates and can be projected through ray tracing (Hoskins and Karoly 1981; Hoskins and Ambrizzi 1993). The refractive index in this framework is a function of the PV gradient in the background flow, which in practical use is defined by some low-pass filter in space and/or time.

Hoskins and Ambrizzi (1993) demonstrates the great circle path of ray traces for long-wave (low wavenumber) Rossby activity curving into high latitudes, while ray traces for shortwave (high wavenumber) Rossby activity are confined to lower latitudes where the gradient of planetary vorticity is largest. Jet streams also introduce local maxima in PV gradient, which have the ability to trap and channel Rossby wave activity downstream, especially in the mid-latitudes. These ribbons of enhanced PV gradient are referred to as Rossby waveguides, also defined in the ray framework by a local maximum in the refractive index. The shortwave Rossby waves ducted in the waveguide often travel within an amplitude envelope called a Rossby wave packet (RWP). RWPs travel eastward at a velocity (known as the group velocity, $\vec{C}_g$) faster than the phase velocity of the individual waves, resulting in successive amplification of downstream troughs and ridges, known as downstream development. The existence of a waveguide allows for vorticity perturbations of sufficient scale to trigger RWPs (Schwierz et al. 2004). Wirth et al. (2018) provides a comprehensive review of RWPs and waveguides, including works on their relationship to extreme weather events and predictability.

Grazzini and Vitart (2015) found that long-tracking RWPs, such as those originating over the Pacific, yield higher medium-range predictability over Europe compared to short-tracking RWPs coming from the United States or western Atlantic. One caveat that Grazzini and Vitart acknowledge, and elaborated on by Lillo and Parsons (2017), is that RWPs can act to amplify and propagate error in the waveguide. Thus while potentially increasing intrinsic predictability, long-tracking RWPs do not always guarantee an improvement in verification scores. Errors associated with an initial vorticity perturbation follow the downstream development associated with the group velocity of the RWP and would have

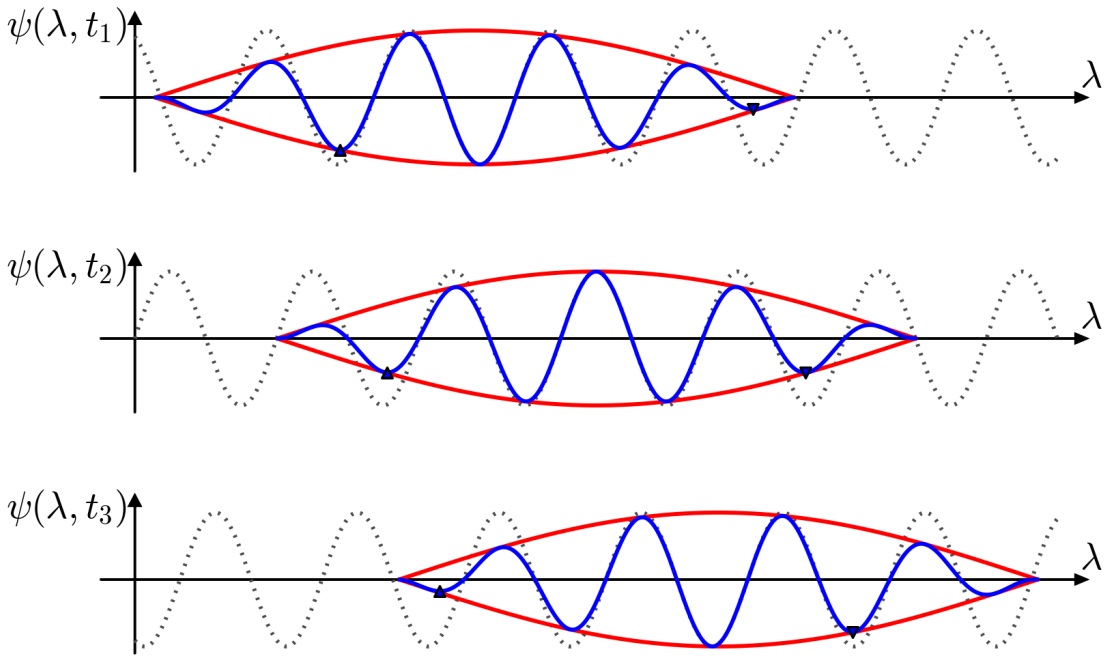

Figure 1.5: Schematic of a zonally-oriented Rossby Wave Packet (RWP) at 3 successive times, represented by streamfunction along a line of constant latitude. The dashed line is the carrier wave, the red lines depict the amplitude envelope, and the blue line is the resulting streamfunction. Upward-pointed triangles note the base of a de-amplifying trough in the exit of the RWP, and downward-pointed triangles note the base of an amplifying trough in the entrance of the RWP.

significant ramifications downstream in the waveguide. RWPs have also been shown to be precursors to high-impact weather events (HIEs, e.g. Shapiro and Thorpe 2004; Chang 2005; Wirth and Eichhorn 2014). Therefore, we can connect incipient errors associated with a perturbation provoking a response within a waveguide to reduced predictability downstream, as well as increased uncertainty surrounding HIE potential.

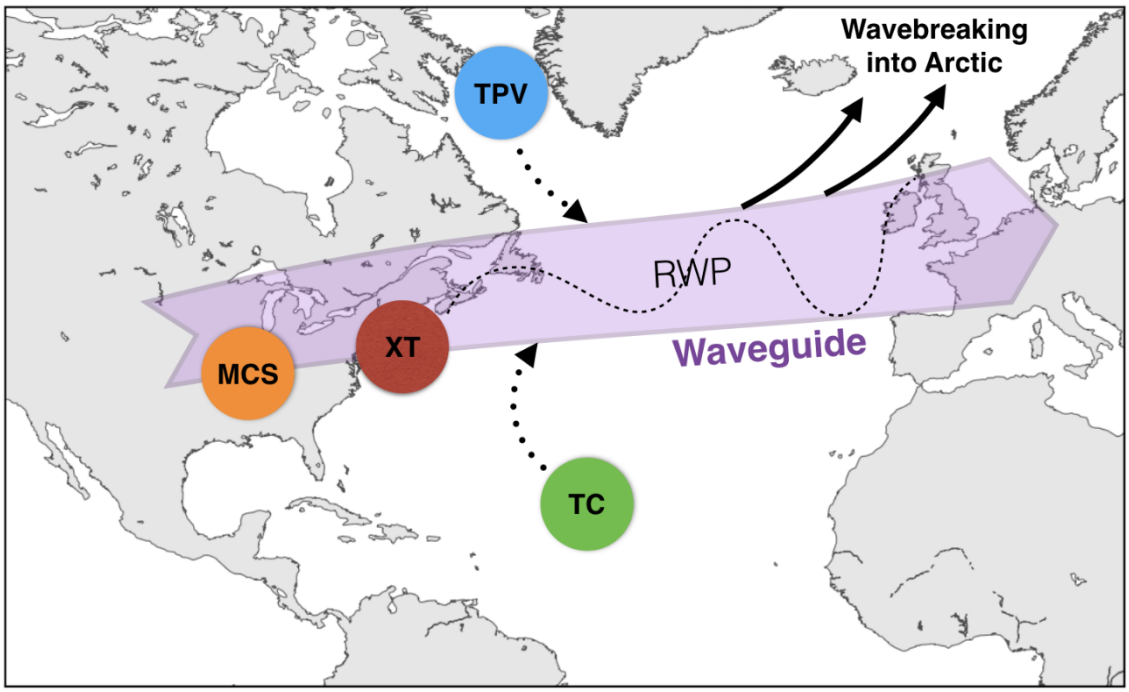

Figure 1.6: Schematic of the Atlantic waveguide, and types of triggers for downstream Rossby wave activity. MCS: Mesoscale Convective System, XT: Extratropical Cyclone, TC: Tropical Cyclone, TPV: Tropopause Polar Vortex.

There has been recent effort to objectively identify and track RWPs. The three-dimensional wave activity flux formulation by Takaya and Nakamura (2001a) for migratory waves is an expansion of Plumb (1985) for stationary waves. These formulations provide insight into the geometry of the waves, their evolution, and relationship with the larger scale.

Positively tilted troughs feature equatorward wave activity flux and poleward westerly momentum flux. Thorncroft et al. (1993) classified these systems as “Life Cycle” number 1 or LC1 behavior. Their geometry is also consistent with anticyclonic wavebreaking,

typically occurring on the equatorward or anticyclonic shear side of the mid-latitude jet. The LC1 evolution often leads to thinning troughs and PV streamers, as cyclonic vorticity is concentrated and stretched along a deformation axis between anticyclones. Along the axis of dilatation, cyclonic vorticity becomes primarily manifested through shear. However, a highly concentrated area of curvature vorticity exists at the tail of the trough, which can occasionally lead to cut-offs from the mean flow (Fig. 1.7), and surface cyclogenesis where there is downstream vorticity advection. Additionally, LC1 behavior is associated with propagation of Rossby wave activity into the tropics, particularly the eastern Pacific (Kiladis and Feldstein 1994), and has large-scale relationships with the strength of the Hadley circulation and ENSO (Caballero 2007; Caballero and Anderson 2009).

Negatively tilted, cyclonically breaking, "Life Cycle" number 2 or LC2 troughs exhibit poleward wave activity flux and equatorward momentum flux. The counterpart ridges to LC1 and LC2 behaviors are classified as P2 and P1, respectively, by Gabriel and Peters (2008). The LC2 and P1 cyclonic wave behavior can be especially important for the pattern at polar latitudes. These synoptic-scale features can lead to sub-seasonal and seasonal oscillations in the annular mode (Rivière and Orlanski 2007; Franzke et al. 2011; Kunz et al. 2009). Cyclonic wavebreaking features poleward wave activity flux, which acts to reverse the PV gradient between the arctic and mid-latitudes.

In addition to interests within sub-continental domains, interaction between meridionally and vertically propagating Rossby wave activity (often associated with wave breaking) and the base state environment can modify the planetary-scale flow pattern (Holton 1976; Andrews and McIntyre 1976) and have lasting impacts on the low-frequency modes of the atmosphere (e.g. Archambault and Harr 2013; Bosart et al. 2017). It follows that errors carried within a RWP and associated breaking waves can have the same magnitude of impact on the low-frequency modes. This invites an important consideration that given the occurrence of a medium-range forecast bust, uncertainty dramatically increases in the long-range forecast of the planetary-scale pattern.

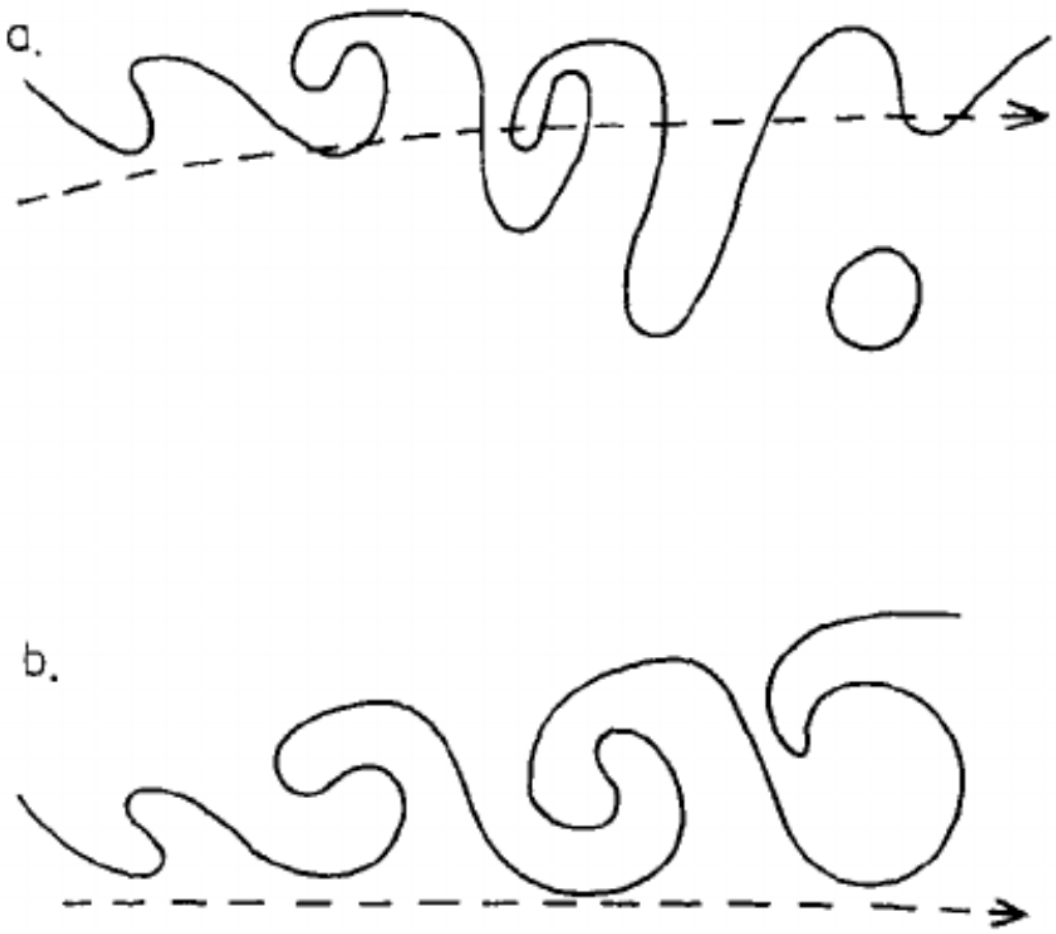

Figure 1.7: Figure 12 from Thorncroft et al. (1993): ”Schematic of a PV-theta contour in an Atlantic storm track sharing its main characteristics with (a) an LC1-type life cycle and (b) an LC2-type life cycle. The dashed line marks the approximate position of the mean jet at each stage.”

1.6 Summary and Outline

The implications of forecast busts on predictability of high impact events, as well as the impacts extending beyond the mid-latitudes and on subseasonal prediction, motivate this study of the life cycle of error in NWP. The purpose of this dissertation is to investigate all stages of error, from origin to growth to propagation, associated with medium-range forecast busts, and the implications in pattern evolution and predictability thereafter.

This dissertation is organized as follows. Diagnostics for error in NWP are developed in chapter 2. Using these metrics, we discuss the origins of error especially tied to mesoscale features, as well as the response to this error through considerations of upscale growth and geostrophic adjustment. Finally propagation and amplification of error as organized on synoptic scales will be investigated within the framework of Rossby waves. This chapter concludes with an application of the aforementioned error metrics to distinguish between busts and non-busts or good forecasts. Chapter 3 will discuss the results of a sensitivity study with one case run using the Model for Prediction Across Scales (MPAS; Skamarock et al. 2012). Chapter 4 applies MPAS to study the predictability and sensitivity of an extreme cold air outbreak to a sub-synoptic scale feature. Chapter 5 discusses the combined effects of an historic ENSO event and rare RWP activity in producing an extreme trough and cold air outbreak over Mexico. These chapters apply concepts and tools for analyzing predictability and Rossby wave activity in cases of extreme events and forecast busts. The final chapter summarizes the dissertation and continues the discussion on the effect of error growth into planetary and subseasonal to seasonal scales.

Chapter 2

Analyzing Error in Numerical Weather Prediction

In the quest to better understand predictability and restrictions thereof, the primary focus of past studies has typically been on the origin of error in the beginning of the forecast. Lorenz (1969) showed, using a spectral turbulence model, that limits to predictability can result from features below the scale of observation as errors saturate at small scales and grow upscale. However as discussed by Rotunno and Snyder (2008) and Durran and Gingrich (2014), it is the slope of the background kinetic energy spectrum that dictates error growth, and not the scale of the initial error. Thus, it is important to consider at all times during the forecast that error at large scales grows rapidly downscale. As an example, consider a slight phase shift in the position of a synoptic-scale trough, and the immediate impact it would have on the existence and position of convection. Regardless of the scale of the initial error, the same action of upscale growth from the minimum resolvable scale occurs, saturating through the microscales and mesoscales.

In this chapter, we discuss the techniques used in our subsequent investigation of the predictability of two extreme events and our study of the forecast busts and the impact of diabatic processes. We also quantify error origins in NWP, and distinguish those errors that are prone to upscale growth. We show that the forecast bifurcation from truth is less important at the origin of the error, but rather it is the error growth within the downstream waveguide that is consequential to a bust event. It is the sensitivity of the downstream environment to the introduction of error that is paramount in the development of a large-scale busted forecast.

2.1 Potential Vorticity Diagnostics

The focus of this study is on situational limits to regional to global predictability, both intrinsic and practical, in the medium-range (day-5 to day-10). Upscale error growth begins to saturate by day-3 in the forecast, after which time up-magnitude error growth takes over (Judt 2018). Our interest in the study of error origins is on the scales leading to up-magnitude growth, with synoptic scale responses. This process includes phenomena appearing on the mesoscales, and growing to baroclinic scales.

We approach the investigation of error origins and initial growth from the perspective of PV tendency, consistent with past studies (e.g. Davies and Didone 2013; Baumgart et al. 2018). There are a number of PV definitions, but the Ertel PV (EPV, Π) and potential temperature (theta, θ) framework is exceptionally useful due to clear conservation properties without assumptions. EPV is defined as:

$$\Pi = \frac{\vec{\omega}_a}{\rho} \cdot \nabla\theta \tag{2.1}$$

where ω_a is the three-dimensional absolute vorticity vector combining relative vorticity and planetary vorticity, ρ is density, and θ is potential temperature. The units of EPV are Potential Vorticity Units (PVU) defined as $1\ PVU = 1 \times 10^{-6}\ K\ kg^{-1}\ s^{-1}\ m^2$. The dynamic tropopause outside of the tropical latitudes is designated by a surface of constant PV that is generally chosen to be 2 PVU. This convention is followed hereafter.

As shown in Pedlosky (1998), the time tendency of EPV following the motion of a fluid can be derived as:

$$\frac{D\Pi}{Dt} = \frac{\vec{\omega}_a}{\rho} \cdot \nabla\frac{D\theta}{Dt} + \frac{\nabla\theta}{\rho} \cdot \left(\nabla \times \frac{\vec{F}}{\rho}\right) \tag{2.2}$$

where $\vec{F}$ is the frictional force vector. Equation 2.2 shows that the only ways to change EPV along the path of a fluid, such that it is no longer a conserved quantity, is through differential diabatic heating ($\nabla\frac{D\theta}{Dt}$) that changes the potential temperature gradient, and through the curl of the frictional force ($\nabla \times \vec{F}$) countering relative vorticity.

Cavallo and Hakim (2009, 2010a) demonstrate the effects of friction are small near the tropopause and can be neglected. In addition, since the gradient of potential temperature is two to three orders of magnitude larger in the vertical than in the horizontal, Eq. 2.2 simplifies to

$$\frac{D\Pi}{Dt} = \frac{\eta}{\rho}\frac{\partial}{\partial z}\dot{\theta} \tag{2.3}$$

where η is the vertical component of absolute vorticity, and the notation $\dot{\theta}$ refers to the material derivative of potential temperature or the diabatic heating rate. In applying this assumption note that the largest errors in the PV field often occur near the level of the tropopause in the vicinity of sharp PV gradients, resulting from differences in the location of the tropopause (Dirren et al. 2003; Gray et al. 2014; Giannakaki and Martius 2016; Baumgart et al. 2018). This quantity can be partitioned into different physical sources of diabatic change, which is discussed further and applied in Chapter 4.

Errors defined by deviations in the forecast PV from analysis (truth) grow through advection by the error wind and non-conservative PV tendency due to diabatic heating (Davies and Didone 2013). Given no antecedent PV error, the error wind must be irrotational. Therefore, PV error must originate from diabatic heating and advection of PV (forecast PV is same as truth PV with zero error) by the error wind.

Following the derivation from Davies and Didone (2013), the lagrangian change of PV error following the true flow can be written as

$$\begin{aligned}\frac{\partial PV_e}{\partial t} + \vec{U}_t \cdot \nabla PV_e = &-\vec{U}_e \cdot \nabla PV_t - \vec{U}_e \cdot \nabla PV_e \\ &+ PV_t\Big(\frac{\partial Q_e}{\partial \theta}\Big) + PV_e\Big(\frac{\partial Q_t}{\partial \theta}\Big) + PV_e\Big(\frac{\partial Q_e}{\partial \theta}\Big) \\ &- Q_t\Big(\frac{\partial PV_e}{\partial \theta}\Big) - Q_e\Big(\frac{\partial PV_t}{\partial \theta}\Big) - Q_e\Big(\frac{\partial PV_e}{\partial \theta}\Big)\end{aligned} \tag{2.4}$$

where the subscript t indicates truth field variables, and the subscript e indicates error field variables.

The resulting equation has nine terms on the right side that Davies and Didone group in various ways and describe their physical meaning. Ultimately this equation is limited by following a specific flow and the nonlinear terms that result. We can similarly write the time change of PV error following the forecast flow by simply substituting for the forecast variables instead of truth variables. Notice several similarities, except for sign changes in the nonlinear terms.

$$\begin{aligned}\frac{\partial PV_e}{\partial t} + \vec{U}_f \cdot \nabla PV_e = &-\vec{U}_e \cdot \nabla PV_f + \vec{U}_e \cdot \nabla PV_e \\ &+ PV_f\Big(\frac{\partial Q_e}{\partial \theta}\Big) + PV_e\Big(\frac{\partial Q_f}{\partial \theta}\Big) - PV_e\Big(\frac{\partial Q_e}{\partial \theta}\Big) \\ &- Q_f\Big(\frac{\partial PV_e}{\partial \theta}\Big) - Q_e\Big(\frac{\partial PV_f}{\partial \theta}\Big) + Q_e\Big(\frac{\partial PV_e}{\partial \theta}\Big)\end{aligned} \tag{2.5}$$

We can remove the nonlinear error terms by adding these two different error tendency equations, and form an equation that is not dependent on the chosen flow to follow. Presented below is our original equation that is the PV error tendency following the average flow of the forecast and the truth.

$$\begin{aligned}\frac{\partial PV_e}{\partial t} + \vec{U} \cdot \nabla PV_e = &-\vec{U}_e \cdot \nabla PV \\ &+ PV\Big(\frac{\partial Q_e}{\partial \theta}\Big) + PV_e\Big(\frac{\partial Q}{\partial \theta}\Big) \\ &- Q\Big(\frac{\partial PV_e}{\partial \theta}\Big) - Q_e\Big(\frac{\partial PV}{\partial \theta}\Big)\end{aligned} \tag{2.6}$$

where $\vec{U}$, PV, and Q refer to the averaged forecast and truth variables. The nonlinear terms are removed, and we begin to see more mathematical and physical elegance in the equation.

We can now arrange equation (2.6) to resemble the linearized PV equation derived below,

$$\frac{\partial PV}{\partial t} + u\frac{\partial PV}{\partial x} + v\frac{\partial PV}{\partial y} = s \tag{2.7}$$

$$\frac{\partial PV'}{\partial t} + \vec{\overline{U}} \cdot \nabla_H PV' + \vec{U}' \cdot \nabla_H \overline{PV} = s' \tag{2.8}$$

where variables with bars indicate the slowly-evolving large scale state, and variables with primes indicate the perturbations on top of that slowly evolving state. ∇_H is the gradient operator in the horizontal. The total source term, s, contains all influences on PV tendency outside of horizontal advection and is generally a summation of the diabatic terms. Following the linearization of Equation 2.7 to get Equation 2.8, nonlinear combinations of variables have been removed from the left side of the equation, and can be contained within s'.

Unlike the linearizing of the PV equation which in practice requires a method of obtaining the base state that can often be subjectively defined, the above PV error tendency equation (Eq. 2.6), which already fits the same mold as Equation 2.8, does not require partitioning of the flow into base state and perturbations. The error variables in Equation 2.6 represent the perturbations, and the base state is given by the average of the forecast and the truth. A source term can be formed by the four diabatic terms on the right side of Equation 2.6.

On meso to synoptic scales, diabatic heating is most prominent in the middle troposphere where PV and PV gradients are small, and heating is small near the tropopause where PV gradients are large (e.g. Ling and Zhang 2013). The nonconservative diabatic terms are thus generally small compared to the advection term, and have little impact at the tropopause. In contrast, the advection term will be large at the tropopause where horizontal PV gradients are largest. This does not negate the importance of correctly representing the magnitude and profile of diabatic heating in NWP, as it is the kinematic response intimately connected to vertical gradients in heating that drive the non-negligible terms in Equation 2.12 (Mapes and Houze Jr 1995; Ling and Zhang 2013). At the start of the forecast, the challenge is for data assimilation to correctly initialize these vertical heating profiles.

Assuming minimal direct contribution from diabatic heat to error growth, we consider an adiabatic barotropic atmosphere for approximate antecedent conditions to synoptic-scale error growth on the tropopause. This approximation allows us to analyze errors on

the tropopause from a purely kinematic perspective. Using Helmholtz decomposition, we can partition the error wind into irrotational (χ) and solenoidal (ψ) components, such that $\vec{U_e} = \vec{U_{e\chi}} + \vec{U_{e\psi}}$. With no initial PV error, the solenoidal component of the error wind is negligible. The primary contributor to initial PV error growth is advection of PV by the irrotational error wind. Divergence at the tropopause is often tied to deep convection and the associated latent heat release in the middle troposphere (Riemer and Jones 2010; Teubler and Riemer 2016), and therefore error growth can be indirectly connected to diabatic heating. However, the greatest direct contribution to large scale PV tendency and error growth comes not from the in situ diabatic heating, but rather PV advection by the irrotational component of the error wind.

$$\frac{\partial PV_e}{\partial t} + \vec{U_\chi} \cdot \nabla PV_e + \vec{U_\psi} \cdot \nabla PV_e = -\vec{U_{e\chi}} \cdot \nabla PV - \vec{U_{e\psi}} \cdot \nabla PV \tag{2.9}$$

Rearranging to isolate the advection by irrotational wind terms on the right, we can mimic the Rossby Wave Source (RWS) term derived from the barotropic vorticity equation in Sardeshmukh and Hoskins (1988): RWS = $-\nabla \cdot (\vec{v_\chi}\zeta)$, which for barotropic flow is equivalent to RWS = $-\vec{v_\chi} \cdot \nabla PV$. This RWS term is physically the advection of barotropic potential vorticity by the irrotational wind. We can also adapt his linearization as RWS = $-\vec{v_\chi'} \cdot \nabla PV - \vec{v}_\chi \cdot \nabla PV'$. After rearranging, our PV error tendency equation becomes,

$$\frac{\partial PV_e}{\partial t} + \vec{U_\psi} \cdot \nabla PV_e + \vec{U_{e\psi}} \cdot \nabla PV = -\vec{U_\chi} \cdot \nabla PV_e - \vec{U_{e\chi}} \cdot \nabla PV \tag{2.10}$$

$$RWS_e = -\vec{U_\chi} \cdot \nabla PV_e - \vec{U_{e\chi}} \cdot \nabla PV \tag{2.11}$$

The two terms that comprise RWS$_e$ in Equation 2.11 are the advection of potential vorticity error by the average irrotational wind and the advection of average potential vorticity by the irrotational error wind. If we consider once again a situation in which the initial PV error is much smaller than the average PV field, then the latter term $-\vec{U_{e\chi}} \cdot \nabla PV$ becomes dominant. This term, and RWS$_e$, will be largest near strong PV gradients such as those

associated with waveguides. Returning to the full error tendency equation but keeping the assumption that the initial PV error is small, we can write

$$\frac{\partial PV_e}{\partial t} = RWS_e + PV\left(\frac{\partial Q_e}{\partial \theta}\right) - Q_e\left(\frac{\partial PV}{\partial \theta}\right) \tag{2.12}$$

For both RWS and RWS_e, it is important to recognize the relationship between the physical meaning of these terms and phenomena that might be associated with them. The most common source of both deep-layer diabatic heating and a strong irrotational wind component is convection. While convection is where errors begin (e.g. Bierdel 2017), the ability of convection, and the errors therein, to generate a large scale response is dependent on the height and strength of the associated upper level divergence. In order to activate a Rossby wave response, the irrotational wind must impinge on a potential vorticity gradient. This intersection can be displaced fairly far from the convection; specifically, as far as the Rossby radius of deformation, which determines the length scale at which geostrophic balance is restored. This metric is defined as NH/f, where N is the Brunt–Väisälä frequency, H is the scale depth of the atmosphere, and f is the coriolis parameter. In the mid-latitudes, the Rossby radius of deformation is approximately 1000 kilometers. This is also an important consideration in assessing the Rossby response due to tropical convection and the initialization points for Rossby ray tracing analysis used in Chapter 5.

Ability to generate a large scale response is facilitated through the persistence of the source (e.g. Stensrud 1996, Stensrud and Anderson 2001, Stensrud 2013). Meteorological features associated with persistent convection include long-duration or recurring MCS activity, explosive baroclinic cyclogenesis, and tropical cyclones. Recurving tropical cyclones exhibiting a large canopy of strong divergent winds aloft impinging on the mid-latitude jet, especially those undergoing extratropical transition (ET), can produce large PV perturbations in the vicinity of the jet (Jones et al. 2003). The jet and associated background PV gradient can then be very effective in producing a response downstream of the original perturbation (Archambault et al. 2013a). Explosive cyclogenesis along strong background baroclinic zones can have the same effect, with the added assistance of already

being in proximity to the mid-latitude jet. Rapidly intensifying extratropical storms are familiar to the western Pacific and western Atlantic, which are also in the entrance regions to the respective jets and waveguides (Zheng 2016).

As noted earlier, transient mesoscale convective systems (MCSs) interacting with the jet stream as a wave guide can also result in significant forecast errors (e.g., Gray et al. (2014)). Recent work, such as Parsons et al. (2019a) and Clarke et al. (2019a) elaborated on this effect of the nature of these errors. The downstream Rossby wave response found in Parsons et al. (2019a) resembled the ET interaction with the wave guide discussed earlier. Jones et al. (2003) noted that these ET errors resulted in a significant drop in medium range forecast skill over the entire Northern Hemisphere.

2.2 Kinematic Error Diagnostics

In this section, we continue with the development of kinematic error diagnostics based on the PV error tendency equations above. We have particular interest in deriving phase-independent metrics for tracking packets of error and performing composite averaging.

2.2.1 Rotational Error Metric

To track packets of error, a phase-independent error amplitude is derived from a linear combination of terms proportional to wave energy (maximized at wave nodes) and wave enstrophy (maximized at wave antinodes) in the horizontal plane. The result of this summation is identical to the addition of cosine squared and sine squared terms. Using a streamfunction calculated from the horizontal wind forecast error field, we can write:

$$E_\psi = \frac{1}{2}\Big[\Big(\frac{\partial \psi_e}{\partial x}\Big)^2 + \Big(\frac{\partial \psi_e}{\partial y}\Big)^2 - \psi_e\Big(\frac{\partial^2 \psi_e}{\partial x^2} + \frac{\partial^2 \psi_e}{\partial y^2}\Big)\Big] \tag{2.13}$$

where E is the total error amplitude, with units of m^2/s^2, and ψ_e is the error streamfunction calculated from u_e and v_e. Considering a packet of error in the form of a plane wave given by $\psi_e = \psi_{e0} sin(kx + ly + \phi)$, the error amplitude simplifies to $E = \frac{1}{2}\psi_{e0}^2(k^2 + l^2)$.

This metric is thus proportional to the amplitude of rotational errors scaled by the total wavenumber, or inversely to the wavelength.

2.2.2 Divergent Error Metric

Based on the approximations of the prognostic vorticity equation on synoptic scales, the development of synoptic scale rotational structures can be attributed to the RWS term introduced in section 2.1. As such, we recognize the importance of the irrotational wind component as a precursor to larger rotational error structures. We can write a phase-independent divergent error metric similarly to Equation 2.13, but using velocity potential calculated from the horizontal wind forecast error field.

$$E_{\chi} = \frac{1}{2}\Big[\Big(\frac{\partial \chi_e}{\partial x}\Big)^2 + \Big(\frac{\partial \chi_e}{\partial y}\Big)^2 - \chi_e\Big(\frac{\partial^2 \chi_e}{\partial x^2} + \frac{\partial^2 \chi_e}{\partial y^2}\Big)\Big] \tag{2.14}$$

Lastly we look at the Rossby Wave Source. Since RWS is a potential vorticity tendency term, we can acquire a streamfunction for the RWS by the inverse lapacian:

$$RWS_{\psi} = \nabla^{-2}\big(RWS\big) \tag{2.15}$$

We can thus write the phase-independent RWS as

$$E_{RWS} = \frac{1}{2}\Big[\Big(\frac{\partial \chi_e}{\partial x}\Big)^2 + \Big(\frac{\partial \chi_e}{\partial y}\Big)^2 - \chi_e\Big(\frac{\partial^2 \chi_e}{\partial x^2} + \frac{\partial^2 \chi_e}{\partial y^2}\Big)\Big] \tag{2.16}$$

2.2.3 Error Propagation and Amplification

Given the conclusions of Lillo and Parsons (2017), and observations from Hakim (2005) that the structure and evolution of synoptic-scale error can resemble a RWP, it is convenient to treat existent finite-scale errors as waves and wave packets. We can approach this framework by using a base state and perturbation defined from equation (2.6) to form the necessary linearized equation. Based on the derivation of a phase-independent wave-activity flux

by Takaya and Nakamura for stationary (1997) and migratory (2001c) eddies on a zonally-varying base state, an error wave-activity flux is formulated for an error streamfunction perturbation given by ψ_e,

$$\vec{W}_e = \frac{1}{2|\vec{U}|}\begin{pmatrix} U\left[\left(\frac{\partial\psi_e}{dx}\right)^2 - \psi_e\frac{\partial^2\psi_e}{\partial x^2}\right] + V\left[\frac{\partial\psi_e}{\partial x}\frac{\partial\psi_e}{\partial y} - \psi_e\frac{\partial^2\psi_e}{\partial x\partial y}\right] \\ U\left[\frac{\partial\psi_e}{\partial x}\frac{\partial\psi_e}{\partial y} - \psi_e\frac{\partial^2\psi_e}{\partial x\partial y}\right] + V\left[\left(\frac{\partial\psi_e}{dy}\right)^2 - \psi_e\frac{\partial^2\psi_e}{\partial y^2}\right] \end{pmatrix} + \vec{C_{eu}}M_e \tag{2.17}$$

$$M_e = \frac{E}{2|\vec{U} - \vec{C_{eU}}|} \tag{2.18}$$

where $\vec{U} = \frac{1}{2}(\vec{U_f} + \vec{U_t})$ is the average of the forecast wind $\vec{U_f}$ and the true wind $\vec{U_t}$, and U and V are their zonal and meridional components respectively. M_e is the pseudomomentum of the error field, adapted from Takaya and Nakamura (2001c), and proportional to the error amplitude (eq. 2.13) scaled by the magnitude of the base state Doppler-shifted wind (eq. 2.18). For migratory waves, $\vec{C_{eU}}$ is the phase velocity vector of the error wave in the direction of the mean wind. The base state upon which errors propagate is thus given by the mean of the forecast and the truth. Note that these two fields diverge as lead-time increases, and their average will move toward a filtered low wavenumber pattern.

For the same plane wave error packet as above, the error wave activity flux can be written as

$$\vec{W}_e = \frac{\psi_{e0}^2}{2|\vec{U}|}\begin{pmatrix} Uk^2 + Vkl \\ Ukl + Vl^2 \end{pmatrix} + \frac{\psi_{e0}^2|K|^2}{4|\vec{U}|}\left(\frac{|\vec{U}||K|^2}{|\nabla Q|} - 1\right)\vec{U} \tag{2.19}$$

$$\vec{W}_e = \vec{C_{eg}}M_e = \vec{C_{eg}}\frac{E}{2|\vec{U} - \vec{C_{eU}}|} \tag{2.20}$$

for stationary Rossby waves in a zonally-propagating packet, this simplifies to $\vec{W}_e = E\frac{\vec{C_{eg}}}{|\vec{C_{eg}}|}$, i.e. the error wave activity flux is a vector in the direction of the error group velocity with the magnitude of the error amplitude. Packets of error are characterized by local maxima in E, with $\vec{W}_e$ oriented parallel to their group velocity. Greater predictability is associated with long-tracking RWPs, typically originating in the western Pacific as discussed in Grazzini and Vitart (2015) and Lillo and Parsons (2017). For reference, idealized schematics of an error packet due to amplitude error versus phase error are shown in Figure 2.1.

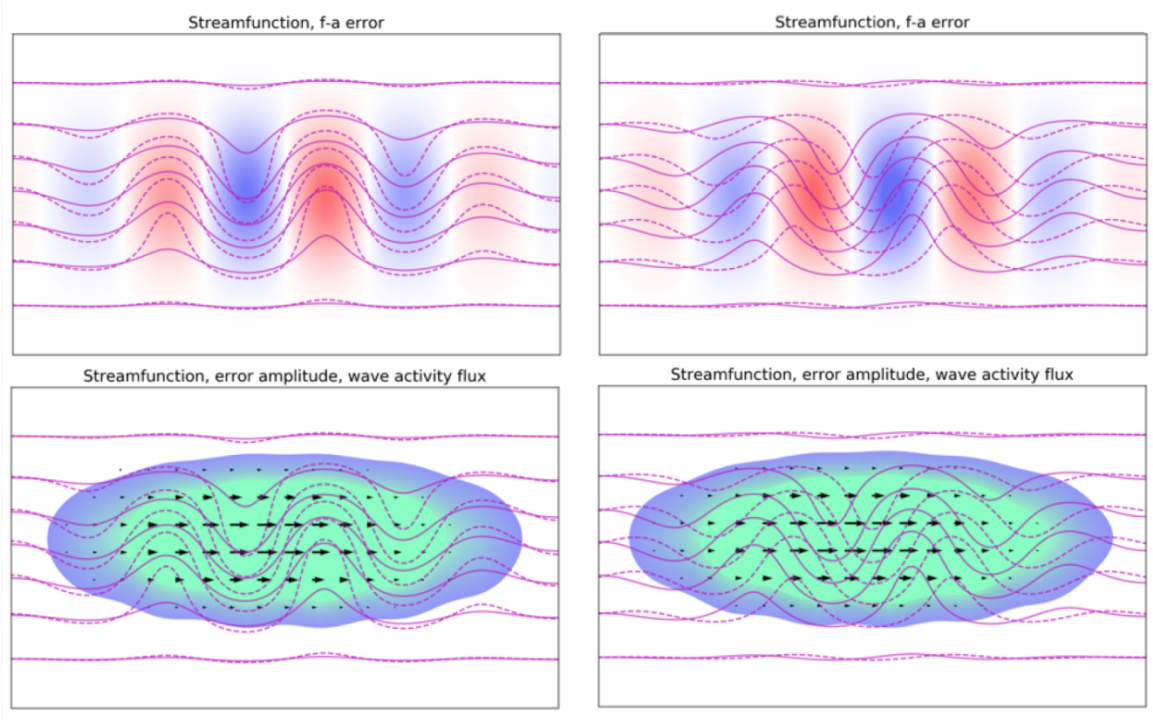

Figure 2.1: Idealized forecast (dashed line) and analysis (solid line) streamfunction configurations for a Rossby wave packet. Color fill in the top row is a simple forecast minus analysis difference. Color fill in the bottom row is the phase-independent error amplitude, and arrows are the error wave activity flux. The left side is an idealized amplitude error and the right side is an idealized phase error. Notice the error amplitude is identical for these two situations.

The diagnostic approach developed in this dissertation is then applied to the April 2011 bust case described in Rodwell et al. (2013) and shown earlier in Fig. 1.2. The evolution of the forecast error is shown in Fig. 2.2. The error at 36 h (Fig. 2.2a) is located over the Great Plains to the south of the Great Lakes near the location of the organized convective system discussed in Rodwell et al. (2013). The linkage between the poor errors over Europe and convective activity over the continent of North America has been noted in previous studies including Grazzini and Isaksen (2002), Rodwell et al. (2013), and Parsons et al. (2019a). However, it can be seen from subsequent times (Fig. 2.2b-d) that forecast error is not tied to any one particular feature, but actually propagates and expands downstream as a wave packet. As errors get channeled in the waveguide, both amplitude and scale of these packets increase. The largest error at 96 h is associated with the appearance of a Rossby wave break (Fig. 2.2d) with errors propagating into the Arctic. A systematic linkage between middle latitude forecasts busts and changes in the Arctic has been demonstrated in Lillo and Parsons (2017). Parsons et al. (2019a) have also shown error propagation into the Arctic in association with poor forecasts over Europe.

While (Fig. 2.2) demonstrates the value of the technique in an example of the bust technique, a more systematic approach is utilized where the rotational error amplitude from Eq. 2.13 and error WAF from Eq. 2.17 are evaluated for all ECMWF 00z and 12z deterministic forecasts from 2008 through 2017. Forecasts are then separated into tri-monthly season, incorporating approximately 1800 different forecasts for each season. Composite season averages of the two error diagnostics are analyzed for 12-hour time-steps.

In the first 24 hours, there are distinct regions favored for initial error growth (Fig. 2.3). In all seasons, there is preference for early growth of rotational errors in the mid-latitude jets over the Atlantic and Pacific oceans. In the winter (DJF; Fig. 2.3a), rotational errors grow first in the eastern Pacific both in the polar jet stream and subtropical jet stream. Composite error WAF shows convergence from both jet streams toward western North America. The African jet also sees early error growth in the winter. By the spring and

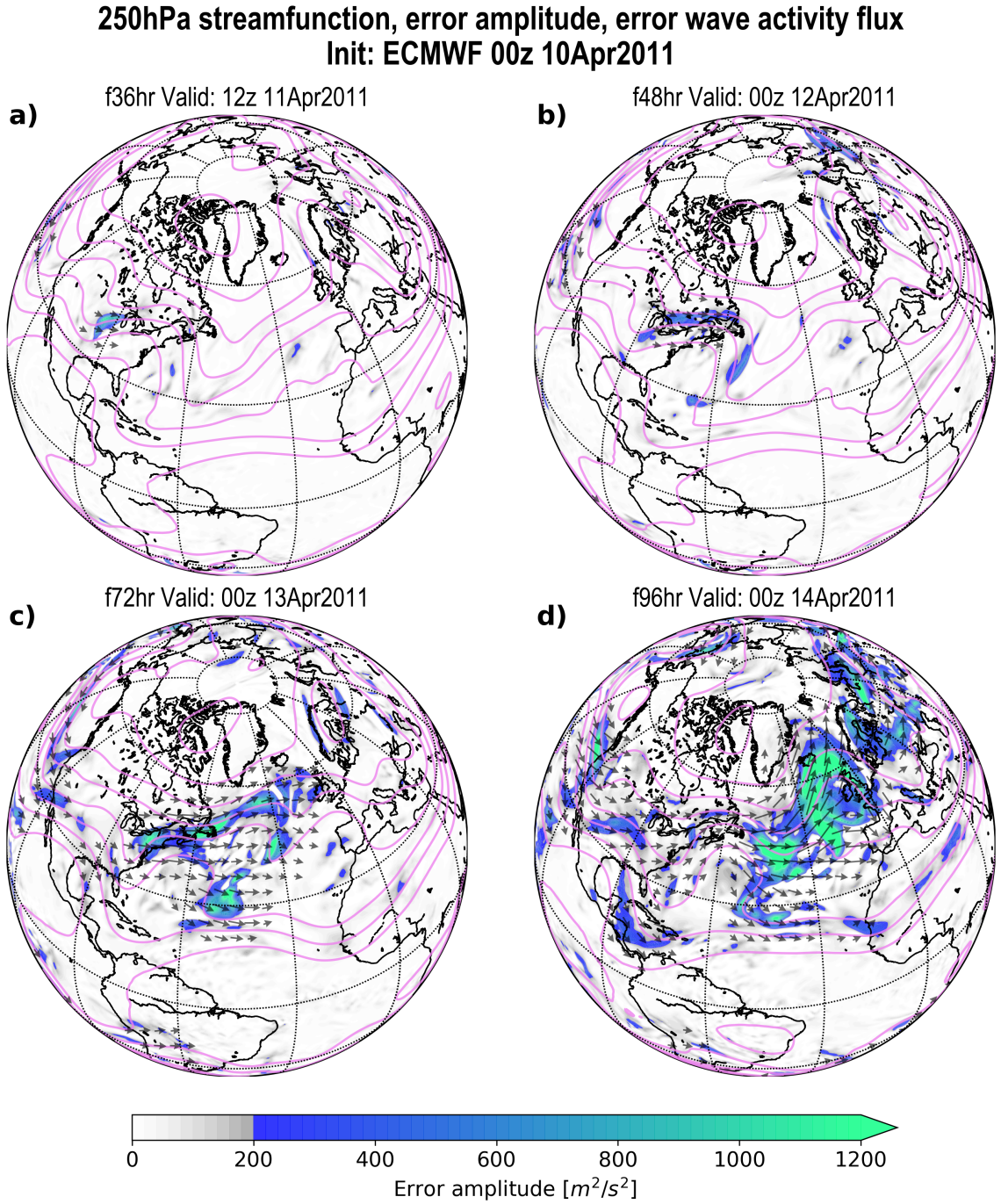

Figure 2.2: Contoured 250 hPa streamfunction average of forecast and analysis, error amplitude (fill), and error wave activity flux (vectors), from the deterministic ECMWF forecast initialized at 00z 10 April 2011 for (a) 36 hours, (b) 48 hours, (c) 72 hours, and (d) 96 hours.

summer, the focus for early error growth turns to eastern Asia and central to eastern North America (Fig. 2.3b,c).

In these late spring to summer months, the greatest rotational errors across the entire northern hemisphere through the first 36 hours are found from the Midwest US to Great Lakes (Fig. 2.3b,c; Fig. 2.4a). Considering the benefit of the most dense upper air observational network in the world, one might expect that short term errors should be smallest over the contiguous United States. The fact that the results shown here directly controvert this hypothesis suggests that this particular seasonally-dependent error growth is not a product of any weakness in the initialization step, but rather is associated with the inherent uncertainty that accompanies a particular atmospheric regime in this part of the world; namely, an environment favorable for convection.

2.3 Re-defining Bust Cases

In order to test new methodologies for tracking error growth as it applies to bust cases, this study initially follows the same rules for selecting bust cases as first defined by Rodwell et al. (2013). The domain of interest is a rectangle on a latitude-longitude grid over the Europe sub-continent, between $35^oN - 75^oN$ and $12^oW - 43^oE$. The thresholds to identify busts considered 500 hPa height forecasts at day-6 lead-time, using an ACC of less than 0.4 and an RMSE greater than 60 m. The combination of the two metrics is meant to ensure both a phase error and magnitude error.

To further explore the concept of a bust in this study, ten years of operational model runs from the European Centre for Medium Range Forecasts (ECMWF) between 2008 and 2017 were accessed from the THORPEX Interactive Grand Global Ensemble (TIGGE; Bougeault et al. (2010), Swinbank et al. (2016)) at a 1-degree by 1-degree spatial resolution and 12-hour time resolution. Over the 10-year period that was utilized, the horizontal resolution increased from T799 on a triangular grid (approximately 25 km), to O1280 on a octahedral grid (approximately 9 km). The vertical resolution increased from 91 levels

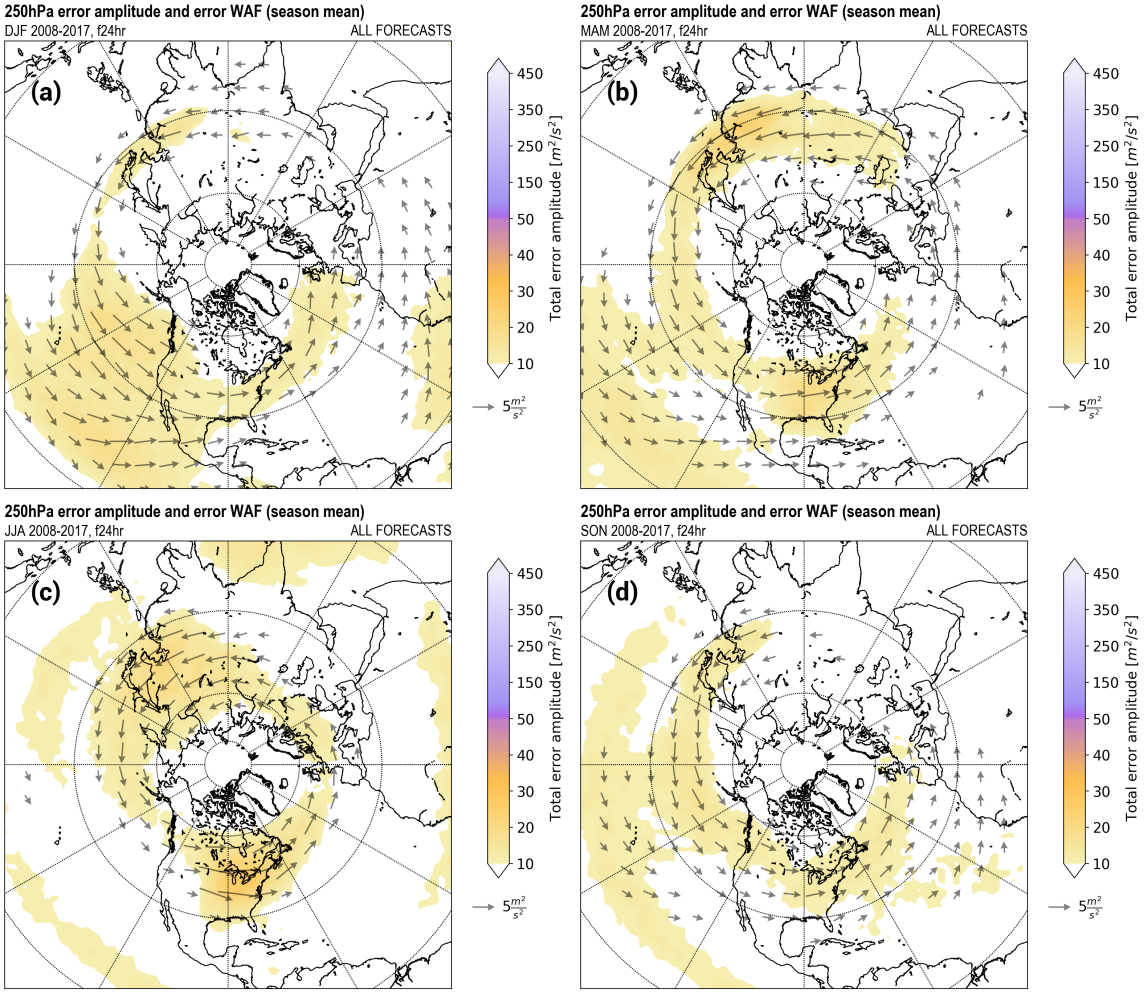

Figure 2.3: Average of all 2008 to 2017 ECMWF forecasts' 250 hPa rotational error amplitude at 24-hour lead-time for (a) winter (DJF), (b) spring (MAM), (c) summer (JJA), (d) fall (SON). Arrows represent the average error wave activity flux vectors.

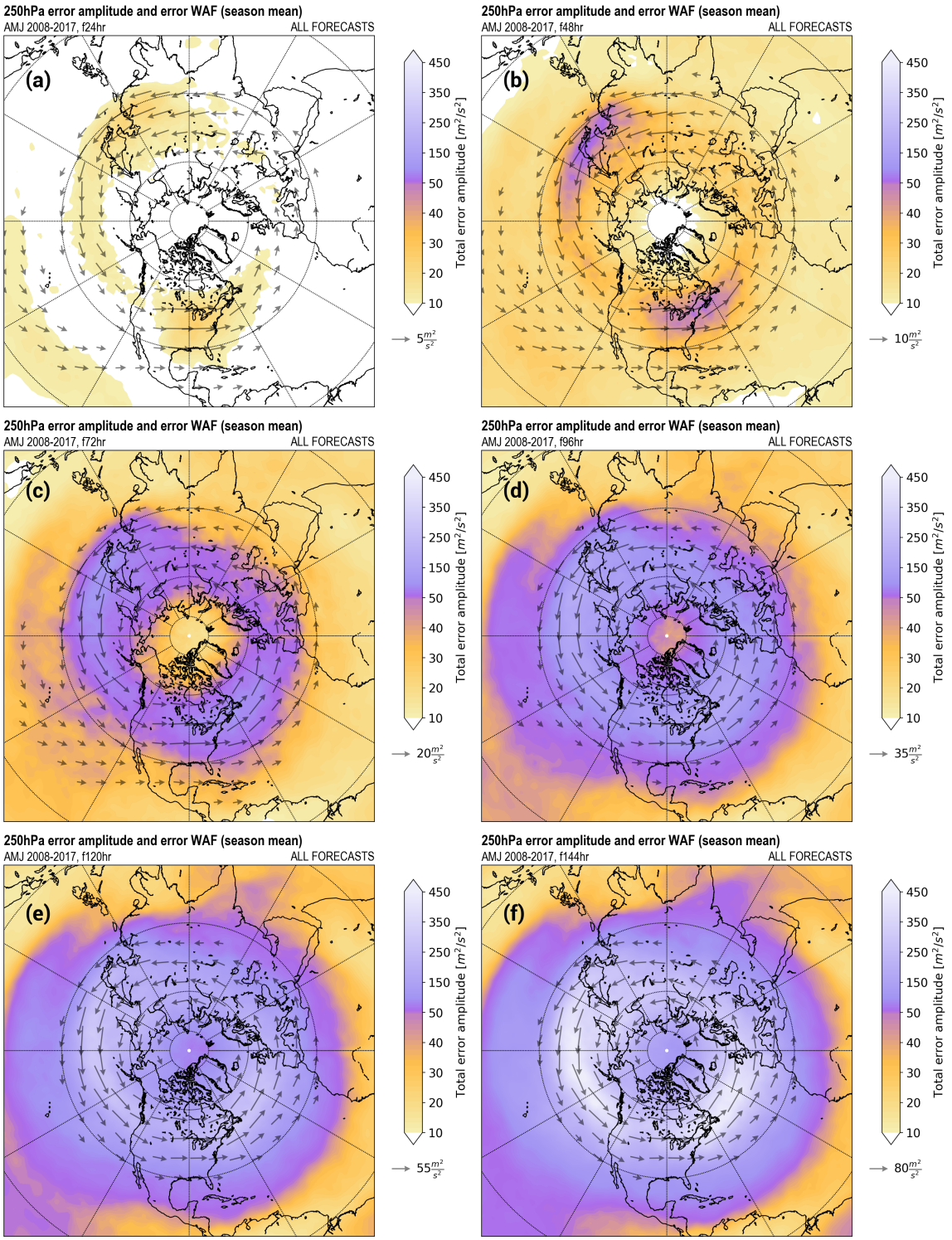

Figure 2.4: Average of all 2008 to 2017 ECMWF forecasts' 250 hPa rotational error amplitude for April-May-June (AMJ) at a lead-time of (a) 24 hours, (b) 48 hours, (c) 72 hours, (d) 96 hours, (e) 120 hours, and (f) 144 hours.

to 137 levels, with the model top at 0.01 hPa (approximately 80 km). In this analysis, we focus on the operational forecasts from the ECMWF generated with the Integrated Forecast System (IFS). The model employs a hydrostatic with convection parameterized and spectral dynamical core.

In this analysis, the anomaly correlation coefficient (ACC) defined by Wilks (2006)

$$ACC = \frac{\overline{(f-c)(a-c)}}{\sqrt{\overline{(f-c)^2}\,\overline{(a-c)^2}}} \tag{2.21}$$

The root mean square error (RMSE) is given by

$$RMSE = \sqrt{\overline{(f-a)^2}} \tag{2.22}$$

Based on the specific focus of Rodwell (2012) on the convective season over the central United States as a period of heightened bust potential, the same season is initially examined in this study, defined here as April through June (AMJ). Compiled over ten years of forecasts from 2008 through 2017, RMSE between the 10th and 90th percentiles follows an exponential growth curve through day-7, followed by a gradual decrease in growth rate from day-7 to day-10 (Figure 2.5, left). The distribution of forecasts in this inner 10% to 90% range is close to Gaussian. Instances of especially poor forecast performance are represented by the long tail in the distribution that exists at greater than 90%. In defining bust cases, the lead-time of 6 days used by Rodwell is also maintained here. The distribution of day-6 forecast RMSE by year demonstrates the consistent shape of an inner Gaussian curve with a long tail in the highest 10 percent of cases (Figure 2.5, right). Busts are identified as those forecasts in the tail, with 500 hPa height RMSE greater than the 90th percentile of all forecasts in AMJ 2008 through 2017.

Using the error amplitude metrics developed above, we can compare composite averages for bust cases to averages for good cases. Bust cases are defined by the highest 10 percent of RMSE over Europe at day-6, and good cases are defined by the lowest 10 percent. Our focus was on the same April-May-June (AMJ) period, in the ten-year period from

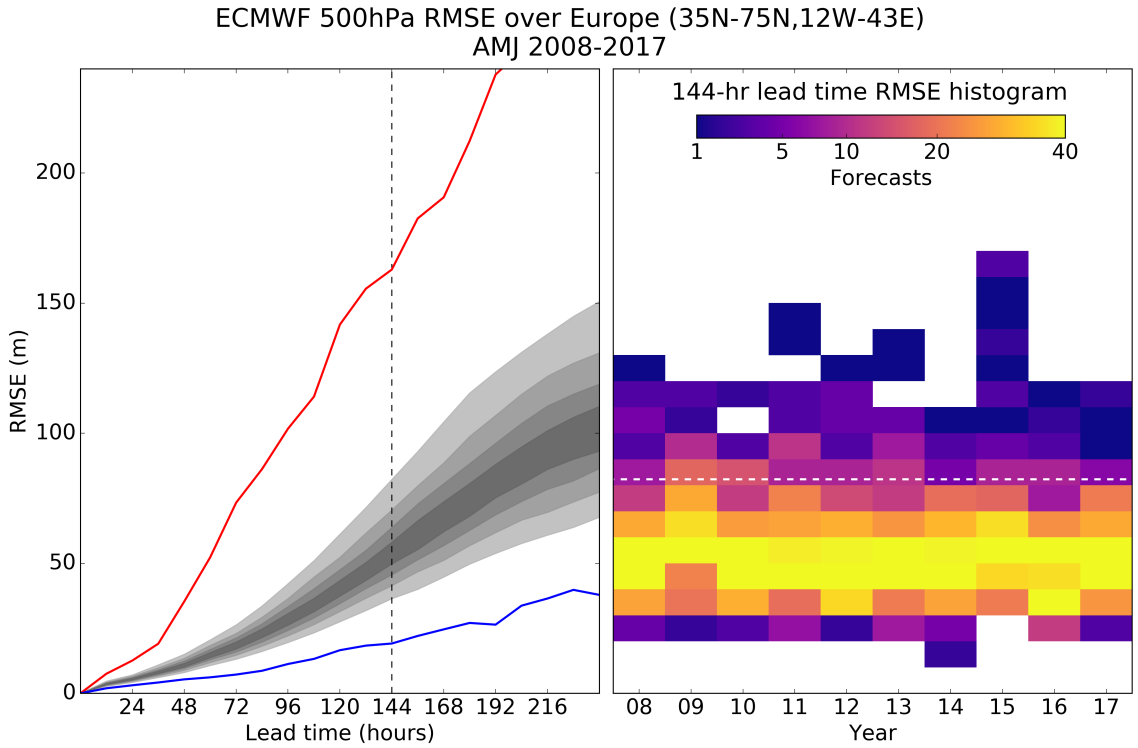

Figure 2.5: Left: Percentile distribution of 500 hPa height RMSE by lead-time of all ECMWF forecasts in April-May-June 2008 through 2017. Each step of gray shading represents a 10% increase toward the median, with the lightest shade bounding 10%-90% and the darkest shade bounding 40%-60%. The minimum and maximum are given by the blue and red lines, respectively. Right: Histograms by year of 500 hPa height RMSE at 6-day lead-time. The white dashed line denotes the 90th percentile.

2008 to 2017. With twice-daily model runs, this amounts to 1,820 total forecasts, with 182 bust cases and 182 good cases.

We find that rotational errors in bust cases do not exhibit significant differences from good cases in the first 48 hours of the forecast (Fig. 2.6). The region over North America where previous studies (Grazzini and Isaksen (2002), Rodwell et al. (2013), Rodwell et al. (2018), Parsons et al. (2019a)) have propose MCSs to play a role in initiating forecast busts (Fig. 2.6a) actually have a smaller error in the bust cases. This difference, however, is not statistically significant suggesting that other downstream processes likely play a significant and necessary role in causing poor forecasts over Europe. In the subsequent 48 hours, errors grow faster over the North Atlantic in bust cases, and significant differences emerge by 3-day lead time. At 4-day lead time (2.6d), bust cases have substantially larger rotational errors over the northeastern Atlantic into western Europe. These errors are statistically significant and are located near the large errors and Rossby wave break shown earlier for the April bust case (Fig. 2.2).

2.4 Discussion and conclusions

In this chapter, we present the techniques developed for our subsequent investigations of the predictability of the two extreme events and our study of the forecast busts and the impact of diabatic processes. This technique was applied to one of the forecast bust cases (April 2011) presented by Rodwell et al. (2013) showing that the error originated in the area associated with an MCS. The error was subsequently shown to propagate downstream and grow in amplitude with the appearance of a Rossby wave break over the North Atlantic (Fig. 2.2).

Beyond this bust case, the technique was also applied to the ECMWF IFS over the period 2008-2017 with the error investigated by season 2.3. The errors tended to be largest in the middle latitude jet stream and to a lesser degree within the subtropical jet. Seasonal differences were observed in the 24h forecast with large errors over much of the tropics

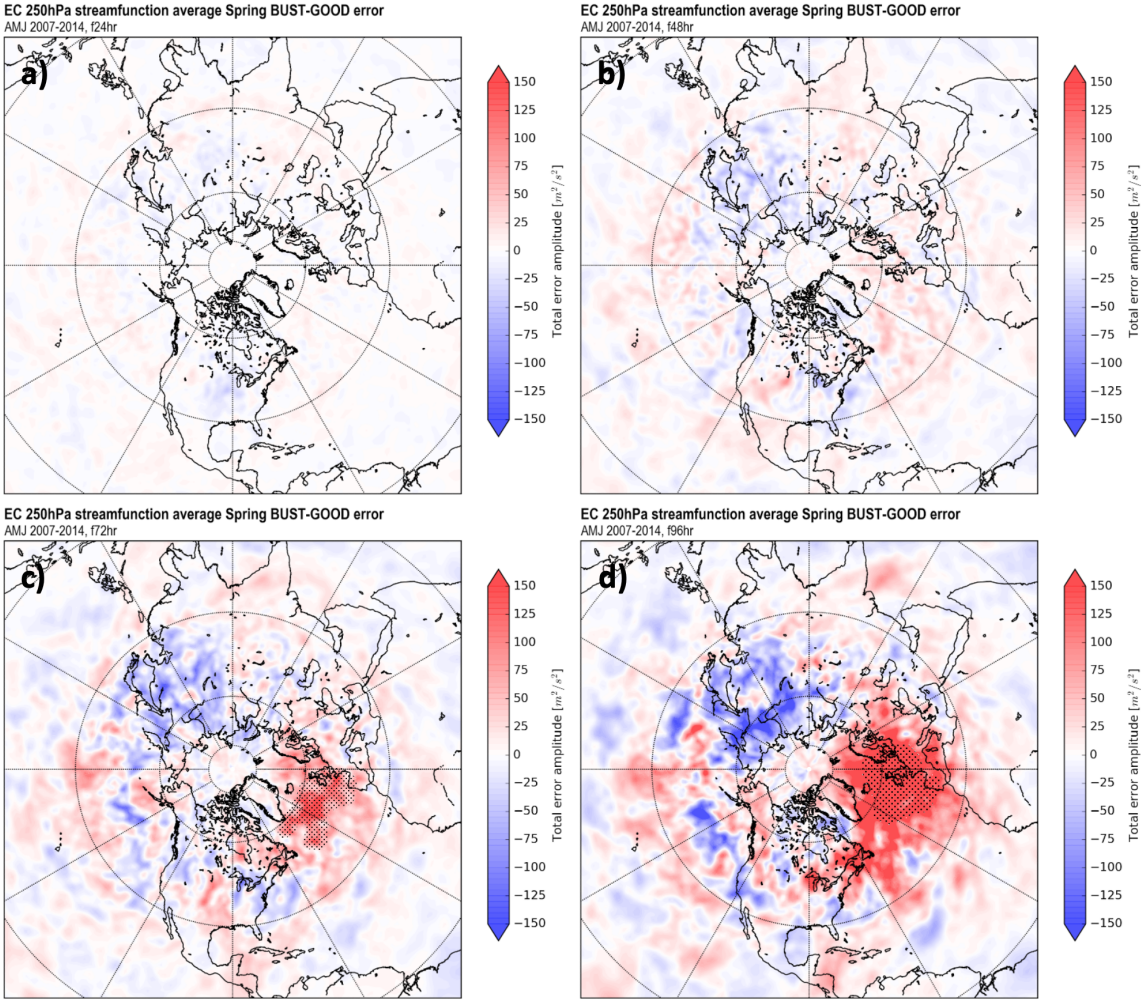

Figure 2.6: Composite difference of 250 hPa rotational error amplitude for April-May-June (AMJ) bust forecasts minus good forecasts, defined as the worst and best ten percent of day-6 RMSE over Europe. Stippling marks 95 percent confidence. Panels are for forecast lead times of a) 24 hours, b) 48 hours, c) 72 hours, and d) 96 hours.

and middle latitudes over the eastern Pacific. Smaller errors were also observed over the fall and winter over Asia with large errors over both North American and east Asia during the summer that extended eastward over the Altantic and Pacific Oceans, respectively. Further investigation of how the errors evolved with forecast time during the spring and early summer (April, May, June) was also undertake (Fig. 2.4). These results also show that the entrance regions of the Atlantic and Pacific are regions of rapid growth rates with the errors subsequently increase in magnitude and expand in area within the wave guide.

While the concept of a bust has proven useful to understand the reasons for forecast errors, in this chapter the general concept of a bust was explored within the framework of contrasting the 10% worst vs 10% best forecasts. This approach allows quantification of the error origins in NWP, and distinguish those errors that are prone to upscale growth. We show that the forecast bifurcation from truth is less important at the origin of the error, but rather it is the error growth within the downstream waveguide that is consequential to a bust event. It is the sensitivity of the downstream environment to the introduction of error that is paramount in the development of a large-scale busted forecast. For example, while errors in the treatment of MCSs over the continental North America was been associated with forecast busts over Europe, no statistically significant difference between the best and worst forecast in the region containing MCSs. Instead the difference between these ”good” and ”bad” forecasts was found to exist over the North Atlantic and western Europe, near the same region as the error growth occurs in the investigation of the April 2011 bust event.

Finally, we note that forecast error plagues all parts of the globe, however with preference on different scales, different levels, and different variables. For example, in the tropics, 500 hPa heights have little variance and errors will be small albeit not necessarily reflective of the true and consequential error in the atmosphere. Thus, this error in the tropics may be more appropriately shown by divergence or velocity potential in the upper levels of the troposphere. In addition, those errors with greatest impact in extratropical latitudes

are focused on subseasonal to seasonal time scales, such as associated with the Madden-Julian Oscillation. That being said, error growth in the tropics is outside the scope of this work. The focus of this study is on mid-latitude medium-range forecast busts. Following the pioneering investigation of busts over Rodwell et al. (2013), this study begins with an investigation described in the subsequent chapter focused on busts over Europe.

Chapter 3

Attribution of Error Growth From Random Gaussian Perturbations in a Model

This chapter explores the concepts of the importance of downstream propagation and amplification of the forecast error within the wave guide that was found in the previous section. Some of the background for this chapter is based on Parsons et al. (2019a) in which the author of this dissertation played a major role as second author of this study. The main portion of this chapter, however, is based on numerical modeling experiments that will be subsequently submitted for publication with Lillo as the first author.

3.1 Case Background

A series of relatively poor medium-range forecasts over Europe occurred during June 2015 as discussed in Parsons et al. (2019a). This period of reduced model performance coincided with the Plains Elevated Convection At Night (PECAN; Geerts et al. 2017) field and modeling campaign that summer. The purpose of this field project included measurements aimed at advancing understanding and predict of the initiation, structure and dynamic mechanisms that support maintenance of long-duration convective systems at night over the Plains. The overarching goal was to explain the observed nocturnal convective maximum over this region.

PECAN benefited from a period of frequent MCS activity in June 2015 (Geerts et al. 2017). Additionally during this time, Tropical Storm Bill (Berg 2015) made landfall along the Texas coast on 16 June and tracked northward through eastern Texas and Oklahoma which had just experienced their wettest May on record. The remnants of Bill proceeded as an MCS across the mid-Mississippi Valley and Ohio Valley into the Mid Atlantic US from 18 through 23 June. Simultaneously, the period from 16 through 23 June featured a fast

zonal jet stream across the northern US into the western Atlantic, as seen in Fig. 3.1a. The multiple long-duration MCSs interacting with this jet fits the conceptual model for error growth and downstream propagation as proposed in Rodwell et al. (2013) and Lillo and Parsons (2017) and as found in the previous chapter.

In the first half of the month, the Hovmoller diagram reveals multiple RWPs tracking across the mid-latitude northern hemisphere (Fig. 3.1b). However beginning around 19 June, this textbook behavior breaks down and transitions to a series of fast short-wavelength troughs and ridges tracking rapidly from the United States across the Atlantic to western Europe. In contrast, the flow downstream over eastern Europe becomes stagnant with a stationary wavenumber-6 trough and downstream ridge (vertical band of southerly winds between 0 and 60^oE in Fig. 3.1).

In order to better understand this difference in the character of the RWPs, a spatiotemporal power spectra was produced for the 250 hPa meridional winds within the middle latitudes between 30^oN and 60^oN and 270^oE to 360^oE in 10-day segments (Fig. 3.2). The regime over the Atlantic in late June is characterized by a wavenumber around 10 (wavelength less than 500 km at 45^oN) and a period around 3 days (Fig. 3.2b). This spectral peak is displaced well to the right and upward from the 1979-2018 June average. The normal for June is closer to a quasi-stationary wavenumber-6 pattern. The presence of these short-period (3 day) rapidly moving Rossby waves is relatively unique in past studies of Rossby waves, although Tribbia and Baumhefner (2004) linked these types of RWPs to large errors in climate models. Their finding, together with the results of Parsons et al. (2019a) suggest that the generation of this type of RWP is relevant to accurate prediction in both weather and climate models. Our subsequent study goes beyond previous work by exploring the mechanisms producing these larger errors with the rapidly moving RWPs.

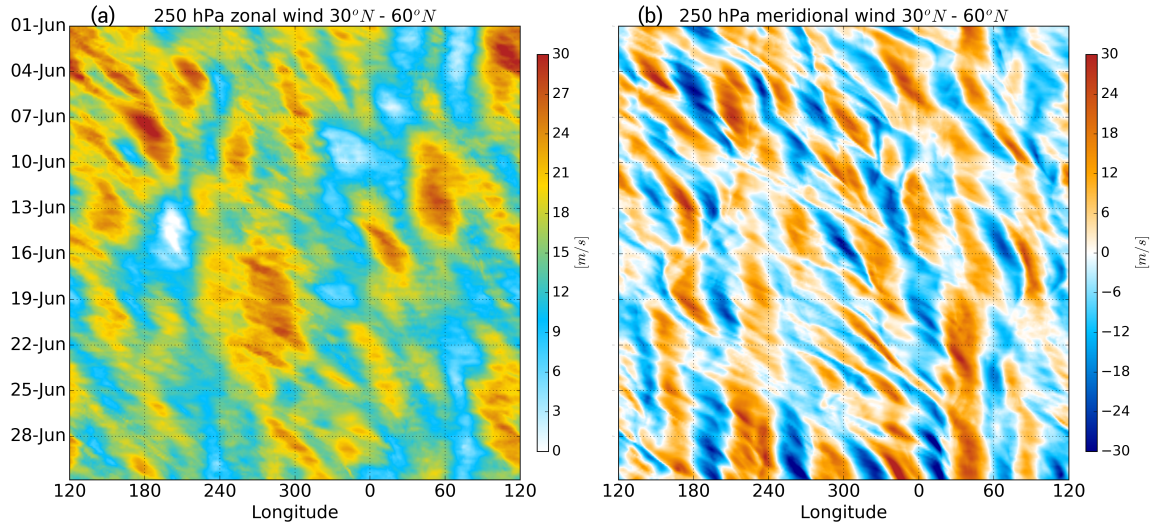

Figure 3.1: Hovmoller diagrams of (a) 250 hPa zonal winds, and (b) 250 hPa meridional winds, averaged between 30^oN and 60^oN. Produced by S. Lillo and included in Parsons et al. (2019a)

3.2 Description of the Numerical Model

This study utilizes the atmospheric component of the Model for Prediction Across Scales (MPAS; Skamarock et al. 2012). The model's dynamical core is built on an unstructured Voronoi mesh with an Arakawa C-grid discretization. Voronoi partitioning of cells allows for smooth transitions to regional refinement at higher resolution, without needing nested grids. For this investigation of error growth and propagation across the Atlantic, the model is run on a mesh with variable horizontal resolution. An elliptic region of refined resolution is centered on 40^oN / 60^oW with the major axis along the 40^oN parallel. The result is an approximate horizontal resolution of 15 km in the middle latitude across North America, the Atlantic and western Europe. The mesh outside of this region transitions to a quasi-uniform 60 km resolution around the rest of the globe (a total of 535,554 cells; Fig. 3.3). The model uses a hybrid terrain-following vertical coordinate system (Klemp 2011) and was run with 55 levels up to a top at 30 km.

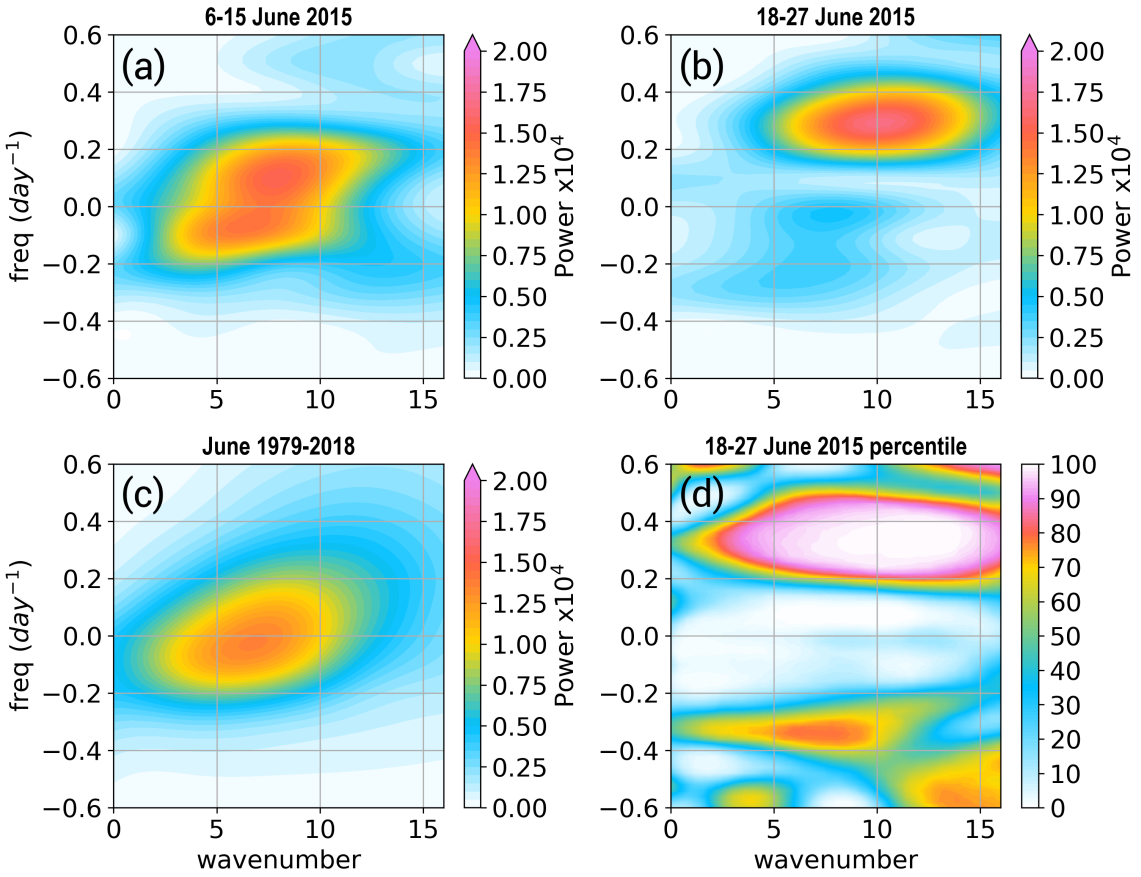

Figure 3.2: Spatiotemporal power spectra for 250 hPa meridional winds between 30^oN and 60^oN and 270^oE to 360^oE in 10-day segments. a) The segment from 6-15 June 2015. b) The segment from 18-27 June 2015. c) The average of all 10-day segments in June from 1979 to 2018. d) The percentile of the power in (b) compared to all 10-day segments in June from 1979 to 2018. Produced by S. Lillo and included in Parsons et al. (2019a)

.

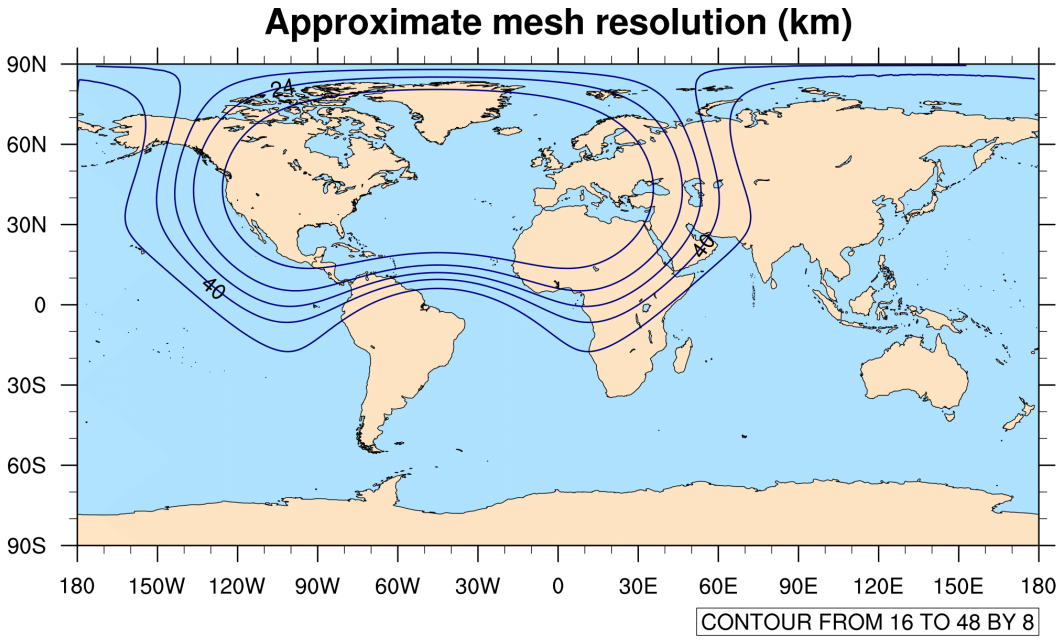

Figure 3.3: The approximate horizontal resolution (km) of the mesh used in the MPAS identical twin experiment.

The MPAS runs in this study employ a physics suite from the Advanced Research Weather Research and Forecasting (WRF) model. This suite includes the Monin Obukhov surface layer scheme (Grell et al. 1994), the Yonsei University (YSU) planetary boundary layer (PBL) scheme (Hong and Pan 1996), YSU gravity wave drag, Thompson double-moment microphysics (Thompson et al. 2004), RRTMG shortwave and longwave radiation (Iacono et al. 2008) called every 30 minutes, and the new Tiedke convection scheme (Tiedtke 1989) modified for WRF (Zhang et al. 2011).

3.3 Investigation of Error Growth

3.3.1 Control Simulation

A control run (CTRL) was initialized with the NCEP GFS 0.25-degree global grid zero-hour forecast from 00z 19 June 2015, and ran with the model configuration described above for seven days. The simulations cover the period of large error growth and rapidly moving RWPs and goes beyond the observational analysis presented in Parsons et al. (2019a). The synoptic evolution in the MPAS realization of the atmosphere is examined using the CTRL simulation (Fig. 3.4). This analysis serves both to evaluate the legitimacy of the evolution compared to the observed atmosphere, and to identify features of the flow that we may later turn attention toward as cultivators of model error and uncertainty.

The remnants of Tropical Storm Bill can be seen as a region of low OLR tracking across the Ohio Valley on 20 June (Fig. 3.4a,b), and into the Mid Atlantic and east of New England on 21 June (Fig. 3.4c,d,e). Poleward outflow can be seen in the irrotational wind vectors north and east of Bill (Fig. 3.4a), which assists in enhancing a jet streak over New England and south of Nova Scotia. This jet streak quickly propagates into a downstream trough on 21 June. Meanwhile a long-duration MCS can be seen marked by a separate region of low OLR tracking across the northern Plains and Great Lakes on 20 June, and another behind it during 21 and 22 June. Similar jet streak accelerations occur in response to the upper

level outflow from these convective systems. By 00z 22 June, the series of jet streak pulses dispersed downstream form a wavenumber-3 pattern in this sub-domain (Fig. 3.4e).

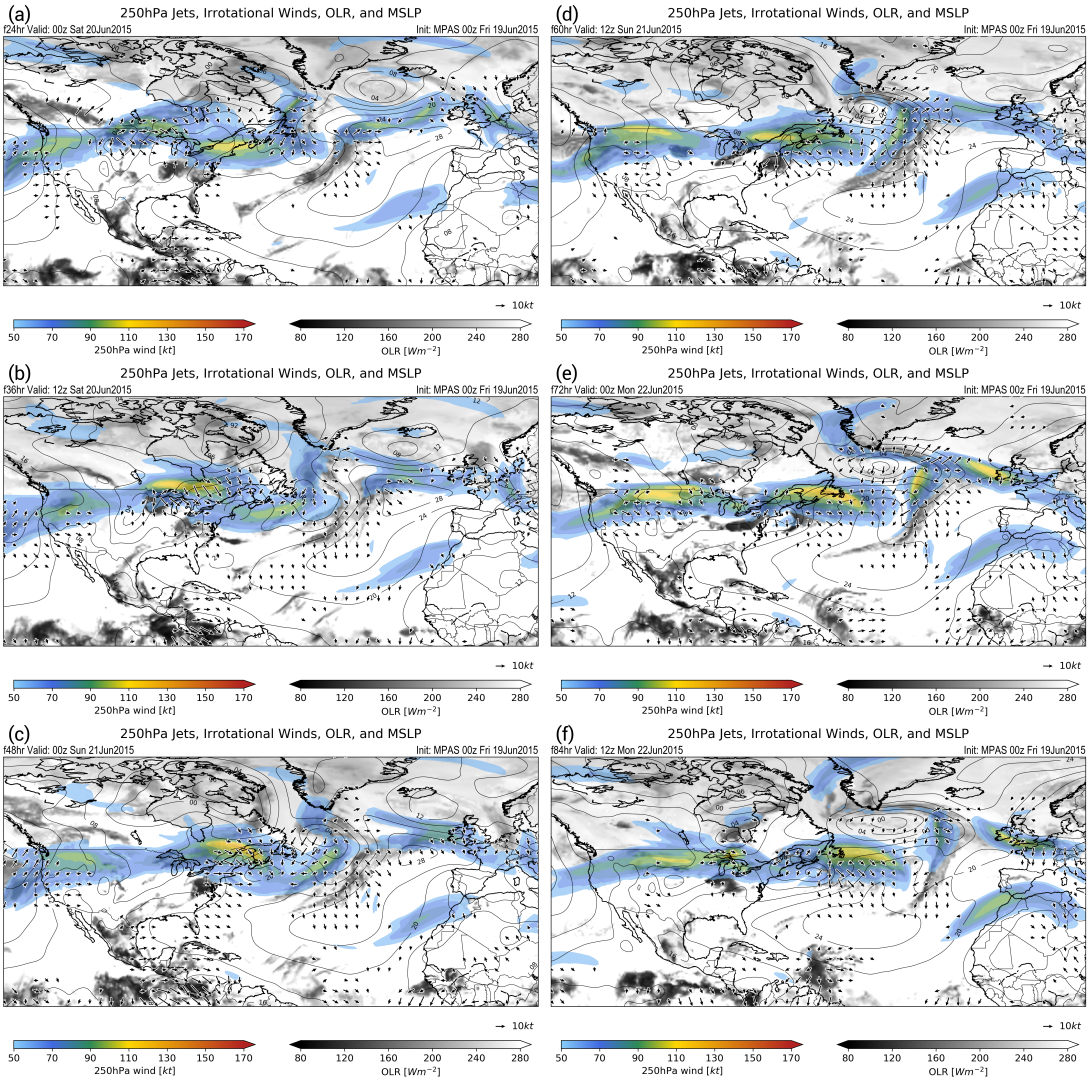

Figure 3.4: CTRL run synoptic overview: 250 hPa jet stream winds (color fill starting at 50 kt), outgoing longwave radiation, and mean sea level pressure contoured every 4 hPa. Panels are every 12 hours beginning at 00z 20 June 2015: a) 00z 20, b) 12z 20, c) 00z 21, d) 12z 21, e) 00z 22, and f) 12z 22 June 2015.

The atmosphere is a continuous fluid, and human inclination is to establish attribution and label features in this fluid. This practice has been very beneficial with advancing understanding in the field of synoptic meteorology, but it also has its limitations that can lead

to flawed discussion and conclusions when complex fluid flow is forced into boxes. Such may be the case with the evolution of the atmosphere during the latter half of June 2015. For example, the rapidly moving RWPs during this period appear quite differently than the conventional, textbook structure evident in the RWPs in the Hovmoller diagram early in the month (Fig. 3.1). The presence of these high wave number RWPs and their strong linkage to severe, rapidly moving MCSs also does not fit convectional models of MCSs over the Great Plains (Parsons et al. (2019a)). In regard to the later point, these experiments employ convective parameterization given the horizontal resolution of the simulations.

3.3.2 Identical Twin Experiments

Following the control run, subsequent identical twin simulations were initialized from the control run restart files every 24 hours for the next five days (PTRB20, PTRB21, PTRB22, PTRB23, and PTRB24) and run to the last valid time from CTRL. The initial conditions for each of these twin simulations were created by perturbing the corresponding forecast time from CTRL. Similar to Judt (2018), the perturbed initial conditions were generated by adding Gaussian noise to the potential temperature fields in the CTRL restart files. The random noise was selected from a Gaussian distribution with a mean of zero and standard deviation $\sigma = 0.05$ K, and truncated at a magnitude of 3σ. The perturbed simulations were run with a model configuration identical to CTRL. Departures of the perturbed simulations from CTRL are hereafter referred to as errors, with the control simulation considered as the truth.

The initial introduction of errors in the perturbed simulations is geographically uniform, but our results in the previous section suggest that more rapid and larger error growth will occur in regions of greatest sensitivity. By initializing new simulations every 24 hours, we

can obtain a picture of how the short-term sensitivity of the error evolves during the period simulated by CTRL. Thus, we can analyze the spatiotemporally varying intrinsic predictability of the flow configuration. The growth and propagation of errors in the medium-term as they project onto larger scales are investigated using the six-day simulation and errors from PTRB20.

PV error and error tendency are evaluated using Eq. 2.6. All output fields on the variable horizontal mesh are interpolated back to a 0.25 by 0.25-degree grid and vertically interpolated to 51 evenly-spaced isentropic levels between 300 K and 400 K. Advection and diabatic terms are calculated on these isentropic levels. Error tendencies on these 51 levels are then averaged in two atmospheric layers defined by the three-dimensional Ertel PV field averaged at each time step from the two simulations. A tropospheric-deep (TROP) layer includes all isentropic levels in a given column that are less than 2 PVU, and an upper troposphere to lower stratosphere (UTLS) layer includes levels between 2 PVU and 6 PVU.

This layer definition is desired over Baumgart et al. (2018) which uses a single isentropic surface and thus would only intersect the tropopause at a specific latitude, and Judt (2018) which used fixed height levels to define the troposphere as 0 to 11 km and stratosphere as 18 to 29 km. Instead, this dissertation study analyzes the dynamic tropopause, capturing the level of jet streams and pathways for Rossby wave dispersion. From the TROP and UTLS layers, diabatic error growth is further partitioned into the contributions from parameterized processes in the model. The processes analyzed here include longwave radiation (RADLW), shortwave radiation (RADSW), planetary boundary layer (PBL), and convection (CONV).

The divergent error amplitude was calculated from the irrotational component of the 250 hPa wind and corresponding velocity potential, following Eq. 2.14. Also shown is the velocity potential derived from the mean of the CTRL and PTRB irrotational wind, with the first three spherical harmonics removed in order to focus on synoptic and mesoscale features. Areas of large divergent error are most commonly found coinciding with mean

negative velocity potential (Fig. 3.7). This finding suggests an important asymmetry in which regions of lifting motion forcing upper level divergence are associated with greater error than areas of upper level convergence. Herein lies a key to upscale error growth where sources of strong upward motion force upper level divergence with associated errors that subsequently impinge on PV gradients and trigger a wave response with associated rotational errors. This finding is consistent with references discussed earlier that highlight the importance of errors occurring when diabatic processes influencing the jet stream are poorly represented in the model.

By day-6 of the PTRB20 simulation (day-7 of CTRL), valid 00z 26 June, the error has organized into a synoptic-scale packet over Europe. This finding is consistent with the knowledge stated earlier that this was a low-skill forecast period over Europe for the deterministic ECMWF. Additionally, as seen developing in Fig. 3.5 d, e, and f, error splits both poleward and equatorward from the mid-latitude flow. Most notably, an LC1 cyclonically breaking trough over Morocco in the mean flow carries a packet of error southward. This particular error is absent in the subsequent perturbed simulations (Fig. 3.6b,c,d,e) again revealing the likely association of forecast error with the ability to represent Rossby wave breaking in association with intensifying RWPs. The day-6 divergent error in PTRB20 shows growth similar to the rotational error (Fig. 3.6a) over the North Atlantic as well as Europe (Fig. 3.7a). Note that the divergent error amplitude is minimal in association with the LC1 trough over Morocco as well as with the large EWAF over western Canada. Interestingly, it is these areas that see large reduction of rotational error in the subsequent perturbed simulations after PTRB20. In contrast, the one location with consistently the largest errors at 00z 26 June in each simulation is the north-central Atlantic.

3.4 Discussion and Conclusions

Prior work (e.g., Grazzini and Isaksen (2002), Rodwell et al. (2013), Rodwell et al. (2018), Parsons et al. (2019a)) has found that large, medium range forecast skill is associated with

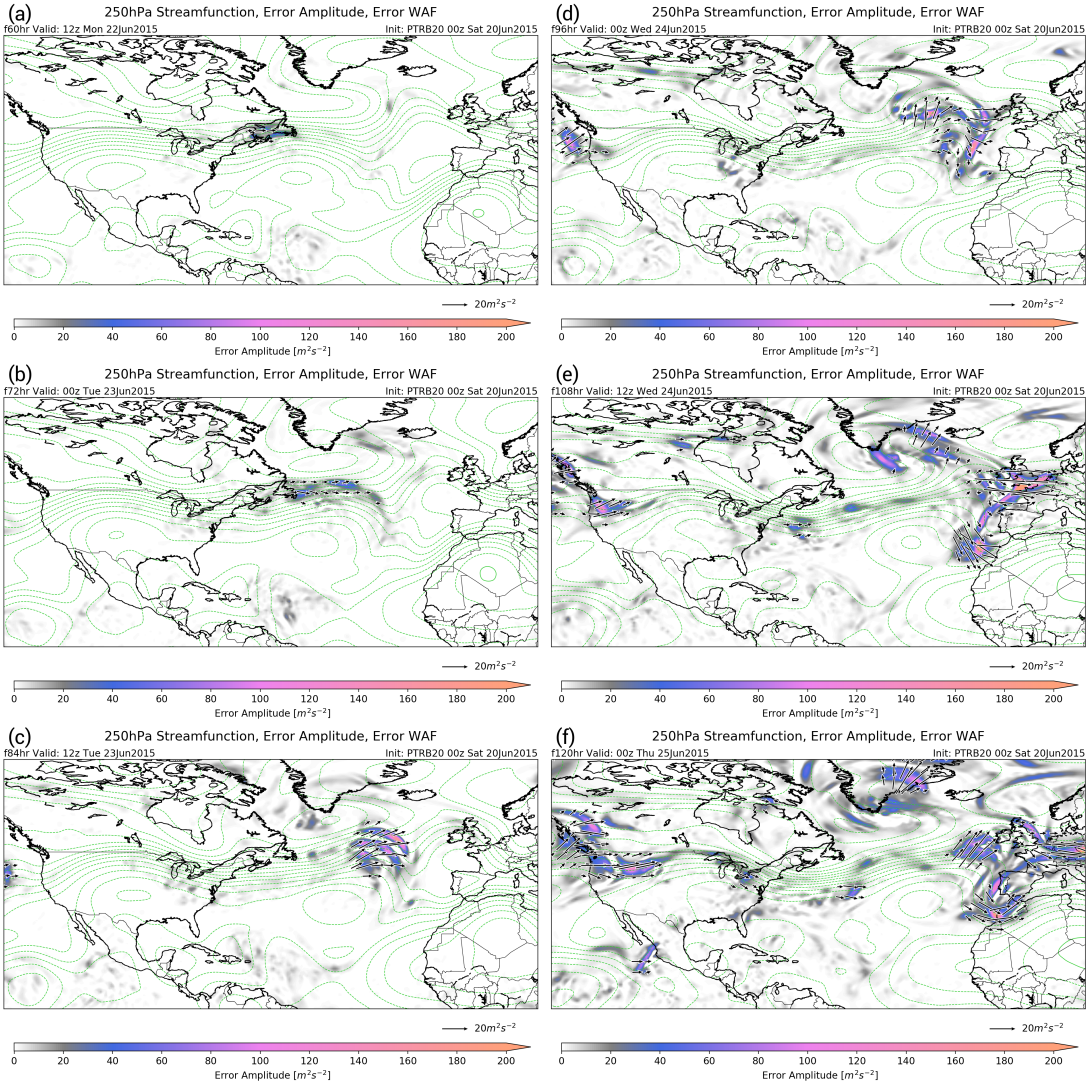

Figure 3.5: 250 hPa streamfunction, error amplitude, and error wave activity flux from PTRB20. Streamfunction is contoured every $5 \times 10^6 m^2 s^{-1}$ with the average gradient directed southward. Panels begin at 60-hour lead-time and advance every 12 hours, valid at a) 12z 22, b) 00z 23, c) 12z 23, d) 00z 24, e) 12z 25, and f) 00z 26 June 2015.

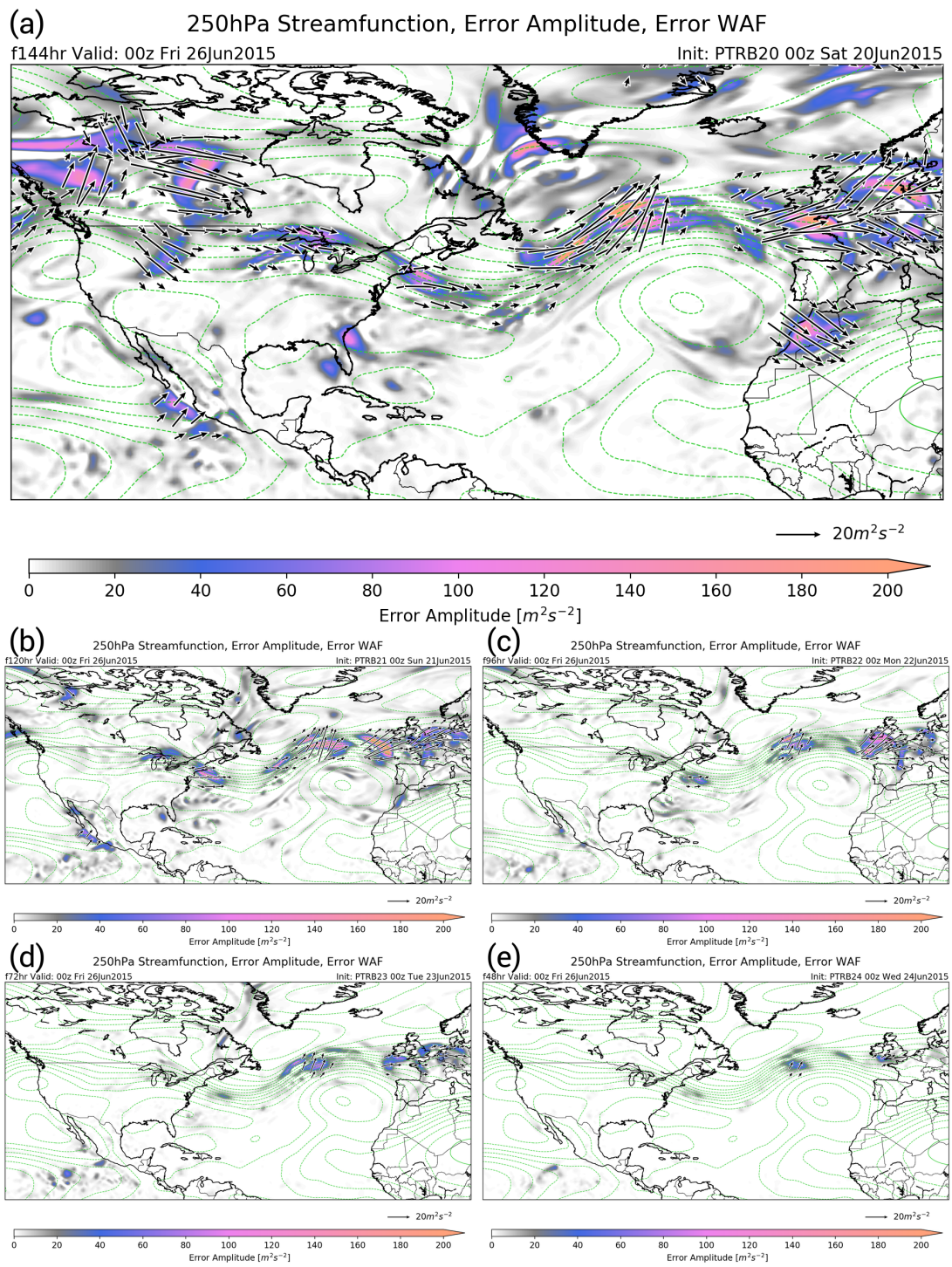

Figure 3.6: 250 hPa streamfunction, error amplitude, and error wave activity flux as in Fig. 3.5, for each of the PTRB simulations: a) PTRB20, b) PTRB21, c) PTRB22, d) PTRB23, e) PTRB24, valid at 00z 2une 2015.

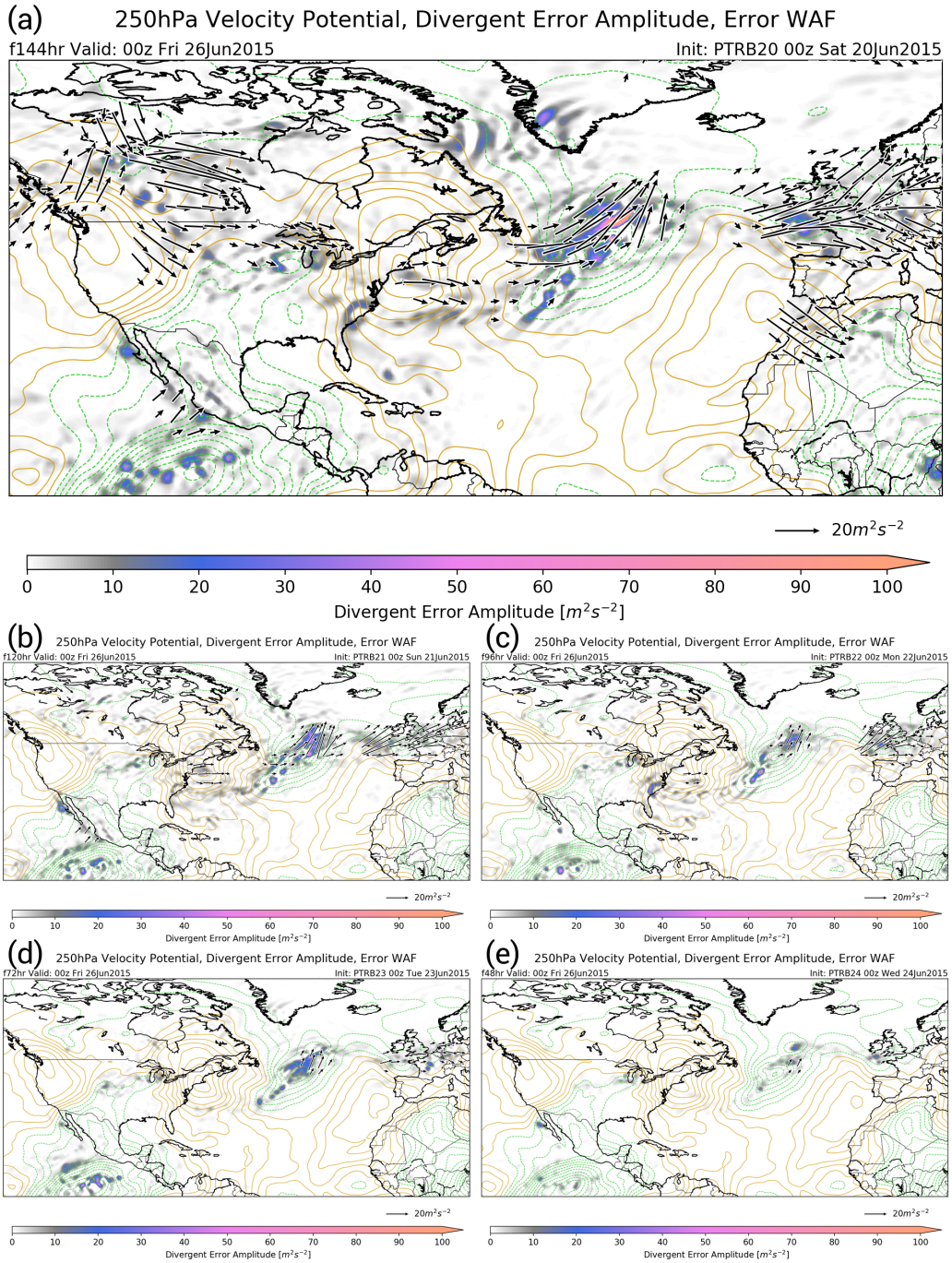

Figure 3.7: 250 hPa velocity potential, divergent error amplitude, and error wave activity flux, for each of the PTRB simulations: a) PTRB20, b) PTRB21, c) PTRB22, d) PTRB23, e) PTRB24, valid at 00z 26 June 2015. Velocity potential is contoured every $5 \times 10^5 m^2 s^{-1}$ with dashed green contours referring to negative values, and solid brown contours referring to positive values.

MCS activity over North America often near the wave guide. A consistent finding is emerging from the results of this and the previous chapter that goes beyond previous studies of periods of low forecast skill over Europe. Specifically, our investigations shows that the subsequent magnification of errors downstream over the North Atlantic plays a critical role. This upscale error growth occurs when sources of strong upward motion force upper level divergence with associated errors that subsequently impinge on PV gradients and trigger a wave response with associated rotational errors. As noted earlier, this finding provides an important asymmetry in which regions of lifting motion forcing upper level divergence are associated with greater error than areas of upper level convergence. The results of the simulations presented in this chapter are consistent with our previous exploration of the April 2011 bust case and our systematic depictions of the behavior of good vs. poor forecasts.

Thus, the treatment of diabatic processes near the wave guide is a critical need in the quest to improve forecast skill in weather and climate models. Our findings amplify recent work (e.g., Gray et al. (2014), Rodwell et al. (2013), Lillo and Parsons (2017), Parsons et al. (2019a)) that highlight the importance of errors occurring when diabatic processes influencing the jet stream are poorly represented in the model. However, our simulations and the results shown earlier in the previous chapter provide specific clarity on the cause of forecast busts over Europe during the warm season. In particular, showing that the downstream amplifications of errors is important, defining the mechanism for the error amplification and a suggestion that these busts can be associated Rossby wave breaking. In the study to date, we have focused on the errors associated with middle latitude processes. In our subsequent chapters, we will investigate the dynamics and forecast errors associated with a extreme event associated with polar-middle latitude interactions (chapter 4) and then an extreme associated with a middle-latitude-tropical interaction (chapter 5).

Chapter 4

The Role of a Tropopause Polar Vortex on the January 2019 Arctic Outbreak

This chapter utilizes observations and numerical modeling to investigate the predictability of and the dynamical and thermodynamical processes associated with an extreme cold air outbreak over North America. The event that was found to be closely linked with a Tropopause Polar Vortex. This finding led to a climatological investigation of the linkages between these upper-level disturbances and cold air outbreaks east of the Rocky Mountains of the continental United States. The text from this chapter is based upon and largely taken from Lillo et al. (2021).

4.1 Introduction

Exceptionally cold temperatures accompanied by strong winds swept southeastward from Canada into the Midwest, Great Lakes, and Northeast United States (US) during 29 January to 1 February 2019. Daily cold temperature records were broken across the Midwest and into the Northeast with temperatures that competed with all-time record lows on a regional scale (Fig. 4.1). Mt. Carroll, Illinois, for example, recorded the coldest ever state-wide temperature of -39^oC (-38^oF) on January 30. At Chicago O'Hare International Airport (ORD) the temperature dropped to -31^oC (-23^oF) on 30 January, which tied for the 5th all-time coldest temperature in Chicago since 1871 (NWS 2019). The high temperature that same day was -23^oC (-10^oF), recorded at midnight, tying for the 3rd coldest high on record. At 22^oC (40^oF) below the average temperature for the heart of the winter, 30 January was the 2nd coldest day (average of the high and low) in recorded history for ORD. In addition, winds gusting to over 13 ms^{-1} (30 mph) made the temperatures feel even colder, producing a wind chill of -47^oC (-52^oF), which was the 5th lowest since 1929.

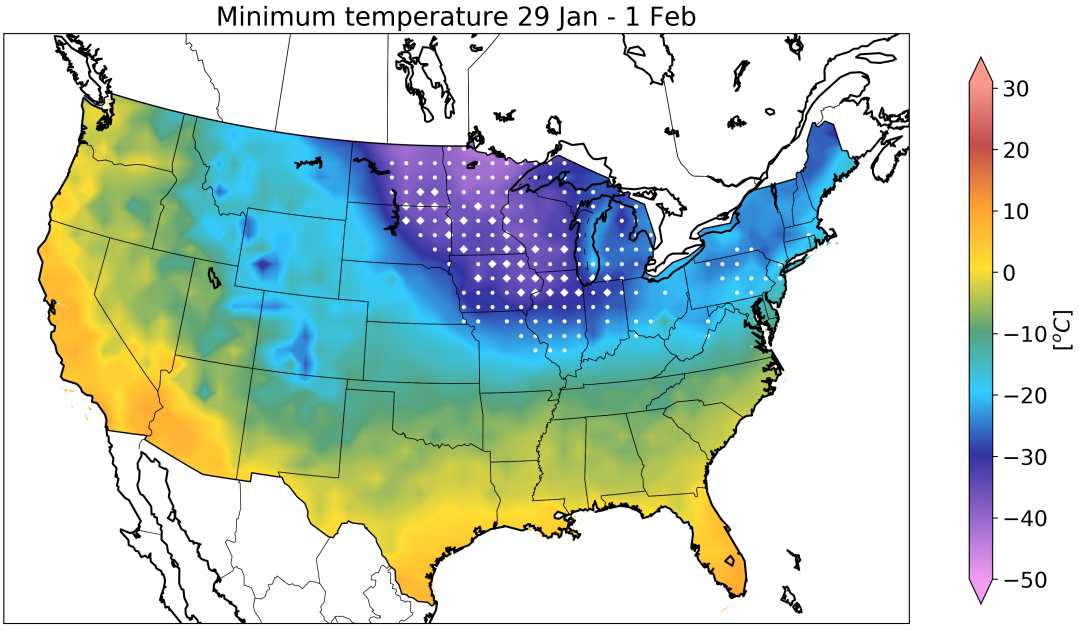

Figure 4.1: Coldest low temperatures (^oC) observed between 29 January and 1 February 2019, from the GHCN. The small circle stippling signifies temperatures that are on average the coldest per year (0.27 percentile of a station's history) and the larger diamond stippling signifies temperatures that are the coldest per 10 years (0.027 percentile).

By the afternoon of the 31st, ORD had spent 52 continuous hours below 0^oF, ranking as the 4th longest duration. In summary, compared to the Arctic outbreak that impacted Chicago and the region in January 2014 (e.g., Screen et al. 2015), the 2019 event was superlative in many categories.

Cold air outbreaks (CAOs) pose significant hazards in the US. Much attention has been given to CAOs impacting the Southeast US due to damage to agriculture, such as Florida citrus crops (Rogers and Rohli 1991; Miller and Downton 1993; Downton and Miller 1993). Extreme cold with CAOs in the northern US has direct impact on human well-being, threatening life and property. For instance, the wind chills observed in January 2019 can cause frostbite in under five minutes. The extreme conditions were implicated in 21 fatalities across the Midwest and Northeast (Gajanan 2019). These conditions also resulted

in closure of schools and business and disruptions to transportation. Both Wisconsin and Michigan declared a state of emergency. Thus, this recent event and its impacts provide the motivation for further investigation of the meteorological factors responsible.

There have been a variety of definitions for CAOs in past studies. Konrad and Colucci (1989) defined CAOs as minima in a time-series of 850 hPa temperatures averaged over the eastern US, while Konrad (1996) used surface temperature over the Southeast. Walsh et al. (2001), Vavrus et al. (2006), and Wheeler et al. (2011) all use similar definitions based on normalized temperature anomalies for a given space or time threshold. See specifically Vavrus et al. (2006) for a discussion on the factors considered. Wheeler et al. (2011) applied their definition to the ERA40 reanalysis dataset, and found a maximum frequency in CAOs from British Columbia and Alberta southeastward into the Plains of the US. Wheeler et al. also found that the average intensity of these CAOs was maximized in the same region of Canada and into the northern Plains and Midwestern US, with a local minimum in intensity over the Great Lakes region. The common theme of the various definitions used in these past studies is that anomalously cold temperatures occur on synoptic space and time scales. As such, CAOs were generally assumed to be connected to synoptic-scale atmospheric features (e.g., cyclones, anticyclones, fronts).

However, as part of a general desire to attribute extreme cold to some larger-scale atmospheric entity beyond low and high pressure systems, the 2014 Arctic outbreak into central and eastern North America popularized the term “polar vortex” into public vernacular through national and global media. This new catch-all for cold winter temperatures returned in January 2019. The public use of this term is often a misconception, since “polar vortex” is the name given to the radiatively-driven climatological cyclonic circulation that resides in the high latitudes of the winter stratosphere (Palmer 1959). Meanwhile, the tropospheric polar vortex may refer to the baroclinically-driven polar jet stream (PJS) which roams around the middle latitudes and exhibits much greater variability and asymmetry than the stratospheric polar vortex. A comprehensive summary of the distinctions between

the stratospheric polar vortex and tropospheric polar vortex is presented in Waugh et al. (2017), including the role each may play in extreme weather. As discussed in Waugh et al. (2017), the amplitude of waviness and "distortions" in the PJS correspond to anomalous temperatures and high impact events on synoptic time-scales.

Past CAO studies have targeted this waviness in the PJS and the attendent surface pressure features including a focus on the surface anticyclone-cyclone couplet (e.g. Boyle and Bosart 1983) that classically advects cold air southward in these events. Konrad and Colucci (1989) provided the first systematic study of CAOs in North America determining that the most intense CAOs were associated with later timing of downstream cyclogenesis. Subsequently, Konrad (1996) stated that CAO intensity was more strongly connected to the amplitude of the upstream anticyclone than the downstream cyclone. Relationships between surface cyclones and anticyclogenesis, and cold surface temperatures transported equatorward from northwestern North America, have also been demonstrated by Colucci and Davenport (1987), Curry (1987), Colle and Mass (1995), and Walsh et al. (2001).

On the planetary scale, Konrad (1996) found a significant signal in the pattern up to two weeks prior to a CAO, including persistent positive 500 hPa height anomalies over Alaska and negative anomalies over the Great Lakes. This upper air configuration is consistent with the large positive sea level pressure anomalies over Alaska into northwest Canada found by Walsh et al. (2001). Konrad II (1998) expanded on the investigation of antecedent large scale circulations with similar conclusions, and referenced the Pacific North American (PNA; Wallace and Gutzler 1981) pattern as one of possible correlation to CAO intensity and frequency. Meanwhile, Cellitti et al. (2006) found no preference in the PNA prior to or during CAOs, but did find a preference for a negative North Atlantic Oscillation (NAO). All of these teleconnection results have the one consistent message that CAOs are connected to the planetary-scale "waviness" and displacements in the PJS.

This study aims to demonstrate that a displacement of the PJS cannot alone achieve the extreme anomalies that were recorded in January 2019. In an investigation of tropopause

folding in the Arctic, Shapiro et al. (1987) identified structures similar to folds associated with the PJS. The Arctic folds were associated with jet cores positioned lower in altitude than the PJS, as well as a thermal boundary extending to the surface. On the cold side of the boundary, Arctic air resided beneath a depressed tropopause. These observations form Shapiro's "threefold" structure of the tropopause, and the first definition of the Arctic jet stream (AJS). The AJS encircled what Shapiro referred to as a "polar vortex", which at this point may trigger a visceral reaction from the reader and confusion with the public misuse of the term. Instead of a planetary-scale feature, the maps and cross sections in Shapiro et al. (1987) reveal a structure similar to the subsynoptic-scale disturbance that has since been referred to as a tropopause polar vortex (TPV; Cavallo and Hakim 2009; Cavallo and Hakim 2010a).

TPVs are one type of feature of initially called mesoscale tropopause depressions and defined as a sub-synoptic maximum in the potential vortiticity (PV) field with a significant lowering of the tropopause (Browning et al. 2000). Subsequently these features became known as coherent tropopause disturbances (CTD; Pyle et al. 2004), identifiable by a local extremum in the height of the tropopause, with the additional distinguishing factor for a TPV being the residence time in the polar latitudes. TPVs were found by Hakim (2000) to be the physical feature characterized by the average three-dimensional structure associated with vorticity maxima on the 500 hPa surface, in which the coinciding flow at the tropopause resembles a vortex rather than a wave. In accordance with the PV framework established by Hoskins et al. (1985), TPVs are characterized by closed material contours such as isentropes on the dynamic tropopause, defined as a surface of constant PV. As such, fluid is trapped within the vortex, isolated from the surroundings, and conserved following adiabatic and frictionless flow.

Given this conservation property, TPVs can remain coherent vortices in high latitudes, reinforced by diabatic longwave radiative cooling at the tops of low-level clouds common in the Arctic (Curry et al. 1996; Cavallo and Hakim 2012; Cavallo and Hakim 2013). With

local tropopause-level PV tendencies generally dominated by quasi-horizontal advection, TPV lifespans can be on the order of weeks to months in some cases (Hakim and Canavan 2005; Cavallo and Hakim 2009; Cavallo and Hakim 2012), making TPVs the longest-lived subsynoptic-scale features in the atmosphere. The lifespan, conservation properties, and closed vortex structure may have important implications in predictability as well (e.g., Provenzale 1999). Hakim and Canavan (2005) also found that TPVs preferentially moved equatorward over the course of their lives. The ejection of TPVs from the Arctic into the mid-latitudes has been shown to play a key role in cases of significant cyclogenesis (e.g., Bosart et al. 1996). Browning et al. (2000) also noted that errors in the positioning in the location of these tropopause disturbances in the initial conditions of a simulation likely resulted in errors in the prediction of the extratropical transition of a tropical cyclone.

In a composite of TPVs, Cavallo and Hakim (2010a) show that the average structure includes anomalously cold air below a lowered tropopause in the center of the vortex. Given the conservation properties of the vortex, and favored equatorward paths out of the Arctic, it follows that TPVs could contribute to CAOs. Biernat et al. (2021) used a tracking algorithm by Szapiro and Cavallo (2018) to develop a climatology of TPVs that ejected out of the Arctic, and matched it against a climatology of synoptic-scale cold pools. Biernat et al. (2021) found that cold pools associated with TPVs accounted for 32.1% to 35.7% of the CAOs over northern regions of the United States, but only in 4.4% to 12.5% of the events within the southern regions. The study by Papritz et al. (2019) of CAOs in the Fram Strait between Svalbard and Greenland also found a linkage between CAOs and TPVs with 40% of the 40 most intense CAOs and 29% of the top 100 CAOs had a TPV in the vicinity of the Fram Strait.

These recent studies suggest that TPVs are likely one mechanism causing CAOs. Our investigation of the potential role of TPVs in CAOs used observational and modeling approaches to further our understanding of the dynamic causes of extreme CAOs. The motivation for this study includes the significant societal impacts of extreme CAOs and also the

relevance of this dynamic understanding to efforts aimed at advancing our knowledge of how the frequency and intensity of CAOs will vary with the warming occurring within the changing Arctic (e.g., Screen et al. 2015). This study is also part of a larger research theme on the role of TPVs in mid-latitude weather extremes. While high amplitude waviness in the PJS is an important condition in the development of high impact weather events, it is the introduction of the Arctic jet circulating the TPV and Arctic tropopause fold that increases the potential for achieving extremes. As such, this study seeks to establish the role that a TPV played in the January 2019 extreme CAO and then use this knowledge to undertake a climaotological investigation of the linkages between CAOs and TPVs over the continental United States.

The following two sections provides a summary of the PV diagnostic framework used in this study followed by a discussion of the meteorological observations and analysis for the CAO. Section 4 details the methods by which the sensitivity of the CAO to a TPV is investigated utilizing perturbed numerical simulations. Sections 5 and 6 present the results and conclusions from this experiment.

4.2 Potential vorticity diagnostics

Given the conservation properties of TPVs, these features are best quantitatively analyzed using potential temperature and Ertel PV (EPV, Π) defined as:

$$\Pi = \frac{\vec{\omega_a}}{\rho} \cdot \nabla\theta \tag{4.1}$$

where ω_a is the three-dimensional absolute vorticity vector combining relative vorticity and planetary vorticity, ρ is density, and θ is potential temperature. The units of EPV are Potential Vorticity Units (PVU) defined as 1 PVU = 1 x 10^{-6} K kg^{-1} s^{-1} m^2. The dynamic tropopause outside of the tropical latitudes is designated by a surface of constant PV that is generally chosen to be 2 PVU. This framework of "PV thinking" (Hoskins et al. 1985; Morgan and Nielsen-Gammon 1998) is utilized herein for qualitative analysis of the TPV and the large-scale patterns.

Various formulations of PV have been utilized to understand the structure and dynamics of upper-level cyclones beginning with Hoskins et al. (1985), Thorpe (1985) and Thorpe (1986). As illustrated by Thorpe (1986), PV inversion reveals that a cold core upper-cyclone disturbance centered on the tropopause would be associated with a descent of the tropopause, a positive potential temperature perturbation in the stratosphere and a negative potential temperature perturbation within the troposphere. Hoskins et al. (1985) showed that with this upper-level cyclone, the static stability within the troposphere would be decreased under the depressed tropopause as magnitude of the cold thermal perturbation decreased near the surface. Thus, in addition to the previously mentioned role that upper-level cyclones, such as TPVs, play in cyclogenesis, these disturbances will also create an environment more favorable for deep convection (e.g., Nielsen-Gammon and Gold 2008). In this formulation, with the cold thermal perturbation decreasing within the troposphere as one moves toward the surface, an intense cyclonic disturbance on the tropopause would be needed to cause an extreme CAO due strong cooling descending relatively close to the surface. Thorpe (1986) also showed that a "classic cold core disturbance" where the sign of the relative vorticity changes with height requires a thermal perturbation on both the tropopause and at the surface. For example, a cold anticyclone at the surface would be paired with a cyclonic circulation associated with a descending tropopause.

There are several classical qualities about this framework. Moving in the direction of the EPV gradient crossing the dynamic tropopause, horizontal gradients in potential temperature switch direction as does the corresponding thermal wind, $-\frac{\partial \vec{V}}{\partial p} = \frac{1}{f\rho\theta}\hat{k} \times \nabla_p \theta$. The magnitude of the geostrophic wind is therefore at a maximum near the level of the tropopause. A local depression of the tropopause would thus be accompanied by a negative potential temperature perturbation in the troposphere with cyclonic thermal vorticity, a positive potential temperature perturbation in the stratosphere with anticyclonic thermal vorticity, and a maximum in geostrophic vorticity at the tropopause. Given this framework, the definition of a TPV is confirmed as a vortex with maximum amplitude at the tropopause.

The vorticity maximum combines with a local increase in stability at the tropopause due to the temperature perturbations in the troposphere and stratosphere to produce a maximum perturbation in EPV (Eq. 4.1).

With the intimate physical connection of vortex strength to PV and potential temperature, the evolution of a TPV is directly related to changes in EPV. As shown in Pedlosky (1998), the time tendency of EPV following the motion of a fluid can be derived as:

$$\frac{D\Pi}{Dt} = \frac{\vec{\omega}_a}{\rho} \cdot \nabla \frac{D\theta}{Dt} + \frac{\nabla\theta}{\rho} \cdot \left(\nabla \times \frac{\vec{F}}{\rho} \right) \tag{4.2}$$

where $\vec{F}$ is the vector indicating the frictional force on momentum. Equation 4.2 shows that the only ways to change EPV along the path of a fluid is through differential diabatic heating ($\nabla \frac{D\theta}{Dt}$) changing gradients in potential temperature, and through the curl of the frictional force ($\nabla \times \vec{F}$) influencing relative vorticity. Similarly, changes in potential temperature on a PV surface following the motion of a fluid trapped in the closed circulation of a TPV occur only due to friction and diabatic processes.

Cavallo and Hakim (2009, 2010a) demonstrate the effects of friction are small near the tropopause and can be neglected. In addition, since the gradient of potential temperature is two to three orders of magnitude larger in the vertical than in the horizontal (see Fig. 4 in Cavallo and Hakim (2010b)), Eq. 4.2 simplifies to

$$\frac{D\Pi}{Dt} = \frac{\eta}{\rho} \frac{\partial}{\partial z} \dot{\theta} \tag{4.3}$$

where η is the vertical component of absolute vorticity, and the notation $\dot{\theta}$ refers to the material derivative of potential temperature or the diabatic heating rate. This quantity can be partitioned into different physical sources of diabatic change. In numerical modeling, these sources are obtained from the physical parameterization schemes. From Cavallo and Hakim (2009),

$$\dot{\theta} = \dot{\theta}_{rad} + \dot{\theta}_{lh} + \dot{\theta}_{pbl} + \dot{\theta}_{cumulus} + \dot{\theta}_{mix} \tag{4.4}$$

where $\dot{\theta}_{rad}$, $\dot{\theta}_{lh}$, $\dot{\theta}_{pbl}$, $\dot{\theta}_{cumulus}$, $\dot{\theta}_{mix}$, refer to diabatic potential temperature tendencies returned from the parameterization schemes for radiation, latent heating, planetary boundary layer mixing, convection, and dissipation, respectively.

4.3 Methods

This study utilizes the atmospheric component of the Model for Prediction Across Scales (MPAS; Skamarock et al. 2012). The model's dynamical core is built on an unstructured Voronoi mesh with an Arakawa C-grid discretization. Voronoi partitioning of cells allows for smooth transitions to regional refinement at higher resolution, without needing nested grids. Our approach employs a variable mesh with an elliptic refinement region centered on 60^oN / 100^oW and the major axis along the 100^oW meridian. The result is a horizontal resolution of $\backsim$15 km in the Arctic and North America, that transitions to a quasi-uniform 60 km resolution around the rest of the globe (a total of 535,554 cells; Fig. 4.2). We utilized a hybrid terrain-following vertical coordinate system (Klemp 2011) with 55 levels up to a top of 30 km.

MPAS employs a physics suite subset of the Advanced Research Weather Research and Forecasting (WRF) model. This suite includes the Monin Obukhov surface layer scheme (Grell et al. 1994), the Yonsei University (YSU) planetary boundary layer (PBL) scheme (Hong and Pan 1996), YSU gravity wave drag, Thompson double-moment microphysics (Thompson et al. 2004), RRTMG shortwave and longwave radiation (Iacono et al. 2008) called every 30 minutes, and the new Tiedke convection scheme (Tiedtke 1989) modified for WRF (Zhang et al. 2011). All simulations were integrated forward 7 days with a time step of 90 seconds.

Four simulations were initialized at 00z on 25 January 2019 with the final operational analysis from the National Center for Environmental Prediction's Final Global Data Assimilation System (NCEP's FNL-GDAS) (Myrick 2017). One simulation was considered a control run. The strength of the TPV varied over the first 48 hours in the other three

simulations through artificial heating tendencies imposed above and below the tropopause within the TPV "basin". Based upon inspection of the control run, the TPV basin in the modified runs was defined as all adjacent cells with a potential temperature less than 285 K on the 2 PVU surface. Following Eq. 4.3, the TPV was weakened (strengthened) through cooling (heating) the stratosphere and heating (cooling) the troposphere.

Specifically, two simulations were designed to weaken the TPV by imposing a heating rate of 10 K day^{-1} (hereafter called TPVweak10) and 5 K day^{-1} (hereafter TPVweak5) in the troposphere, and a cooling rate of the same magnitude in the stratosphere. The other modified simulation strengthened the TPV (hereafter TPVstrong5) with a cooling rate of 5 K day^{-1} imposed in the troposphere, and a heating rate of the same magnitude imposed in the stratosphere. After 48-h of applying these heating and cooling rates, significant differences in TPV intensities were noted. Thus, at hour-48, the modified simulations are restarted with artificial tendencies removed, and run forward with the same model configuration as in the control simulation. These simulations were conducted for another five days, approximately the time for the TPVs to move through the area of interest. The effectiveness of the tendency modifications was assessed by examining the subsequent intensity of the TPV at hour-48 defined by the minimum potential temperature on the 2 PVU surface in the TPV basin. The center of the TPV at a given time was defined by the location of that minimum potential temperature. TPV tracks were generated simply by using a regional minimum filter applied to the 2 PVU potential temperature field, evaluated at the location from the previous time step, and then identifying the new location of the regional minimum.

Coarser simulations with quasi-uniform resolutions of 60 km, 120 km and 240 km were also utilized to test the modified tendencies and evaluate the sensitivity of the TPV and CAO to the gird resolution. The primary differences with the coarser resolution simulations are a systematic bias toward a weaker TPV, as well as a reduction in the equatorward reach of the TPV track. While we will not explore these differences in detail in this paper, one is cautioned about utilizing such coarse grid models to examine the intensity and equatorward

extent of CAOs that are associated with TPVs moving from the Arctic into the middle latitudes. Our findings and the subsequent results of Biernat et al. (2021) and Papritz et al. (2019) that show TPVs are often related to CAOs implies a more general caution should be considered when drawing inferences about CAOs from coarse grid simulations.

In addition to these simulations, a climatology of CAOs were determined from the North American Regional Reanalysis (NARR; Mesinger et al. 2006) with a 32-km grid spacing for 1979 through January 2019. Daily mean 2-meter temperatures (T2m) were standardized against the climatological seasonal mean and standard deviation (σ) for December through February (DJF). Only grid points south of 50^0N and with a DJF T2m σ greater than 5^oC were considered viable to be a part of a CAO. At these viable grid points, streaks of at least two consecutive days with T2m anomalies less than -2σ were identified, consistent with Walsh et al. (2001). Finally, CAO days were defined as any day with at least 75% of a 500 km by 500 km region composed of these cold streak grid points. This method thus includes both temporal and spatial criteria with sub-synoptic-scale thresholds. Additionally, by using standardized anomalies, CAOs are dependent on the second and higher order moments. For example, high CAO frequency is associated with large negative skewness in DJF temperatures. The centroid of the CAO was defined as the center point of the region with the most cold streak grid points, and the magnitude was determined by the median T2m standardized anomaly within the given region.

4.4 Results

4.4.1 Observations

At 12 UTC on 30 January 2019, an extratropical cyclone was located to the northeast of the Great Lakes (Fig. 4.3). An anticyclone and trailing cold front located over the central US was also present with the front extending relatively far southward reaching the border of Oklahoma and Texas, southern Arkansas and northern Mississippi. Comparison of the extreme cold in Fig. 4.1 and the position of the cold front (Fig. 4.3) suggests that the low

temperatures (i.e., coldest per year) and the extremes (i.e., coldest in ten years) are limited to the northern portions of the cold air mass with the southern portions behind the front relatively unscathed.

The FNL-GDAS analysis at 12 UTC on 30 January is shown in Fig. 4.4. The 500 hPa winds and height field (Fig. 4.4a) reveals a large ridge over the eastern Pacific and western North America with a trough containing both an extended area of enhanced vertical vorticity and a strong cyclonic circulation over the Great Lakes that is consistent with a TPV. A vertical cross-section through the region of strongest vorticity (Fig. 4.4b) reveals a structure characteristic of an tropopause fold with a dramatic descent of the 2 PVU surface from above 300 hPa to near the surface with a well defined cyclonic circulation surrounding the tropopause fold. The dramatic descent of the 2 PVU contour to the surface is also visualized in Fig. 4.4c and d with a clear vortex signal characteristic of an intense TPV. The basic interpretation of Fig. 4.4b, c and d is that the stratospheric air within the TPV has descended to below 900 hPa, just above the earth's surface. From Fig. 4.4b, d, it is evident that the descending core of the TPV slopes to the southwest, to the right of the TPV core aloft. Earlier work has shown that vertical motion near the tropopause result in vertically tilting the tropopause and once this initial vertical tilt is established, the vertical shear associated with the cold air advection in the northwesterly flow acts to further tilt the tropopause in the vertical (Wandishin et al. 2000).

Backward trajectories were initiated at 12z 30 January 2019 utilizing NOAA ARL's HYSPLIT program (Stein et al. 2015) based upon the FNL-GDAS analysis (Fig. 4.5). The initial points for these trajectories were taken from a 1-degree by 1-degree latitude/longitude grid within the tropopause fold from heights of 3500 m above sea level. These trajectories (Fig. 4.5) clearly show that the colder air (i.e., less than 270 K) within the tropopause fold can be traced to north of Canada in an area just west of Ellesmere Island and Greenland. Trajectories for the warmer air mass also suggests Arctic origins. The looping nature of the trajectory is consistent with the appearance of a prolate cycloid as air well away from the

centriod circulates around the cyclone as the TPV moves equatorward. The geographical spread in the trajectories appears quite narrow suggesting that the air parcels remain within the cyclonic circulation as the TPV moves across Canada and into the areas west and south of the Great Lakes. This capturing of the TPV circulation is consistent with our earlier discussion of the PV framework as the closed material surfaces associated with a TPV will result in the air being trapped within the TPV circulation. Comparison of the minimum temperatures (Fig. 4.3) and the trajectories (Fig. 4.5) show that the coldest temperatures are located in the wake of the TPV and evolving tropopause fold. The trajectories (Fig. 4.5) also suggest a rapid movement of the cold lower tropospheric air mass into the middle latitudes as, for example, the trajectories to the west of the vortex center move from the northern Canadian Arctic coast to the U.S. border in the less than 24 h.

Radiosonde measurements support the concept that stratospheric air has descended substantially as shown from soundings taken at Chanhassen, MN and from Green Bay, WI at 00 UTC on 30 January 2019 (Fig. 4.6a and b respectively). These profiles taken near and to the west of the vortex center in Fig. 4.4 reveal stable, dry air extending to below 600 hPa, and particularly the Green Bay sounding shows the signature of a tropopause fold near 800 hPa. Both of these soundings taken in the evening hours have a mixed boundary layer extending to near 850 hPa. The soundings taken later and to the west from Lincoln, NE at 12 UTC on 30 January 2019 and Davenport, IA at 00 ITC on 31 January 2019 show the tropopause extending nearly to below 900 hPa (Fig. 4.6c and d respectively). The lowering of the tropopause nearly to the surface is consistent with vertical cross-section and the 2 PVU surface from the FNL-GDAS analysis shown earlier in Fig. 4.4b,d. The winds in these soundings also reveal a general increase with height with little change in direction in this layer. This lack of any significant directional vertical shear implies that little geostrophic cold air advection is occurring near the earth's surface at this time.

The structure of the CAO and TPV is quite different for measurements taken near and "downstream" of the Great Lakes. For example, the soundings at Detroit, MI and Buffalo,

NY (Fig. 4.7c, d) have a much deeper layer of reduced stability relative to the soundings taken to the west at Chanhassen and Green Bay (Fig. 4.7a, b). This layer of reduced stability extends to 700 hPa at Detroit and 660 hPa at Buffalo. At both of these sites, significant moistening and warming (i.e., $10 - 20^{o}C$) has taken place within this layer. While these changes could be due to differential advection, an explanation that will be explored later when the impact of the open waters of the Great Lakes is explored in the subsequent simulations. This modification is also consistent with the lake effect snows discussed in the introduction.

4.4.2 Control simulation

The control run is examined first to establish the evolution of the atmosphere over the week leading up to and including the CAO. In the first 48 hours, through 00z 27 January, a closed area of low potential temperatures colder than 270 K is evident on the dynamic tropopause over the northern Canadian archipelago, identifiable as a TPV (Fig. 4.8). The location and initial meandering path of the TPV agrees with the backward trajectories in Fig 4.5 supporting the observational analysis that suggests a linkage between the CAO and the TPV. Another well-defined TPV is noted to the south-southeast, entering Ontario on the 26th. This first TPV skirts just north of the Great Lakes on the 27th and is associated with the initial surge of cold air entering Wisconsin, Michigan, and subsequently into the Northeast through the 28th (Fig. 4.9). The lead TPV plays an important secondary role in the CAO. While the NAO during this time was positive, as for example in the persistent ridge of warm tropopause temperatures over the North Atlantic (Fig. 4.8), the lead TPV temporarily pushes this ridge east along with a transient surface low near $50^{o}N$ / $50^{o}W$ (not shown) that mimics the effect of a negative NAO, helping upstream cold air to pour southeastward. From the 29th to the 30th, the lead TPV slides eastward from Quebec out to the northern Atlantic.

A large ridge characterized by tropopause potential temperatures over 330 K was a feature over the eastern Pacific and western North America through the control simulation (Fig. 4.8) consistent with the 500 hPa FNL-GDAS analysis shown earlier (Fig. 4.4). A key short wave trough can be seen cresting the ridge over the Yukon territory at 00z on the 27th (Fig. 4.8). As the short wave moved equatorward over Alberta, the destructive interference is removed from the ridge which re-amplifies toward Alaska and the Yukon on the 28th. As this ridge amplifies and the short wave trough extends southward into the mid-western US on the 29th, the TPV moves southward out of Canada. This TPV enters into the Midwest on the 29th subsequently crossing the Great Lakes on the 30th and moving into the northeast US on the 31st. At the surface, an Arctic air mass characterized by temperatures below -30^oC is dragged southward at the leading edge of the TPV from the 27th through the 29th (Fig. 4.9) leaving a swath of temperatures below -30^oC in its wake.

The evolution of vertical structures was analyzed by averaging variables in the horizontal within a 400 km radius of the TPV center and plotting the averages in a time-height section (Fig. 4.10 a). The radius was selected to focus on the core of the TPV as shown in Fig. 4.4. Increased stability above the cold surface layer contributes to increased PV below 850 hPa through 28 January, which can be seen in the time-height section of area-averaged potential temperature and PV in Fig. 4.10a. Over time, the cold air deepens as seen by the evolution of the 240, 245, and 250 K isentropes, pushing the high-PV air upward to between 700 and 800 hPa through the 29th. At its most pronounced stage, the TPV and cold pool are co-located over central Manitoba on 29 January.

Insight into the physical causes of the evolution of the TPV in the observed soundings (Fig. 4.6 and 4.7) and the PV and potential temperature fields in the control simulation (Fig. 4.10 a) can be explored using the time rate of change of PV (3) within the context of the diabatic tendency fields from the parameterization schemes utilized in MPAS (4). Within the middle and upper troposphere, the contributions are generally small with positive contributions from the longwave radiation (Fig. 4.10b) and negative contributions

from shortwave radiation (Fig. 4.10c). The decrease in PV is associated with increasing shortwave radiation as the TPV moves equatorward (Fig. 4.11a). Positive contributions to TPV intensity from diabatic longwave cooling has been previously noted (e.g., Cavallo and Hakim 2012; Cavallo and Hakim 2013). During the southward movement of the TPV, the area-averaged dynamic tropopause lowers over time, by about 10 K and 50 hPa, assisted by longwave radiative cooling near the tropopause.

Below 700 hPa, the impacts of the diabatic terms are much larger (Fig. 4.10) as the TPV moves southward across Canada and into the US (see Fig. 4.8). The diabatic impact of the boundary layer parameterization (Fig. 4.10e) is to create a shallow layer of PV enhancement near the surface beginning on 25 and 26 January, while the TPV is still within the Arctic (Fig. 4.8). As the TPV moves southward, the impact of the boundary layer parameterization deepens and includes times when the PV tendency changes sign. While a near constant temperature might be expected in the Arctic, the southward moving TPV is encountering a surface affected by the diurnal cycle in shortwave radiation and the presence of open water over the Great Lakes (Fig. 4.8). The effects of the Great Lakes on the TPV are evident due to the destruction of PV through the cumulus convection scheme (Fig. 4.10d). The reduction in stability combined with the moisture source from the Lakes promotes shallow cumulus convection (e.g. Agee and Gilbert 1989). The low-level lapse rates also rapidly steepen as seen by the increased spacing between isentropes below 700 hPa in Fig. 4.10. As discussed earlier, the soundings at Detroit and Buffalo (4.7a, b) near the Great Lakes revealed a steepening of the lapse rate and moistening of the lower atmosphere. This environment contributing to the production of cumulus convection result in the long wave radiation cooling at cloud tops and warming underneath decreasing PV (e.g. Fig. 3 in Cavallo 2009) from near the surface to below 850 hPa (Fig. 4.10). In contrast, mixing has a generally smaller impact (Fig. 4.10f). The end result of the passage of the TPV over the Great Lakes is a clear destruction of PV below approximately 600 hpa (Fig. 4.10) with deepest impacts due to the cumulus convection. Consistent with this destruction of PV,

the tropopause height lifts upward on 31 January following the passage of the TPV over the Great Lakes (Fig. 4.10). The interaction between the TPV and the Great Lakes are consistent with the multi-day lake-effect snowfall event with, for example, according to NOAA reports snowfall totals of up to 37.6 inches (95.5 cm) south of Watertown N.Y and up to 21 inches (53.3 cm) at Buffalo.

4.4.3 Modified simulations

All four simulations have similar tracks and timing of the TPV as it ejects out of the Arctic (Fig. 4.11) with TPVweak10 (Fig. 4.11b) and TPVweak5 (Fig. 4.11c) especially similar to the control track (Fig. 4.11a). These three simulations all have a track into southern Canada and subsequently into the midwestern US, but east of the observed event. In contrast, the TPV in TPVstrong5 begins diverging further east of the control during the first four days of the simulation (Fig. 4.11d), but after day-4 abruptly moves to the southwest and then follows a track similar to the observed event into the CONUS. The TPV rolls through the base of the long wave trough like the other simulations, but up to 400 km further south. The center passes over Washington D.C. around day-6, compared to Buffalo, NY in the control.

Despite these differences, ultimately any perturbations in the intensity, size, and structure of the TPV induced by the artificial heating tendencies did not impact the synoptic-scale pattern of the track of the TPV. All simulations, including low-resolution tests, transported the TPV southward into the trough over Canada and the northern CONUS. This result is a testament to the intrinsic predictability of the large-scale flow, in which the sensitivity to this particular mesoscale perturbation introduced in the Arctic was small. These results do, however, show that the stronger TPVs (e.g. control and TPVstrong5) take paths further south.

In order to compare the evolution of the vertical structure around the TPV in the modified simulations to the control, the area-averaged time-height analysis applied to the control

simulation is again utilized. Systematic differences between the three modified simulations and the control are apparent in the dynamic tropopause over the first three days (Fig. 4.12). In accordance with the methods of modifying the TPV strength, TPVweak10 and TPVweak5 feature a reduction in PV near 500 hPa with a tropopause that is shifted upward from the control (Fig. 4.12a,b). Likewise, TPVstrong5 features an increase in PV near 600 hPa, with a tropopause that is shifted downward from the control (Fig. 4.12c).

There are notable negative PV differences from 18z on the 28th to 0z on the 29th in both of the TPVweak simulations (Fig. 4.12a,b). These differences correspond with the negative PV tendencies due to the diabatic boundary layer tendency in the control (Fig. 4.10b), and are likely a result of stronger radiational surface warming in the modified simulations with less cloud cover. In all three of the modified simulations, there is generally higher PV in the boundary layer during 29 January, and higher PV in the middle troposphere on 30 January (Fig. 4.12). Particularly on 30 January, this coincides with the passage of the TPV over the Great Lakes. The differences in TPVweak10 and TPVweak5 may be attributed to the weaker TPV introducing a smaller temperature difference between the water and air, and thus developing less cumulus convection than in the control. The difference in TPVstrong5 is expected both due to the deviation in the TPV track to the south of the Great Lakes (Fig. 4.11d) and to antecedent positive PV perturbations from the prior intensification. The linkages between TPV strength and the severity of lake effect snows is an area for future research.

4.4.4 Sensitivity of extreme cold to the TPV

The depth of the TPV, given by the minimum potential temperature in the TPV basin, diverges quickly among the four simulations in the first 24 hours (Fig. 4.13a). The control and TPVstrong5 simulations deepen the TPV by 20 to 30 K, respectively, while TPVweak5 and TPVweak10 weaken the TPV by 10 to 20 K, respectively as expected given the experimental design. The intensities generally remain steady over the next 24 hours. On 27

January, the control and TPVstrong5 begin to gradually weaken. By the 29th, the control TPV has weakened back to the intensity at the beginning of the simulation, while both TPVweak5 and TPVweak10 show little subsequent change in intensity. By the 30th, the control begins converging toward TPVweak5, and TPVstrong5 undergoes rapid weakening to join this cluster as well. On the 31st, the control, TPVweak5, and TPVstrong5 are tightly clustered while TPVweak10 is approximately 10 K weaker than the rest. This evolution likely shows the impact of the TPV moving into this specific middle latitude flow and the relatively large diabatic influences on the system that occur with cyclogenesis that takes place on 30 and 31 January.

Following the past studies discussed in the introduction that attribute CAO magnitude to the strength of the surface anticyclone, there is a desire to test their null hypothesis in the case of the January 2019 CAO. The strength of surface pressure centers were assessed within a 1600 km radius of the TPV center; a horizontal length scale that exceeds one synoptic wavelength while much less than two wavelengths to avoid capturing unrelated features. The surface high within this radius of the TPV begins at 1023 hPa over the Arctic, and gradually strengthens over the next 24 hours (Fig. 4.13b). From 26 to 27 January, all simulations bring the high pressure up to around 1040 hPa. TPVstrong5 intensifies the surface high by 12 hPa over a 24-hour period up to 1044 hPa at 00z 28 January. The other simulations also exhibit strengthening rates of 9 to 11 hPa in 24 hours, all exceeding the threshold for rapid anticyclogenesis used by Colucci and Davenport (1987).

While the spread is still small, by this point late on the 27th to 28th, a systematic separation of the simulations develops (i.e. a correspondence between the modification of the TPV and the strength of the high). By 00z on 30 January, when the surface anticyclone is crossing into the northern Plains from Canada, the maximum SLP in TPVstrong5 is 1039 hPa, and in TPVweak5 is 1034 hPa (Fig. 4.13b). The greatest separation in the simulations occurs on 30 January in which an inverse relationship exists between the minimum 2 PVU potential temperature in the TPV and the maximum SLP of the surface high. At 12z on

30 January, the surface high pressure area was observed to stretch from Manitoba into the Midwest, with a maximum SLP of 1033 hPa. The simulations range from 1031 hPa in TPVweak10 to 1041 hPa in TPVstrong5. Thus, the strength of the anticylones appear to be dependent on the intensity of the TPV.

The differences in surface temperatures between the modified simulations and the control are consistent with the surface higher pressure and colder air at the surface being associated the stronger TPV. The surface temperatures were evaluated using the minimum of a 24-hour running-mean convolution of 2-m temperatures over the 7-day simulation period (Fig. 4.14). The timing of the coldest 24-hour period by location (not shown) is consistent among the four simulations, particularly within the swath of Arctic air carved by the TPV. There is remarkable linearity in the relationship between the modification of the initial strength of the TPV over the Arctic and the resulting 2-m temperatures in the eastern half of the CONUS (Fig. 4.14). Note that 2-m temperatures over northern Canada and the Arctic were generally not affected by the modifications, with systematic differences along the track of the TPV only beginning to appear in southern Canada.

The magnitude of the temperature differences over the CONUS are substantial. Between TPVweak10 (Fig. 4.14a) and TPVstrong5 (Fig. 4.14c), the mid-Mississippi River Valley in particular ranges more than 11^oC (20^oF). Rather than being maximized directly along the track of the TPV, the location of these temperature differences are displaced to the right of the track, and mostly to the south of the record cold shown in Fig. 4.1. In TPVstrong5, this placement could to an extent be explained by the southward deviation in the track itself (Fig. 4.11), however the TPVweak5 and TPVweak10 runs have the same southward-shifted temperature differences but with TPV tracks similar to the control. These results suggest an asymmetric spatial relationship between the TPV intensity and 2-m temperatures and a strong impact of TPV intensity on surface temperature associated with the extreme CAO. These results together with the studies by Biernat et al. (2021) and Papritz et al. (2019) show the importance of considering the intensity and location of TPVs

in CAOs. The tilt of the TPV with height, as shown earlier, also impacts this relationship between the location of the TPV center and the location of the coldest air.

The strength of surface low pressure was also evaluated within the same radius as the high (Fig. 4.13b). The minimum SLP was remarkably consistent among the TPVweak10, TPVweak5, and control simulations. Most notably, these three simulations all intensify a low over Quebec from around 998 mb to 974 mb in the 24 hours between 00z 30 and 31 January, qualifying it as a ”bomb” cyclone (Sanders and Gyakum 1980). Only TPVstrong5 deviated from this tight clustering, with a substantially weaker low on 30 January that is much closer to observations. These differences raise the issue of whether there is a strong dependence of the intensity of cyclogenesis on the magnitude and location of TPVs. This issue is an area for future investigations and suggests the possible importance of an accurate representation of TPVs in middle latitude cyclogenesis.

4.5 Climatological relationship between TPVs and CAOs

Applying the approach outlined in the section 3 to the period from 1979 through 2019, 256 CAO days were identified, with the majority found along the full meridional extent of the Plains (Fig. 4.15). Lower spatial density is found east of the Mississippi River. A second cluster is found in the Northeast US and southern Quebec (limited to the north by the 50^0 N boundary criterion). The combination of smaller temperature variance and smaller skewness are likely due to modification of cold air masses by the large bodies of water resulting in a dearth of CAO events centered within the Great Lakes region. The position of the CAO for the 30 January event studied in this case (Fig. 4.15) suggests that many CAOs extend far further south than this extreme event sometimes with a similar magnitude. The relationship between CAOs at the surface and dynamics aloft was explored by compositing the potential temperature, winds, and tropopause potential temperature anomaly on a 2 PVU surface (Fig. 4.16). In this composite, the CAO lies poleward of a jet streak on the 2 PVU surface (Fig. 4.16) and the CAO centroid lies to the southwest of a strong cold anomaly

on the tropopause. This finding is consistent with our simulations and observations that revealed, on average, the coldest air is just to the southwest of the TPV.

To explore if the relationship between CAOs and cold anomalies on the tropopause are linked to TPVs, the locations and tracks of all TPVs during DJF are obtained using the tracking algorithm from Szapiro and Cavallo (2018) applied to ERA-Interim (Dee et al. 2011a) reanalysis for the period from 1979 through 2018. Two definitions were analyzed for tracking these vortices: one requiring genesis north of 60^o N (60Ngen), and the other requiring 60% of the feature's lifetime be spent north of 65^o N (60N65). It is important for the reader to note that the later criteria is consistent with the widely utilized TPV definition put forth by (Cavallo and Hakim 2005), while our first TPV definition is not. A relaxed criteria was also implemented by Biernat et al. (2021). The relationship between these two categories of Arctic vortices and CAOs utilizing the definition discussed is shown in Fig. 4.17. Specifically, the distance between the CAO centroid and a TPV was calculated for all CAOs and then the percentage of CAOs with a nearby TPV was determined as a function of distance between the two features (Fig. 4.17). For TPVs generated north of 60^oN latitude, 85% of the CAOs had a vortex located with 1000 km with over 95% of the CAOs having a TPV within 2000 km.

Since the close proximity of these features could be due to random chance rather than a dynamical relationship, we also took the location of the CAO and then calculated the distance to a TPV on days selected at random (1000 times) from the December through February 1979-2019 period. The results of this random selection process for the mean and 95% range for this sample contrast sharply with the CAO-TPV proximity as TPVs on random days are only near that location a few percent of the time (Fig. 4.17). This result supports the findings of our case study and also the recent work of Biernat et al. (2021) and Papritz et al. (2019) that have shown connections between TPVs and CAOs. While the results of Biernat et al. (2021) argue that a 400-km threshold should be utilized when

searching for a linkage between TPVs, cold pools associated with TPVs and CAOs, Papritz et al. (2019) noted that the cyclonic circulation of TPVs can aid in the creation of CAOs through modifying the longer range transport of Arctic air.

The relationship is less clear for those TPVs that have spent over 60% of their lifetime poleward of 65^o N (Fig. 4.17), as for example, the average distance is closer than 1000 km in these cases in less than 25% of the time. This weaker relationship for TPVs that have spent greater time in the Arctic related to those TPVs simply generated north of 60^o N could imply differences in the large-scale flow such as a more positive annular mode that traps the 65^o N TPVs in the Arctic with fewer escaping to the mid-latitudes. The tracks for TPVs passing within 1000 km of a CAO are plotted in standardized form against the full winter climatology (Fig. 4.18). Over North America, there is a clear tendency for TPVs to move from the northern Canadian Arctic southward into the Great Lakes/upper-midwest and then northeastward over Labrador. This result is quite similar to the event investigated in this study. Given our previous finding that TPVs that spent over 60% of the time poleward of 65^o N and this TPV track density, TPVs associated with CAOs are likely to form in the Arctic and then be ejected relatively rapidly into lower latitudes. Thus, relaxing the requirement that the vortices must remain the Arctic for a majority of their lifetime to be called a TPV provides a method to diagnose and include those vortices that originate in the Arctic, are advected more rapidly equatorward and are more likely to include an extreme CAO in midlatitudes. Figure 4.18 also shows that the TPVs associated with CAOs over the CONUS are less likely to spend any extracurricular time between Greenland and Siberia.

A comparison of the minimum anomaly, minimum latitude and lifetime for TPVs located 1000 km or less of the centroid of a CAO and all TPVs shows that TPVs are substantially more intense, are located significantly equatorward, and have significantly longer lifetimes than typical TPVs (Fig. 4.19). Statistical significance is established using the two-sided Kolmogorov-Smirnov (K-S) test to determine whether the distribution of TPVs associated with CAOs are statistically different from the full sample of TPVs (Massey 1951).

In terms of tropopause potential temperature anomaly in the vortex core, anomalies for TPVs located 1000 km or less of CAOs exhibit a peak in the distribution around -40 K with anomalies as low as -76 K with respect to the long-term climatology (Fig. 4.19a). TPVs associated with CAOs tend to have a strong maximum in equatorward movement with a well defined peak in their minimum latitude near 45°N latitude (Fig. 4.19b). Furthermore, lifetimes are significantly longer for TPVs associated with CAOs, with higher probabilities of TPVs with lifetimes of over one week with probabilities of some exceeding one month (Fig. 4.19c). These results again suggest a linkage between CAOs and strong, long-lived TPVs that move equatorward from the Arctic into the midlatitudes.

4.6 Discussion and Conclusions

This study investigated an extreme CAO that began in late January 2019 and was responsible for breaking numerous climatological records for the lowest minimum and maximum temperatures across the Great Lakes, Midwest, and Northeast portions of the US. The wind chills and extreme cold were associated with significant detrimental societal impacts including 21 fatalities, closures of schools and businesses, and transportation disruptions. Our observational and modeling investigations revealed that this extreme CAO was associated with an intense TPV.

A schematic of the TPV and CAO relationship is shown in Fig. 4.20. Within the Arctic, the TPV is associated with a lowering of the tropopause and a cyclonic circulation (Fig. 4.20a). Previous studies focused on the vertical structure of TPVs have revealed that a dome of anomalous cold temperatures occurs within the troposphere below the lowering of the tropopause (Cavallo 2009; Cavallo and Hakim 2010b; Papritz et al. 2019). The vertical gradient in long wave radiative heating often associated with TPVs in the Arctic will cause the TPV to strengthen with a further lowering of the tropopause and an enhancement of this thermal structure. In the event studied, the tropopause descended nearly to the earth's surface.

Our findings suggest that the dome of the anomalous cold temperatures remained associated with the TPV as these feature were ejected out of the Arctic. This behavior is expected since, as described in the introduction, the potential vorticity structure of the TPV means that the air remains within the system for adiabatic and frictionless flow. The evidence for the association between this intense TPV and the cold dome as the TPV entered the continental U.S. includes: i) the wind and thermal structure in the vertical cross-section and the depiction of the 2PVU surfaces (Fig. 4.4); ii) the close proximity of the ensemble of lower tropospheric backward trajectories (Fig. 4.5); iii) the relatively slow initial modification of the TPV structure within the simulation (Fig. 4.10); iv) soundings revealing extremely cold surface temperature near the lowest descent of the tropopause (Fig. 4.6).

A schematic of the subsequent evolution of the intense TPV moving into middle latitudes is shown in Fig. 4.20b. Within middle latitudes cold air was found at the surface and within the lower troposphere beneath the tropopause depression associated with the intense TPV. A tilt of the TPV with height is also evident with the extreme temperatures found in the quadrant where the Arctic tropopause descended nearly to the surface (Fig. 4.20b). The vertical tilt of the TPV is likely connected to the vertical shear associated with the cold air advection from the northwest flow (Wandishin et al. 2000). Recent studies investigating jet superposition events found that vertical circulations associated with the polar jet had a strong ability to vertically restructure the tropopause (Winters and Martin 2017; Winters et al. 2020). The combination of the vertical circulation driven by the polar jet and the vertical shear could be the driving the tropopause vertical extent and tilting. A subsequent impact of middle latitude processes is that as the TPV moved through the region PV was destroyed due to long wave radiation, boundary layer processes and cumulus convection (Fig. 4.10). This modification was especially large when the TPV moved over the ice-free Great Lakes creating lake effect snows.

The linkage between CAOs and TPVs was also found in our climatological investigation that showed TPVs often (85% of the time) exist within 1000 km of a CAO and that

these TPVs tend to be higher amplitude, longer-lived and move further equatorward than the climatological distribution of all TPVs. Our finding is consistent with recent studies of CAOs by Biernat et al. (2021) and by Papritz et al. (2019). For example, Papritz et al. (2019) found that 40% +/- 5% of the 40 most intense CAO events over the Fram Strait were directly associated with a TPV. Biernat et al. (2021) concluded that cold pools associated with TPVs accounted for a significant minority (32.1% to 35.7%) of the CAOs over northern regions of the United States, but far less (4.4% to 12.5%) of the events within the southern regions. Biernat et al. (2021) used a threshold distance of 400 km to define a CAO that was directly linked to the cold pool of a TPV, while Papritz et al. (2019) noted that TPVs may also indirectly contribute to a CAO through enhancing long range transport of Arctic air. Our studies show that 85% of CAOs had a TPV within 1000 km allowing the possibility of direct and/or indirect impacts of TPVs to be present. These results show that intense TPVs moving out of the Arctic are one cause of CAOs in middle latitudes, especially at more northern locations. In contrast, previous studies of CAOs over North America (Colucci and Davenport 1987; Curry 1987; Colle and Mass 1995; Walsh et al. 2001) often stressed the transport of surface cold air equatorward by surface cyclones and anticyclones.

Our simulations of this event with the atmospheric component of MPAS allowed further insight into TPVs and their relationship to CAOs. Comparison of the control simulations against simulations in which the initial strength of TPV was modified revealed a strong relationship between TPV strength in the Arctic and the subsequent magnitude of the cold surface air over the CONUS. Weaker (stronger) TPVs in the Arctic meant warmer (colder) temperatures to the right of TPV track over CONUS. Changing the initial intensity of the TPV in the Arctic had more modest impact on the TPV track even in a 7-day forecast, although stronger TPVs did have a more southerly track over the CONUS. In terms of predictability for this high impact events, our control and modified simulation utilizing MPAS all predicted a movement of the TPV and associated CAO into the northern CONUS.

The magnitude of the CAO and its southern extent were, however, found to be closely linked to the intensity of the TPV.

The widely utilized definition of Cavallo and Hakim (2005) required that vortices spend greater than 60% of its lifetime within the Arctic to be considered a TPV. Our study and the results of Biernat et al. (2021) suggests a broadening of this lifetime criteria is needed. The importance of CAOs that are linked to TPVs that are ejected relatively rapidly out of the Arctic is an intriguing result given that Papritz et al. (2019) found that TPVS with CAO that move over the Fram Strait tend to have longer residence times in the inner Arctic. This difference supports the suggestion of Papritz et al. (2019) that the linkage between TPVs and CAOs needs to be investigated across various regions.

From our climatological investigation, the path for TPVs associated with CAOs over North America show a movement of TPVs out of the northern edge of the Canadian Arctic (western Canadian Archipelago) south-south-eastward into the Midwest and Great Lakes region of the US and then toward the northeast toward Labrador. This movement is consistent with the results of Biernat et al. (2021). Our composites of CAOs in the observations suggest a dynamical linkage in that the CAO centroid lies to the southwest of a minimum in tropopause temperatures and poleward of the entrance region of a jet streak. This relationship is expected given the region to the southwest of the TPV cyclonic centroid will be associated with the advection of cold northerly flow. Our case study, however, suggests that the location of the surface CAO relative to the TPV core on the tropopause also results from the vertical tilt of the TPV.

As noted in Papritz et al. (2019), the atmospheric moisture will increase as the Arctic warms so that TPVs may weaken as the impacts of latent heat increase relative to the role of longwave radiation. Given the association between TPVs and CAOs in our study and the increase in the ice-free areas in a warming Arctic, we concur with the hypothesis of Papritz et al. (2019) that the potential weakening of TPVs with climate change could also reduce the intensity and frequency of CAOs, especially for the most extreme events. Screen et al.

(2015) showed that in a changing climate, Arctic sea ice loss reduces the risk of extreme cold in North America. In addition, the observations and MPAS simulations in our study revealed that the intensity of the TPV in the lower levels was reduced by diabatic processes as the system moved into middle latitudes with a particularly rapid weakening when the TPV moved over the ice-free Great Lakes. A delay in the freezing of the Lakes in a warmer climate is likely to decrease the intensity of CAOs in this region and increase lake effect snows when TPVs move over ice-free warmer water.

In the event investigated in this study, the TPV did pass over the sea ice region between Greenland and the Yukon. Since TPVs that are associated with CAOs spend more time in the western hemisphere side of the Arctic (Fig. 4.18), the origin and location along the equatorward track will matter. Given that our study showed a common track for TPVs moving out of the Arctic into North America, another implication of this study is whether an increase in the waviness of the PJS will occur with a warming Arctic and, if so, the impact of such changes on the frequency of extreme CAOs due to intense TPVs being ejected out of the Arctic. As noted in Blackport and Screen (2020), the relationship between a warming Arctic and waviness of the PJS is currently being debated. The final implication of our study related to a changing climate is the dependence of the intensity and equatorward movement of the TPV and associated CAO on the horizontal grid of the model. This dependence adds a significant caution on the utilization of coarse grid model to draw inferences on how a warming Arctic impacts the extreme CAO events in middle latitudes.

The proceeding sections include work from Lillo et al. (2019): Dynamics behind a record-breaking trough over Mexico and internal atmospheric variability during El Niño.

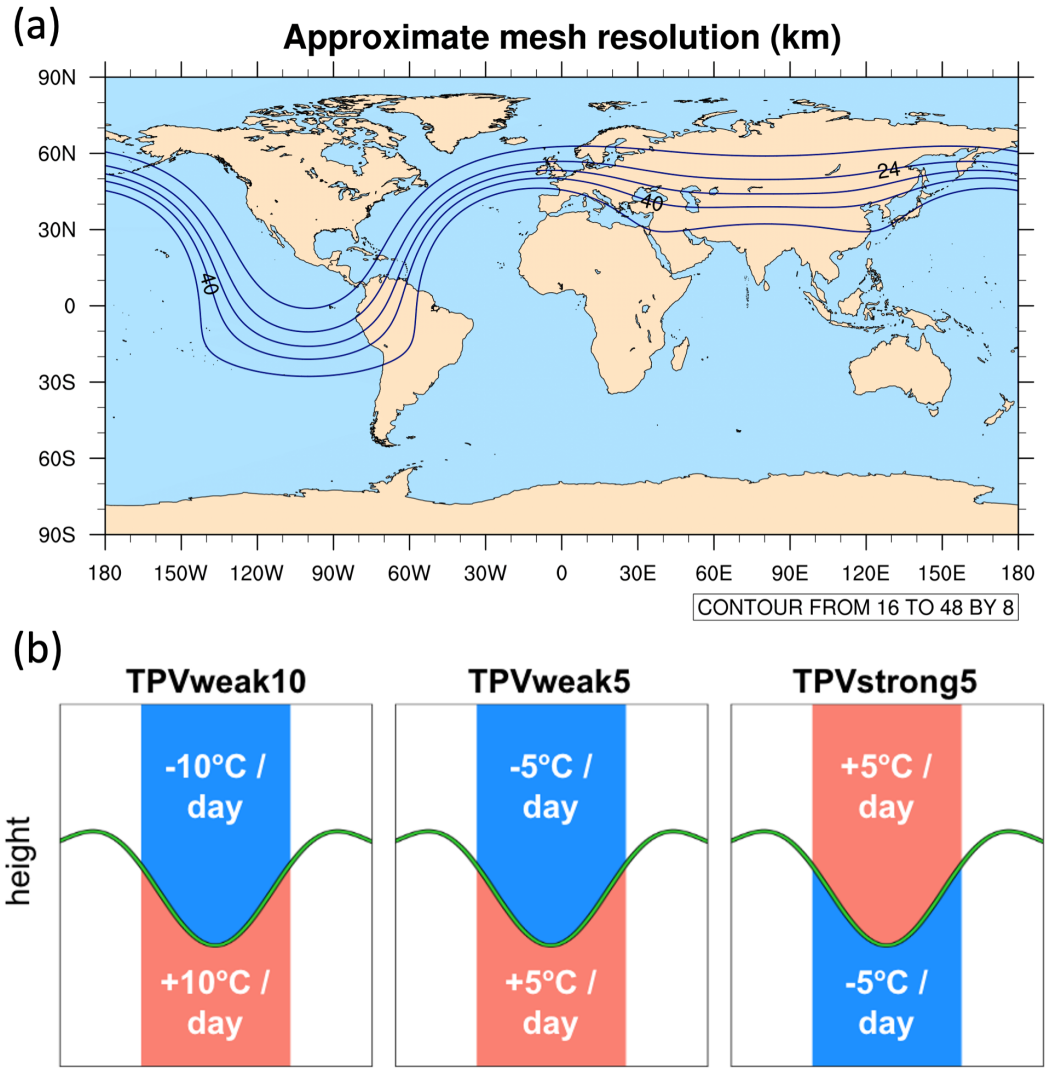

Figure 4.2: (a) The approximate horizontal resolution (km) of the mesh used in the MPAS simulations. (b) Schematic illustrating the method of perturbing the TPV through artificial heating tendencies during the first 48 hours of the simulation.

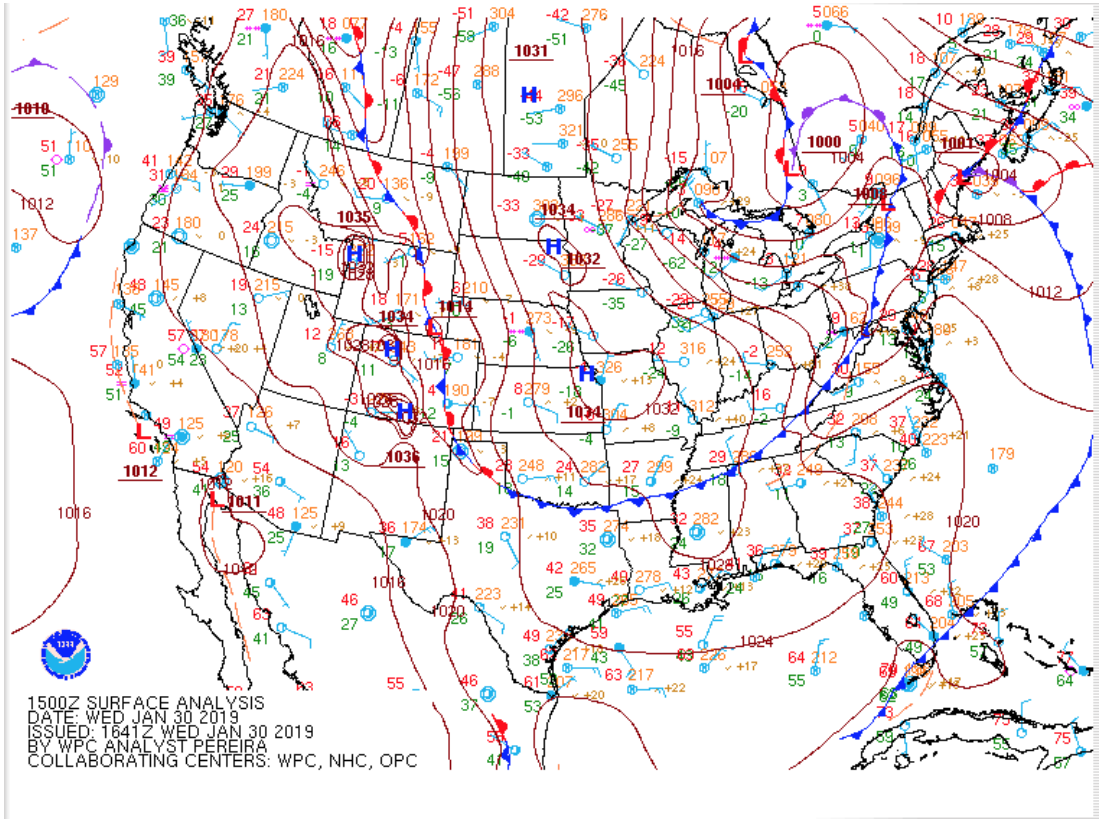

Figure 4.3: The NOAA WPC operational surface analysis for 12 UTC on 30 January 2019.

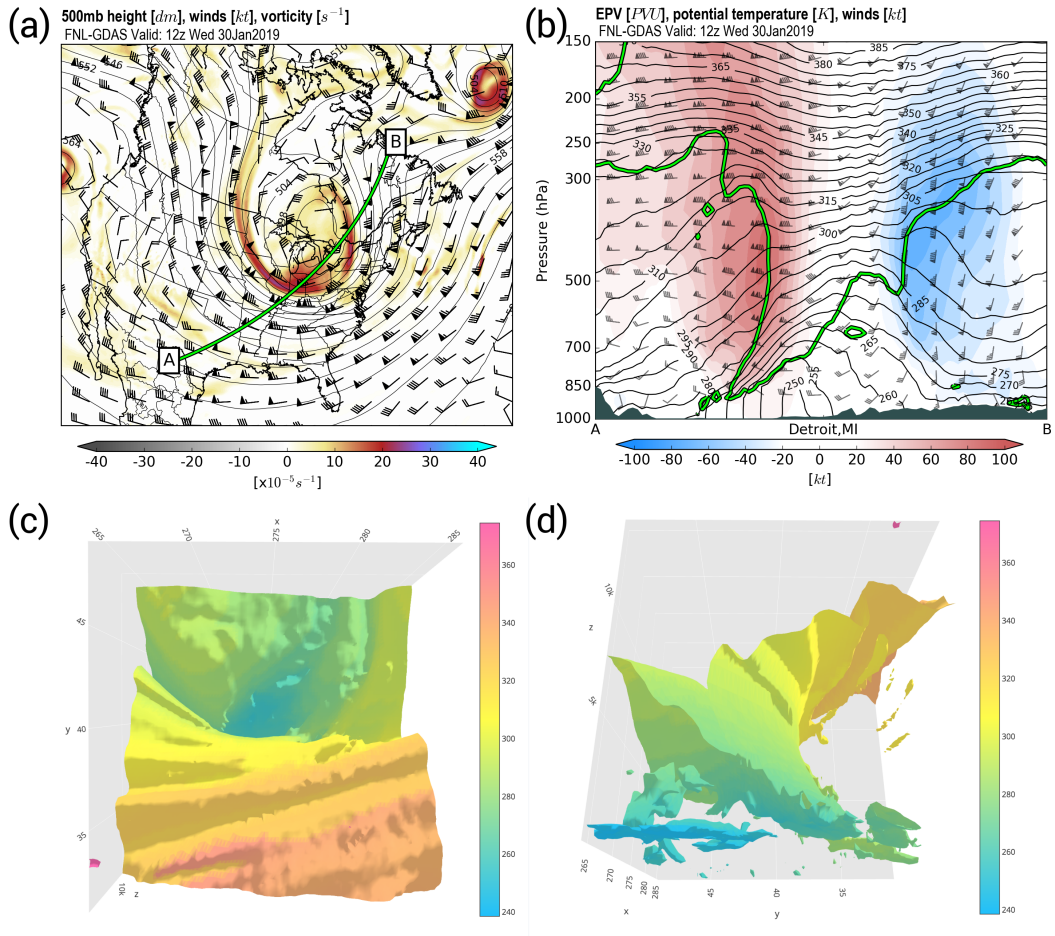

Figure 4.4: FNL-GDAS analysis for 12z 30 January 2019. (a) 500 mb height (dm) contoured every 6 dm, wind barbs (full barb = 10 kt, flag = 50 kt), and relative vertical vorticity (s^{-1}) in color fill. (b) Cross section along the green line plotted in (a) from southwest to northeast centered on Detroit, MI. Potential temperature is contoured every 5 K, the 2 PVU EPV contour is drawn in green, wind barbs are plotted with the same convention as (a), and the wind component normal to the cross section is given by the color fill (positive = out of the page). (c) and (d) show the 2 PVU isosurface shaded by potential temperature (K) in a 3-dimensional plot centered on the 500 mb vorticity maximum. The axes are x: longitude, y: latitude, and z: height [m]. The perspectives are looking directly down (c), and looking up to the east (d).

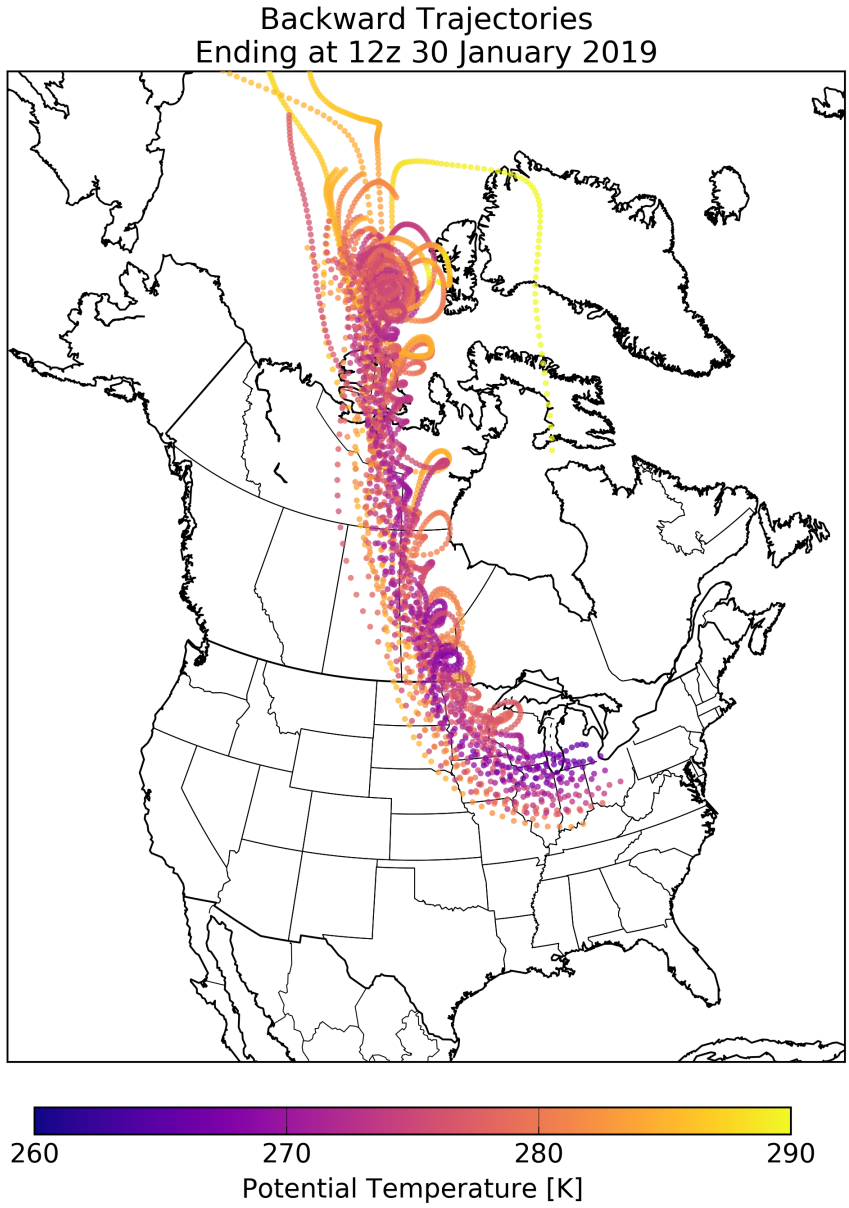

Figure 4.5: Backward trajectories initiated at 12z 30 January 2019 from a 1-degree by 1-degree latitude/longitude grid 3500m above sea level within the tropopause fold shown in Fig. 4.4. Trajectories are run backward for 132 hours using NOAA ARL's HYSPLIT program (Stein et al. 2015) and FNL-GDAS analysis. Each point is at 1-hour intervals along the trajectories and their colors refer to the potential temperature of the parcel.

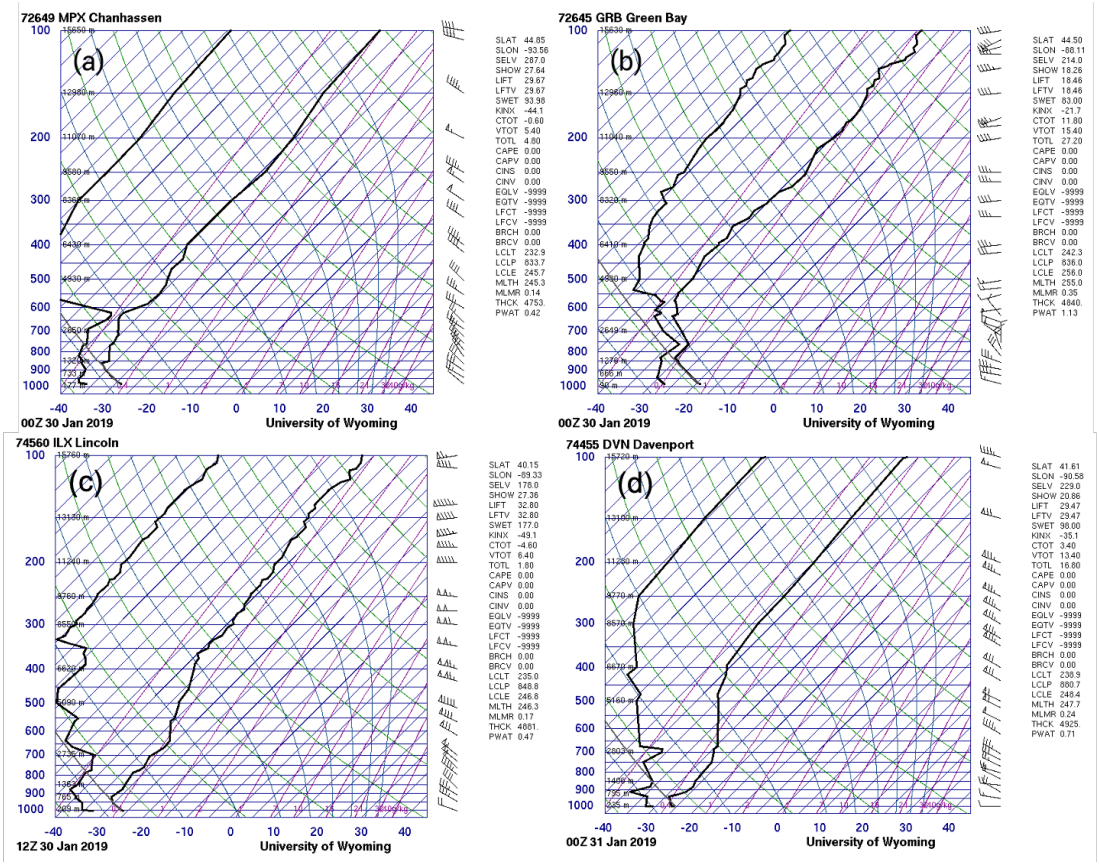

Figure 4.6: Operational National Weather Service radiosonde measurements taken from: (a) Chanhassen (Twin Cities), Minnesota at 00 UTC on 30 January 2019; (b) Green Bay, Iowa at 00 UTC on 30 January 2019; (c) Lincoln, Nebraska on 12 UTC 30 January 2019; (d) Davenport, Iowa on 00 UTC 31 January 2019. These soundings were taken from the University of Wyoming's Department of Atmospheric Sciences' sounding archive.

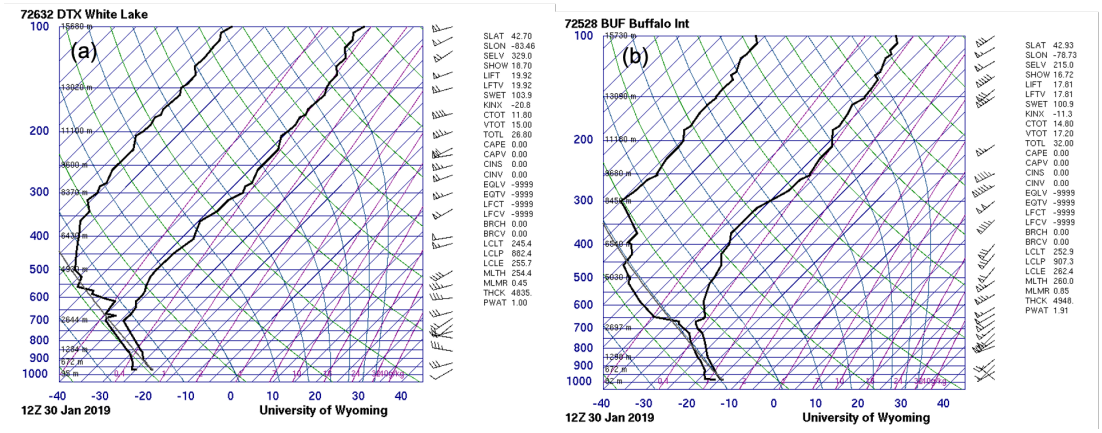

Figure 4.7: Operational National Weather Service radiosonde measurements taken from: (a) White Lake (Detroit), Michigan on 12 UTC 30 January 2019; (b) Buffalo, New York on 12 UTC 30 January 2019. These soundings were taken from the University of Wyoming's Department of Atmospheric Sciences' sounding archive.

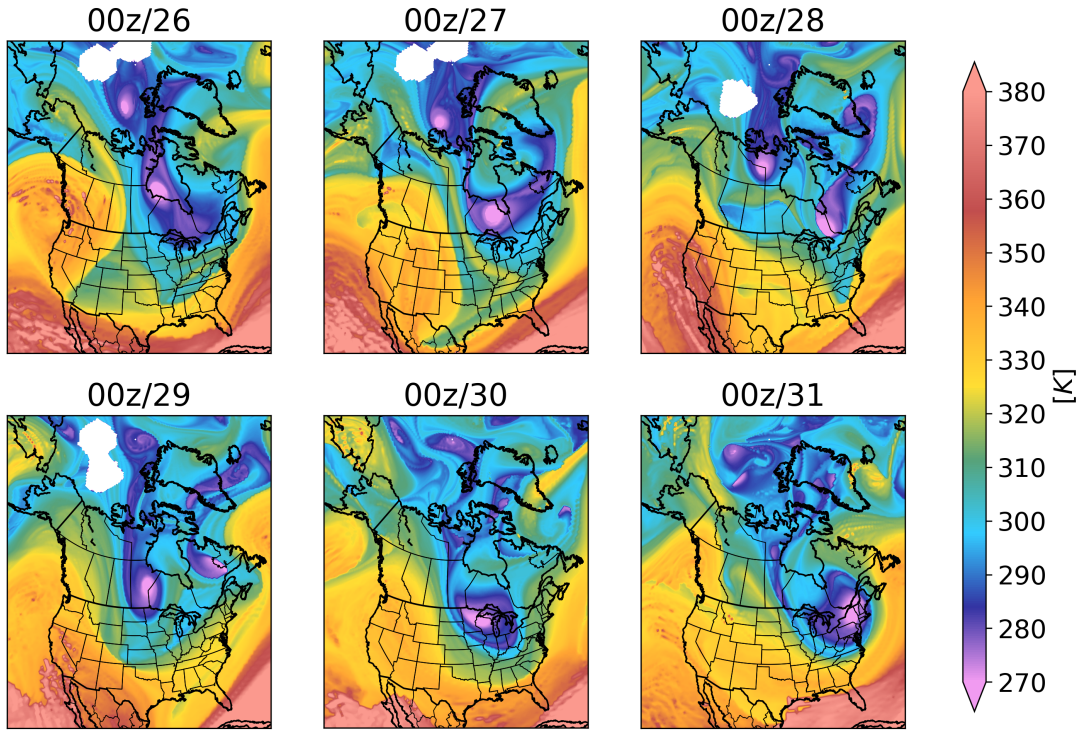

Figure 4.8: Potential temperature (K) on the 2 PVU surface in the control run. The top right panel is 00z 26 January 2019; 24 hours into the simulation. Each subsequent panel advances 24 hours.

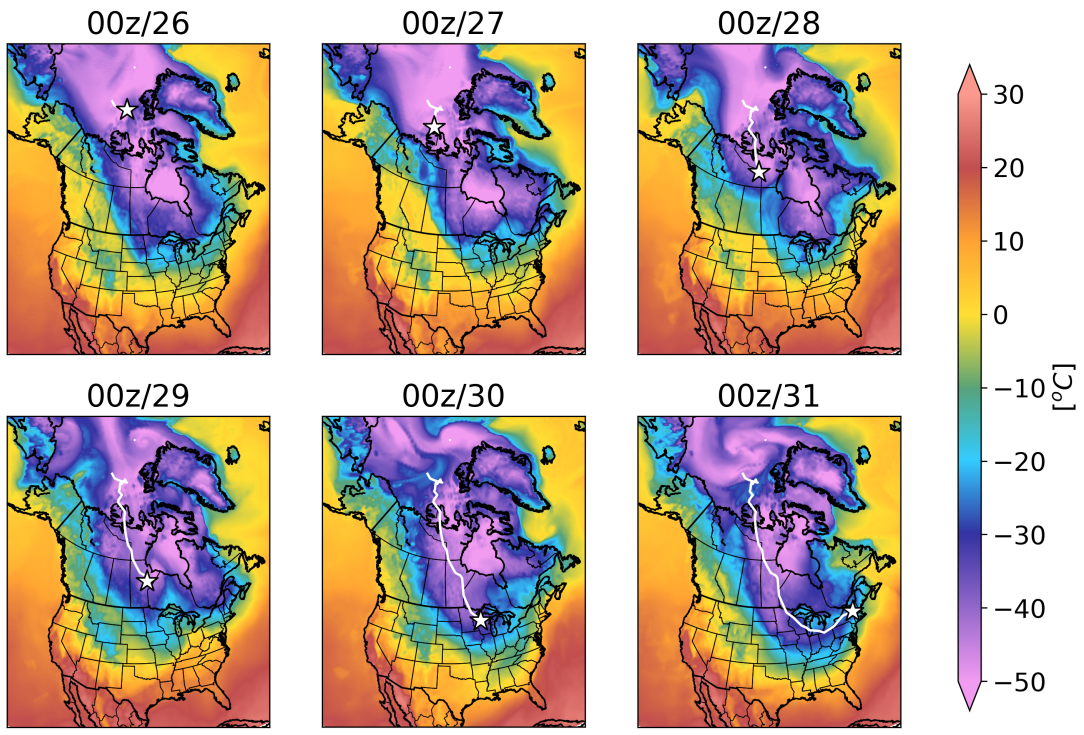

Figure 4.9: Control run forecast 2-m temperature (^oC). The white line denotes the track of the TPV, and the white star denotes the locations of the TPV at the respective times. The top right panel is 00z 26 January 2019; 24 hours into the simulation. Each subsequent panel advances 24 hours.

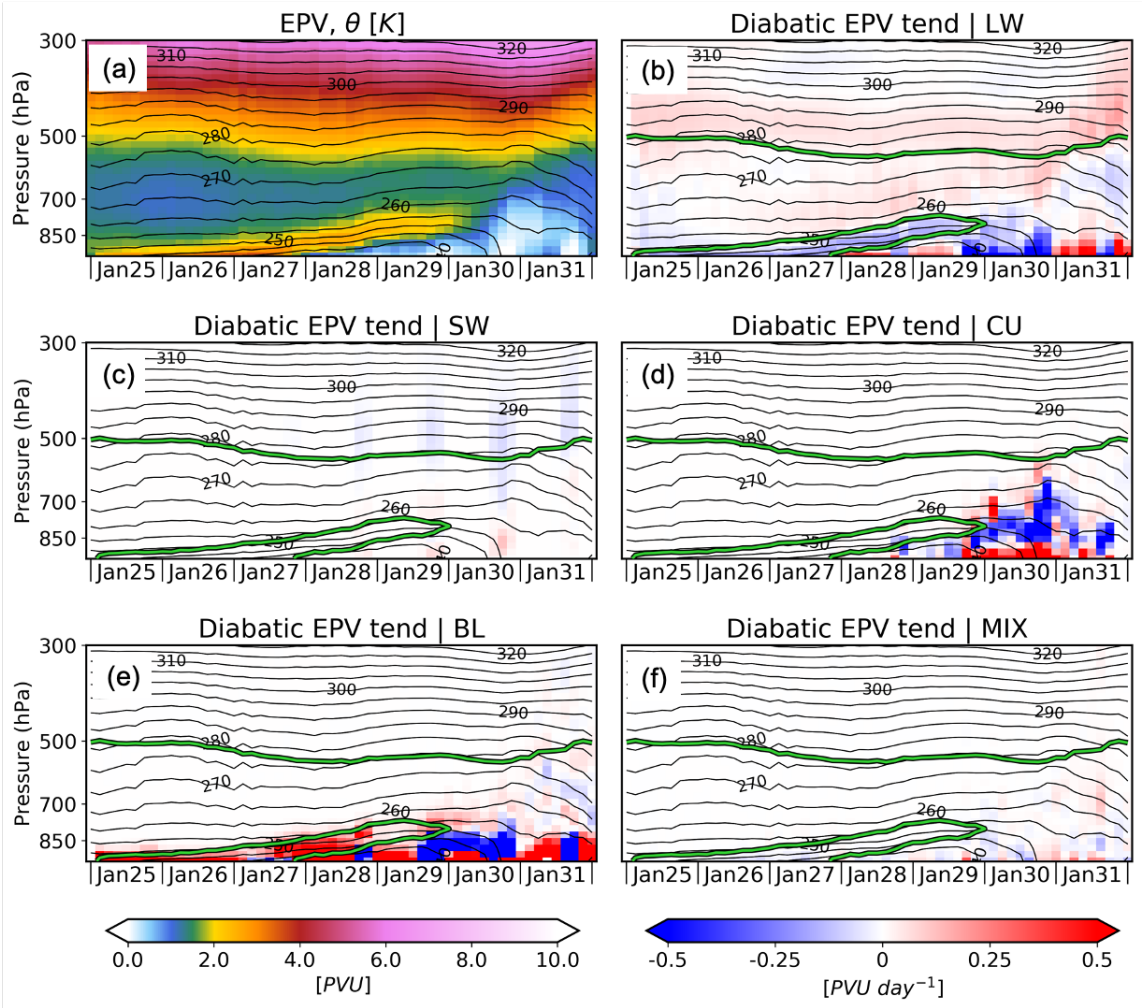

Figure 4.10: Vertical cross-section of Ertel potential vorticity (EPV) and potential temperature averaged over an area defined by a 400 km radius from the center of the TPV. The subsequent panels show the (a) potential temperature and (b) potential vorticity tendencies from longwave radiation (LW), (c) shortwave radiation (SW), (d) cumulus (CU), (e) boundary layer (BL), and (f) mixing (MIX) over this area.

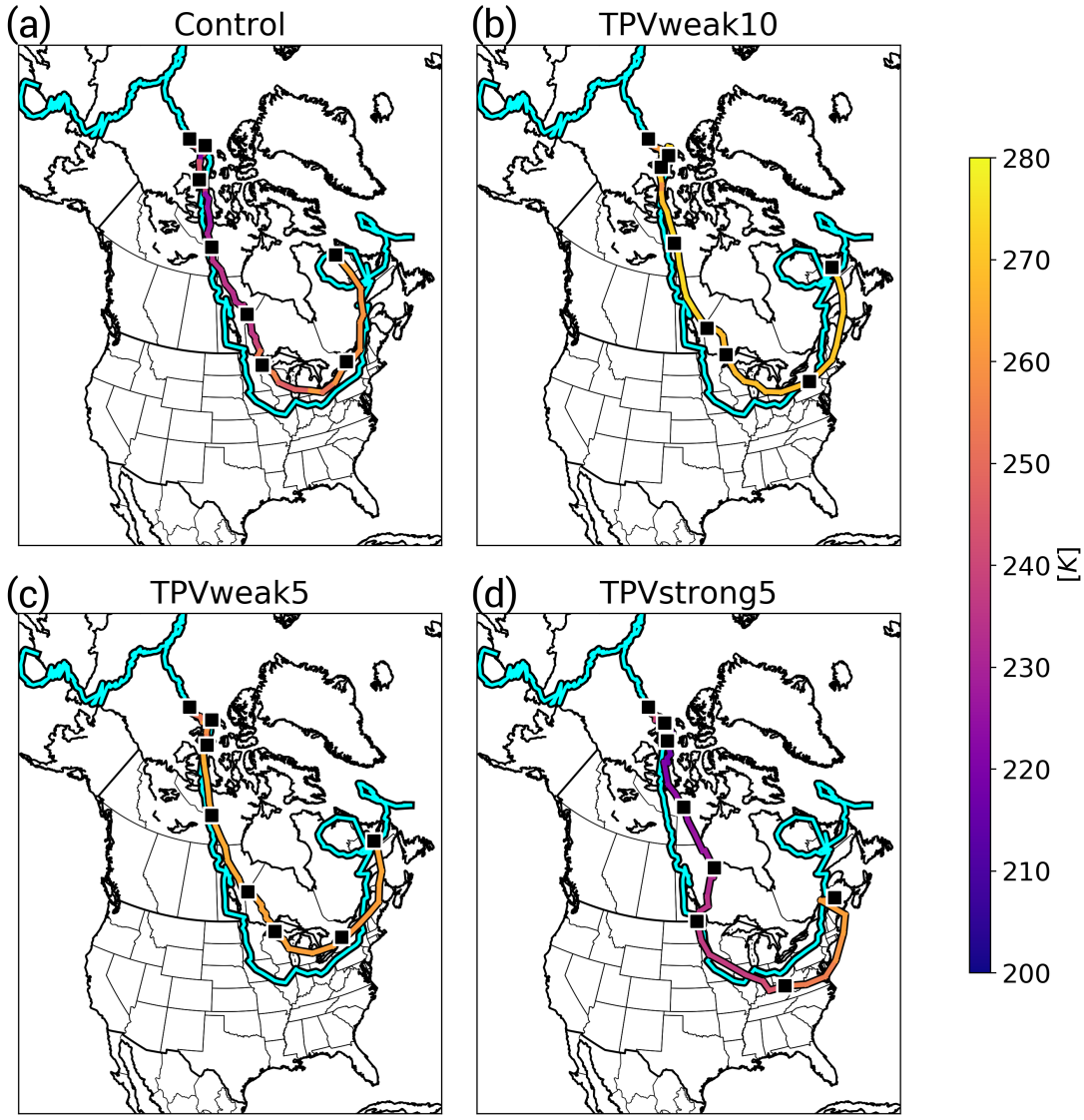

Figure 4.11: Track of the TPV in each simulation: (a) Control, (b) TPVweak10, (c) TPVweak5, (d) TPVstrong5. The cyan line denotes the track of the TPV in the ERA-5 reanalysis. Squares denote the 24-hr TPV positions at 00z for the four simulations. The color of the track corresponds to the depth of the TPV given by the minimum potential temperature on the 2 PVU surface.

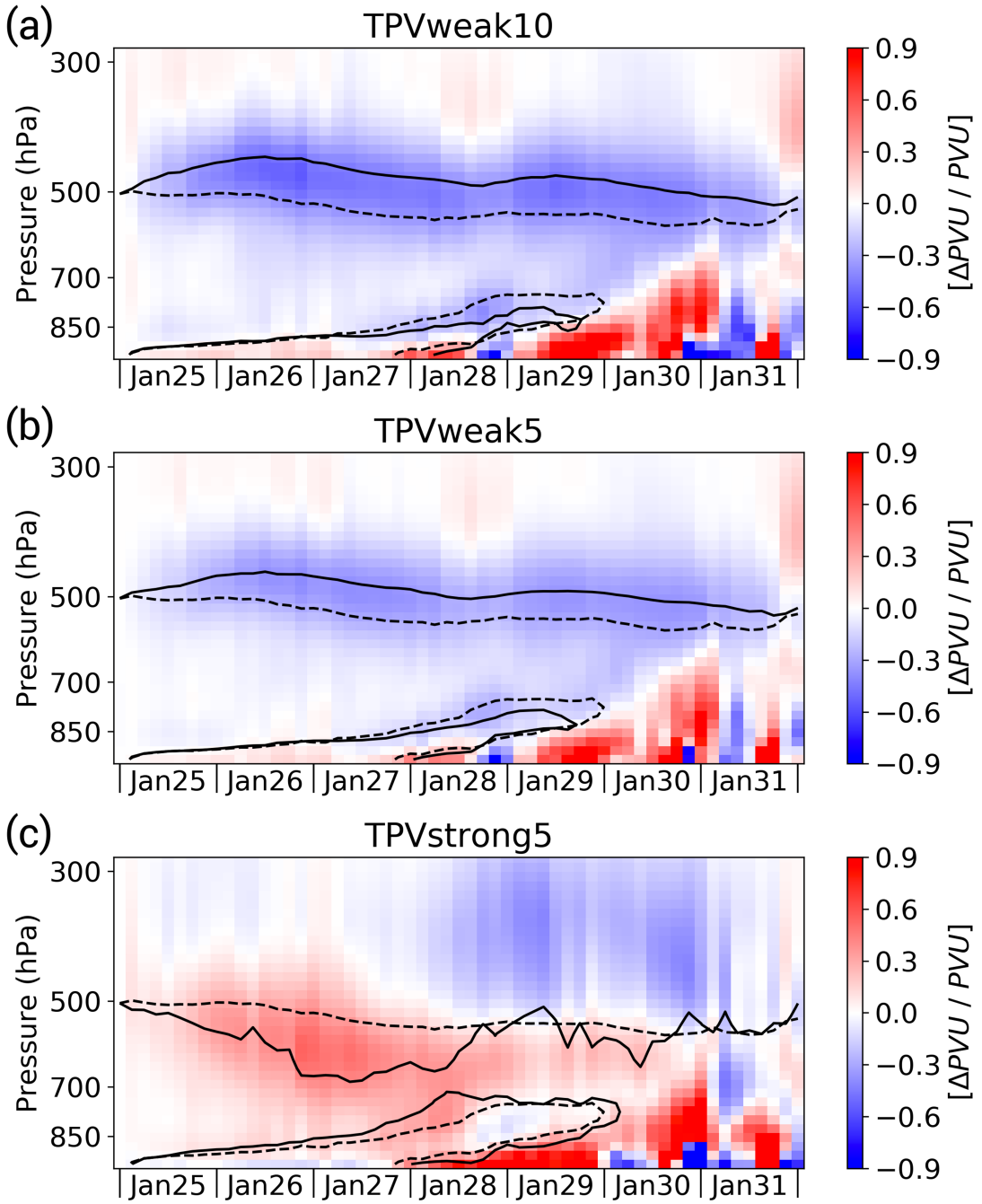

Figure 4.12: Differences in EPV over the 400 km radius area from the TV center from the control and (a) TPVweak10, (b) TPVweak5, and (c) TPVstrong5. The color fill is the EPV difference between the modified run and control run, scaled by the average EPV of the two runs. In each panel, 2 PVU EPV is contoured for the modified run (solid line) and the control run (dashed line).

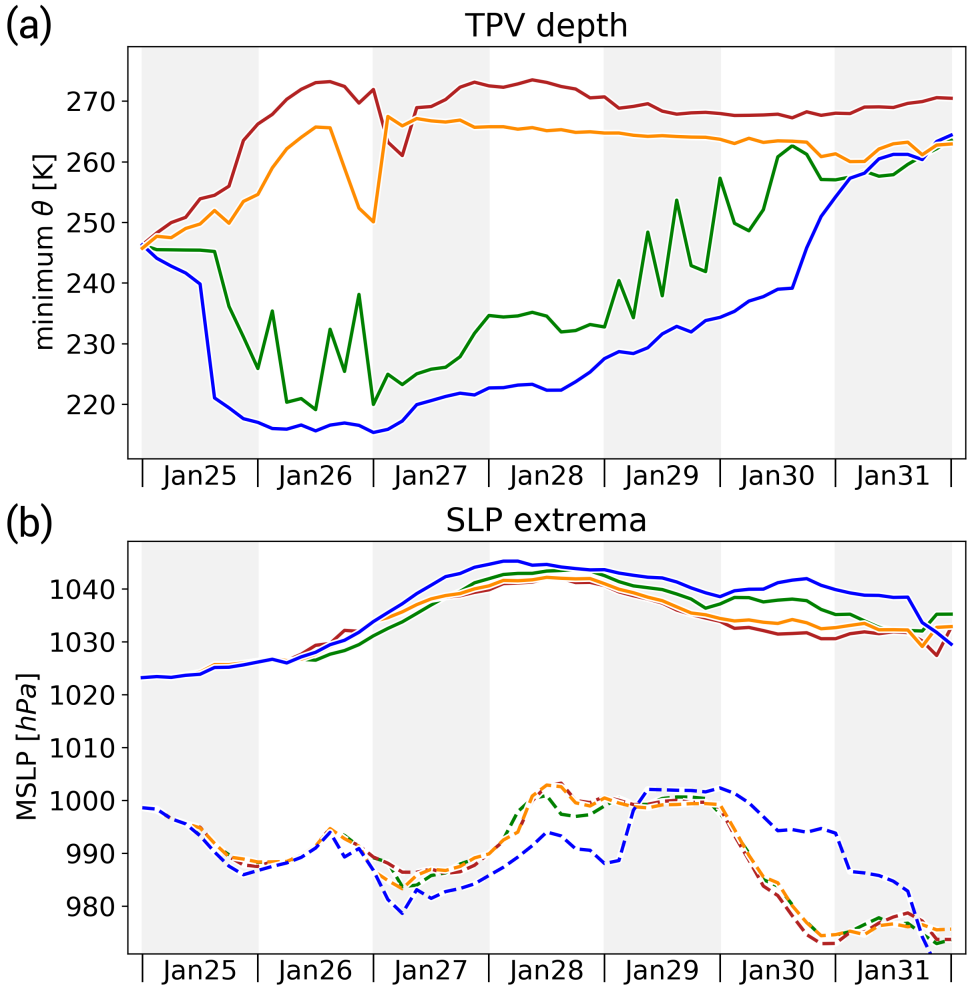

Figure 4.13: Time plots from the 7-day forecast runs for the control (green), TPVweak10 (red), TPVweak5 (orange), and TPVstrong5 (blue). (a) Minimum potential temperature on the 2 PVU surface in the TPV. (b) SLP maximum (solid line) and minimum (dashed line) within a 1600 km radius of the TPV center.

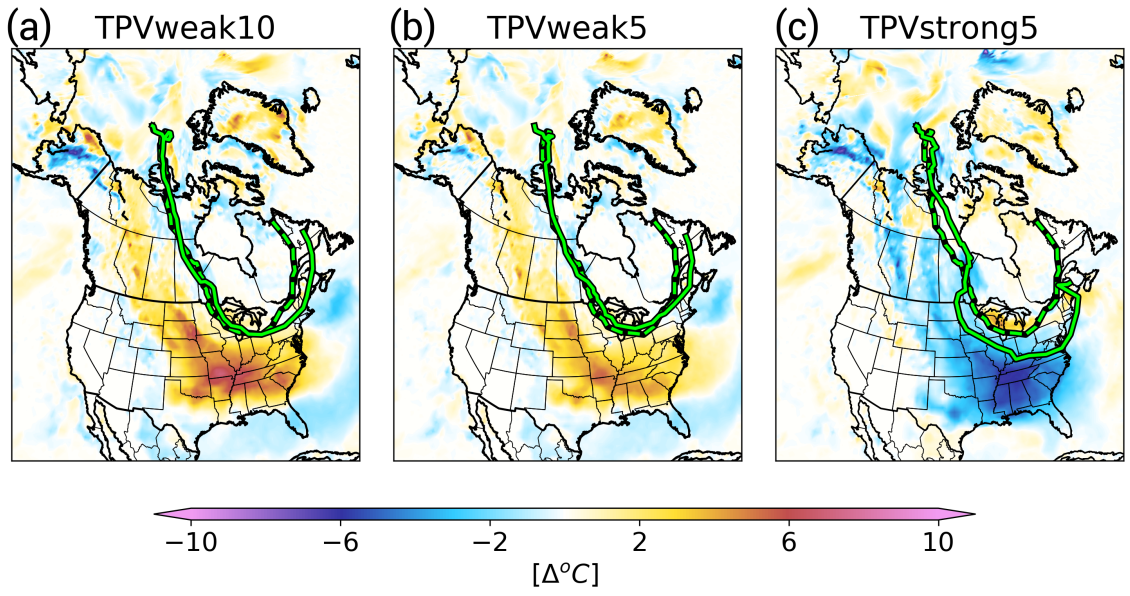

Figure 4.14: Difference of each modified simulation from the control of the coldest 24-hour running-mean 2-m temperature during the 7-day forecast period, for the (a) TPVweak10 run, (b) TPVweak5 run, and (c) TPVstrong5 run. Solid green line marks the track of the TPV in the modified simulations, and the dashed green line marks the track in the control.

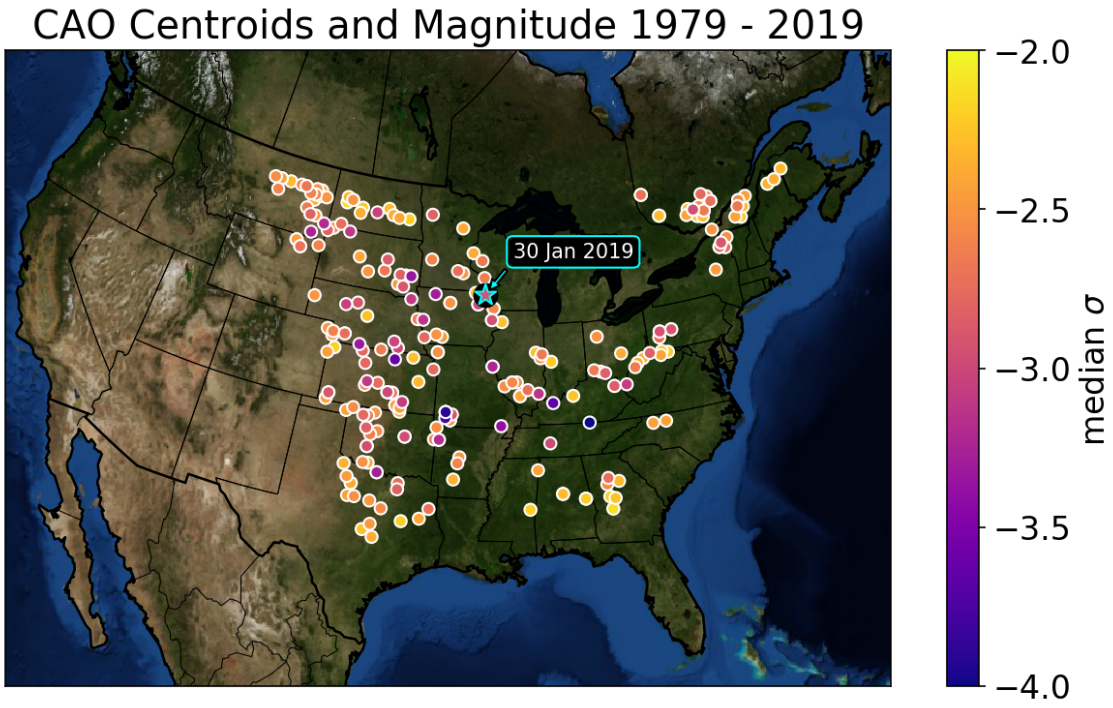

Figure 4.15: Points of CAO centroids and corresponding median standardized temperature anomaly given by the color, for period from 1979 through 2019.

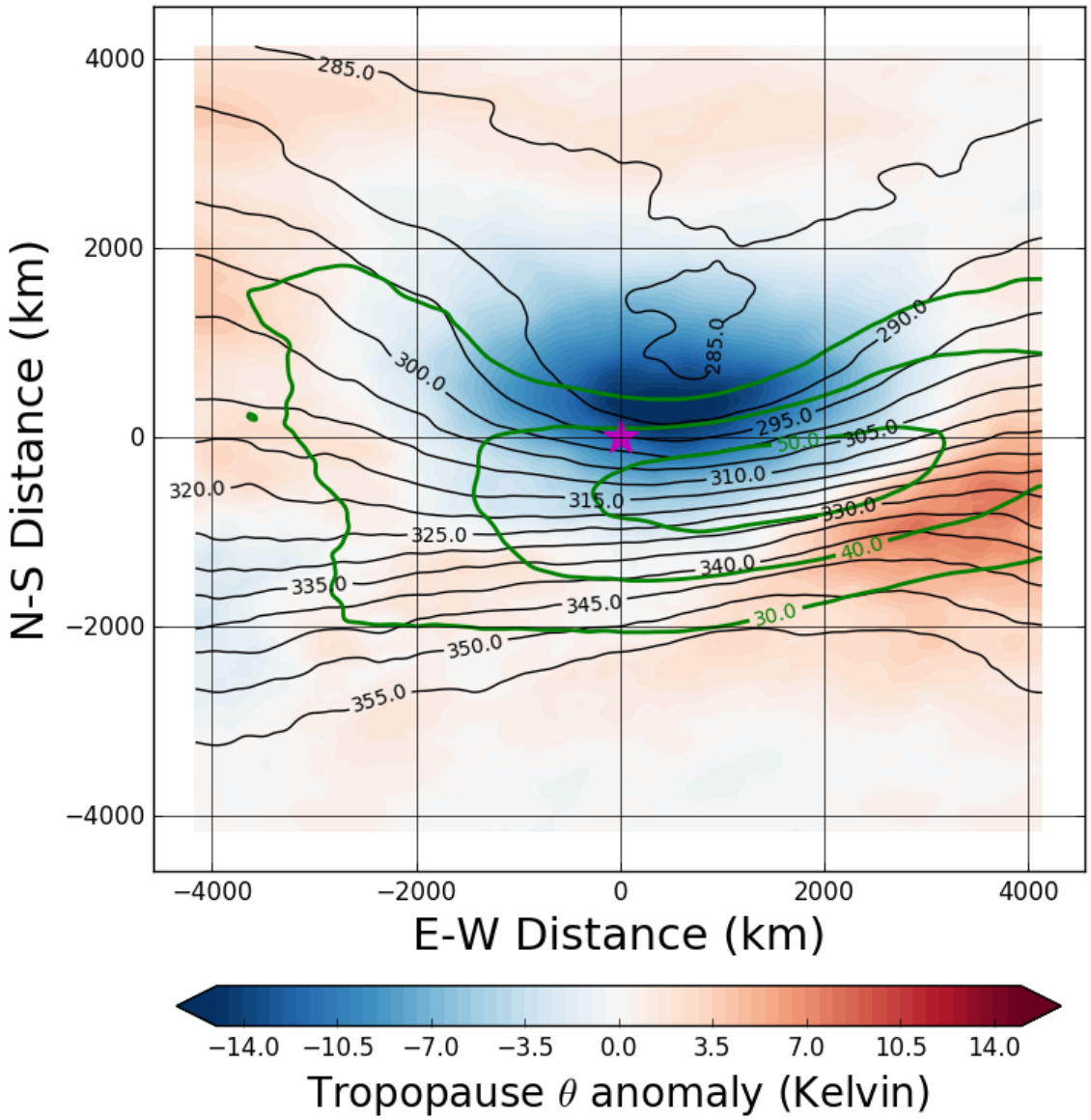

Figure 4.16: The potential temperature anomaly on the tropopause (shaded), potential temperature (black lines) and 250 hPa wind (green lines) on the 2 PVU level plotted relative to the CAO centroid. The data was obtained from ERA-5 reanalysis

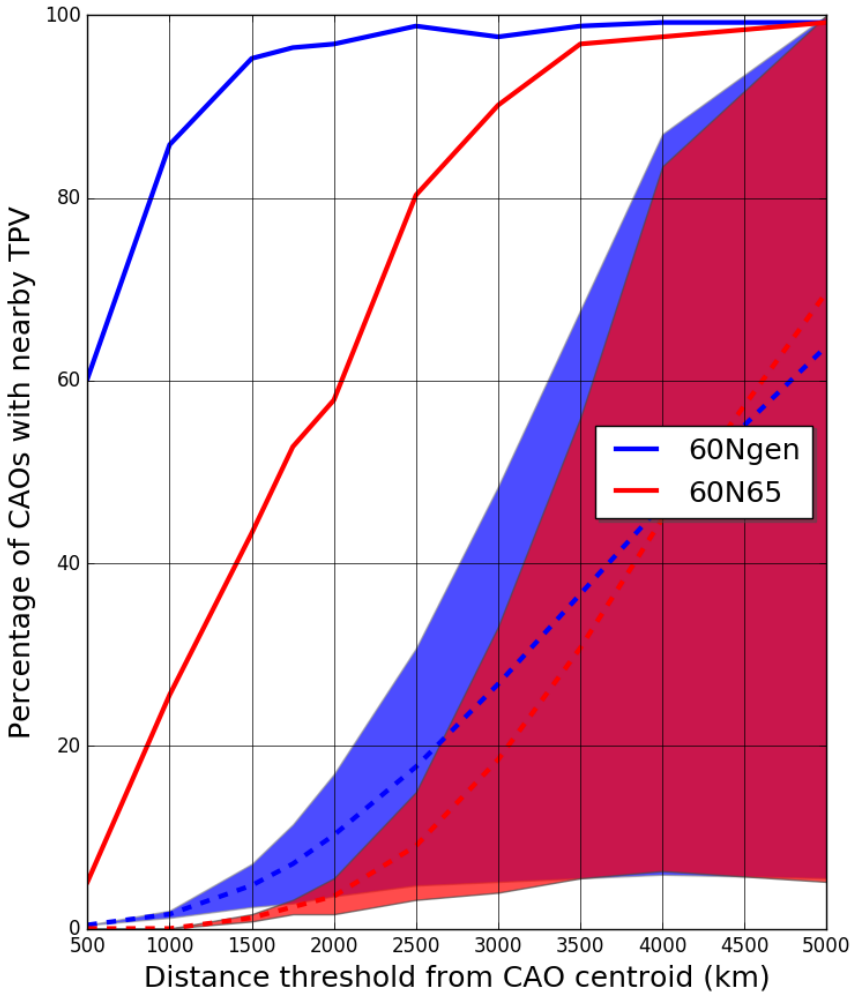

Figure 4.17: The percentage of time there is a TPV within a specified distance threshold (x axis) given a CAO location at the time of the CAO. The blue solid line (60Ngen) represents all tropopause PV anomalies originating poleward of 60N. The red solid line (60N65) utilizes the TPV definition that the TPV spends 60% of its lifetimes poleward of 65N. The blue dashed line and shading show the average percentage of time that there is a 60Ngen TPV within a specified distance threshold (x axis) for a random December-January-February day between 1979-2019. The random sample was created using all CAO locations with random dates and repeating 1000 times. The shading is the 95% range of this sample. The red dashed line and shading represent the same approach but for the 60N65 TPVs.

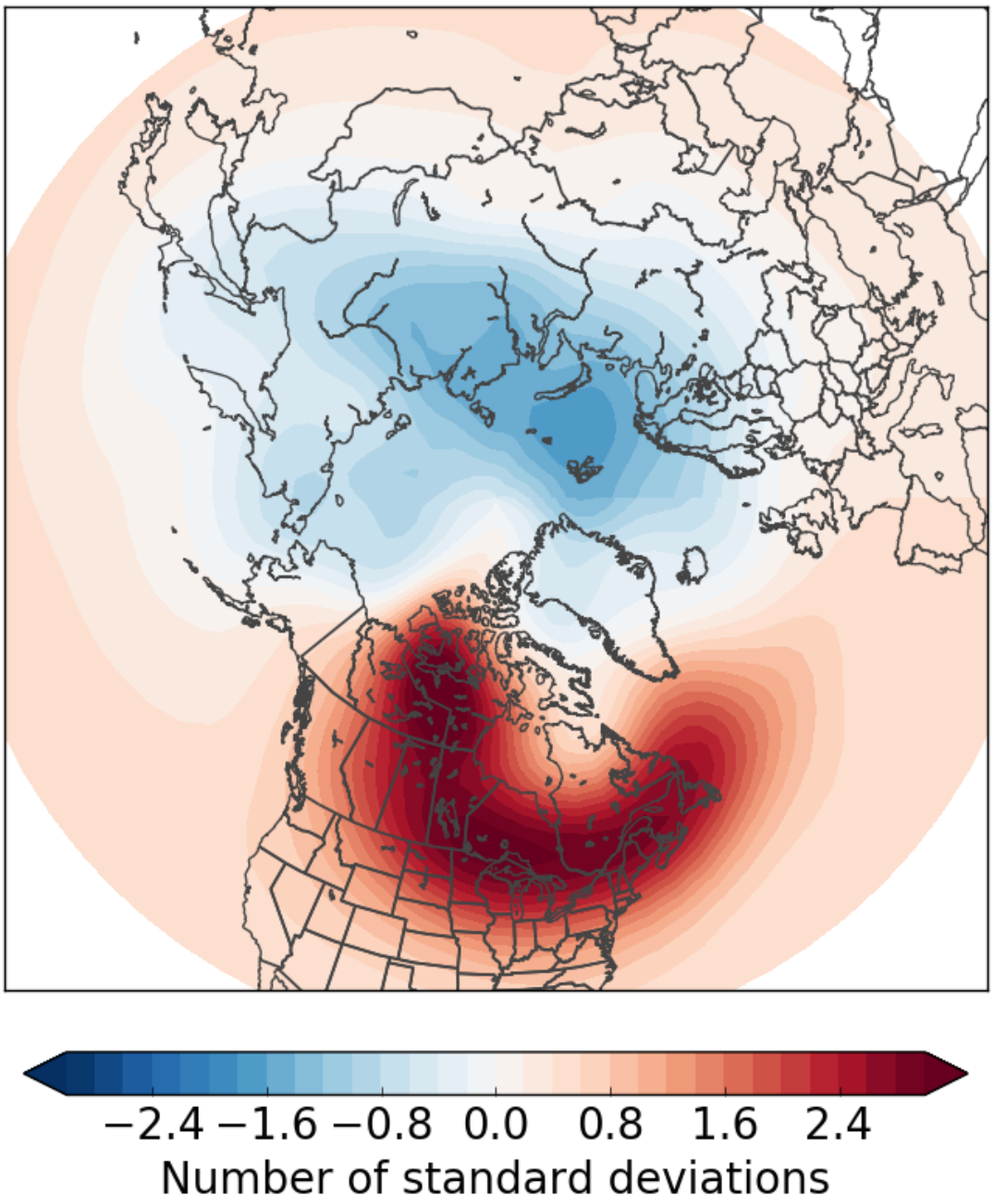

Figure 4.18: Standardized track density for TPVs passing within 1000km of CAO centroids. The track densities are plotted relative to the full winter TPV climatology as determined from ERA-Interim reanalysis.

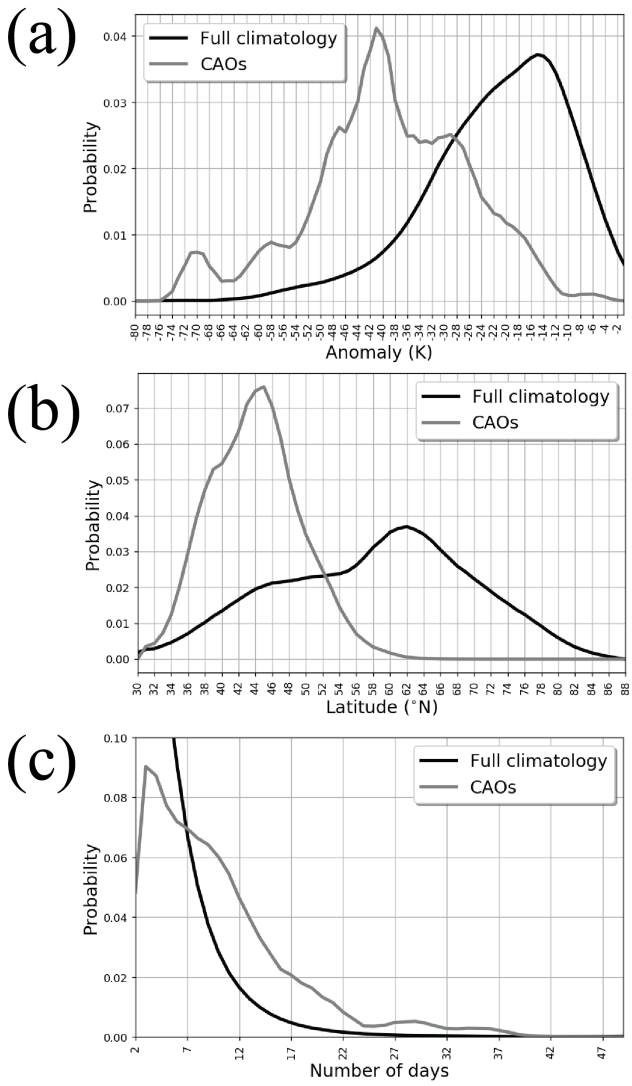

Figure 4.19: Cyclonic tropopause polar vortex structural properties of (a) minimum core anomaly, (b) minimum latitude, and (c) lifetime. The bin interval is 1 K in (a), 1° latitude in (b), and 1 day in (c). The black contours correspond to the full climatological record, while the gray contours correspond to the vortices that are located 1000 km or less from a cold air outbreak. P-values from the K-S test are in 3.62×10^{-101} (a), in 8.30×10^{-128} (b), and 3.02×10^{-56} in (c). Anomalies in (a) are computed with respect to the long-term daily climatological mean (1979-2010) of tropopause potential temperature at the corresponding grid point of the vortex core (vortex core minus climatological value).

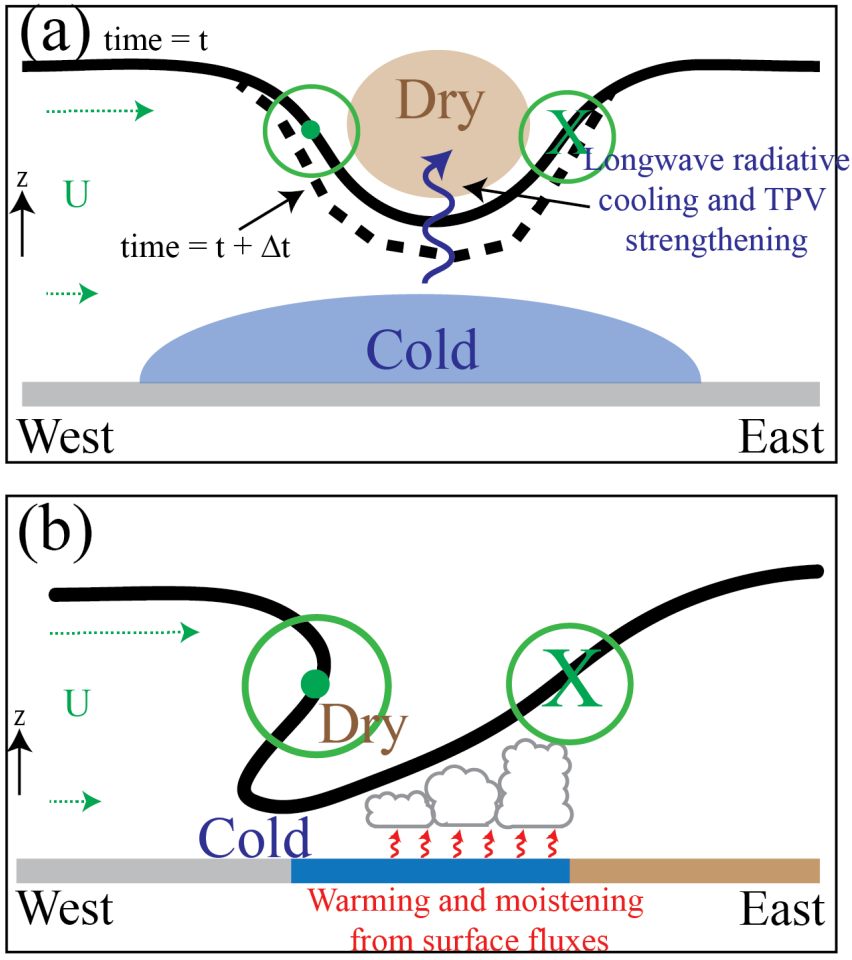

Figure 4.20: Schematic of the interaction between the structure of the TPV and the CAO. (a) The structure of the TPV within the Arctic. There is a lowering the tropopause with a cyclonic circulation around the lowered as indicated by the conventional symbols for flow into and out of the page. The vertical shear in the background westerly (U) winds are relatively weak. Long wave cooling increases the intensity of the TPV with a lowering of the tropopause. (b) The structure of an intense TPV moving into middle latitudes. As the TPV begins to interaction with the polar jet, the vertical shear (U) increases and the system begins to tilt with height. The cyclonic flow around the center can also increase. PV is destroyed and warming and the moistening of the lower troposphere occurs as the TPV moves over warm and moist surfaces. The example is consistent with the observed lake effect snows.

Chapter 5

Dynamics behind a record-breaking trough over Mexico and internal atmospheric variability during El Niño

This chapter investigates the dynamics associated with an extreme winter storm that occurred over Mexico during the strong 2015-2016 El Niños. The chapter is based upon and largely taken from Lillo et al. (2019). This extreme was well predicted and unlike past strong El Niños, the North Pacific preceding this event was characterized by significant synoptic-scale Rossby wave activity on the midlatitude jet stream including multiple wave packets tracking around the globe during February and March. The interaction of one of these packets with the subtropical anticyclone aloft resulted in a large anticyclonic wave break over the east Pacific, leading to the amplification of the downstream trough over Mexico. The ability of numerical weather prediction to capture this extreme trough is directly related to the predictability of the Rossby wave packet. These results are also placed within the context of the relationship between El Niños, Rossby wave activity, and extreme events in western North America.

5.1 Introduction

An extreme winter storm impacted Mexico in March 2016, in association with an exceptionally deep upper-level trough characterized by 500 hPa heights near 9 standard deviations below average (Fig. 5.1a). This storm had numerous detrimental societal and economic impacts. Much of Mexico was in a state of emergency due to severe wind and cold weather. An estimated four million people lost power, primarily in the states of Mexico and Puebla in the south central region of the country. In addition, hundreds of injuries and fatalities were caused by the high wind and hypothermia. Schools were closed in 12 states. Major agricultural damage was declared in the states of Oaxaca, Sinaloa, Durango, San

Luis Potosí, Tamaulipas, and Zacatecas. In the state of Sinaloa alone, nearly 50,000 acres of corn and wheat were harmed by the wind and heavy precipitation. The event was also responsible for harmful environmental impacts. Freezing cold lead to a mortality rate of over 30% of butterflies in colonies of the Monarch Butterfly Biosphere Reserve (Brower et al. 2017). Strong winds with this storm toppled thousands of trees, destroying shielded sanctuaries and scouring out the microclimate that butterflies had relied on in the past cold air outbreaks.

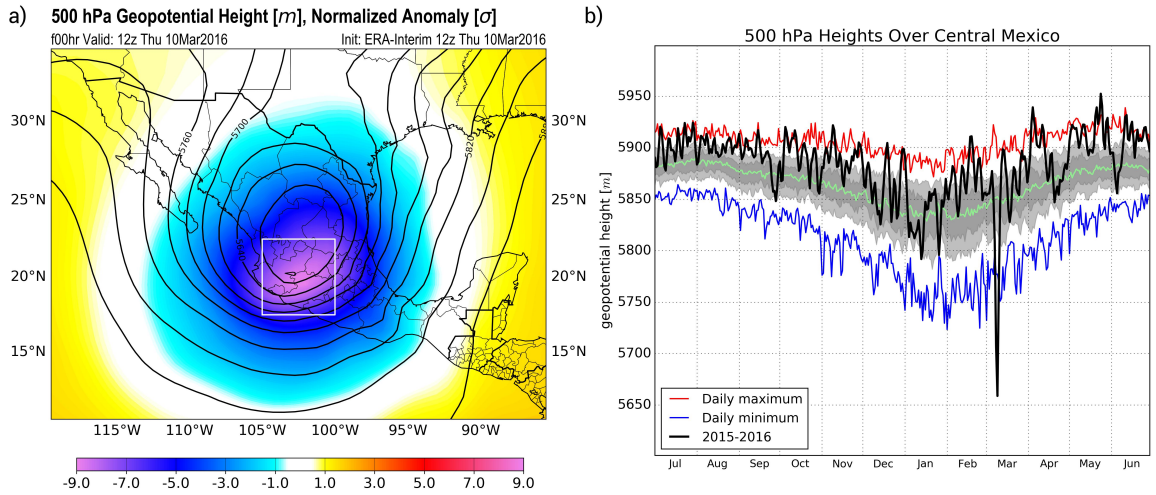

Figure 5.1: a) Contours of 500 hPa heights at 12 UTC on 10 March 2016 from ERA Interim. The standard deviation of the anomaly from the climatological mean is given by the color shading. b) Daily-mean 500 hPa heights over central Mexico indicated by the white box on the map ($17.5^oN - 22.5^oN, 100^oW - 105^oW$) from NCEP/NCAR Reanalysis for 1948-2015. Light gray fill marks the 10-90 percentile range and dark gray fill marks the 25-75 percentile range. Red, green, and blue lines mark the daily maximum, median, and minimum respectively. The black line marks the 2015-2016 daily heights.

The impending hostile environment was lead by a cold front stretching across northwest Mexico on 7 March. The synoptic evolution and societal impacts during the days that followed are depicted in Fig. 5.2. Temperatures plummeted from near 20^oC to below freezing with winds gusting to 22 m/s (50 mph). For the next three days, most of central

Mexico averaged between 6^oC and 10^oC below average (Fig. 5.3a) following what was a temperate winter (Fig. 5.3c). Sleet and snow was reported over the Sierra Madre Occidental and as far south as Guadalajara, and frost was reported in Mexico City. Along the west coast of Mexico, snow was recorded for the first time in Northern Sinaloa and western Durango with record wind and low temperatures reaching southward to as far as Chiapas and Oaxaca. Downstream of the trough, deep-layer moisture transport from the Gulf of Mexico fueled heavy rain in strong to severe thunderstorms from Texas to Louisana, Arkansas, and Mississippi. Because of the cut-off nature of the trough, this regime was stagnant between the 8th and 12th, during which time widespread rainfall over one foot (Fig. 5.3b) resulted in devastating flooding (Breaker et al. 2016).

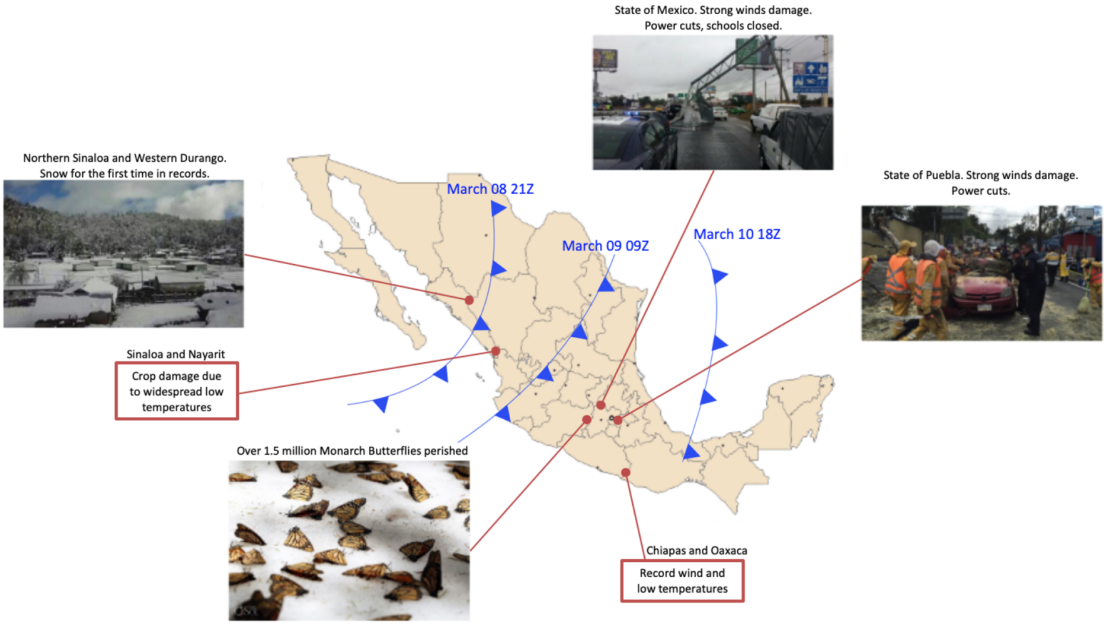

Figure 5.2: Positions of the surface cold front at 21z 8 March, 9z 9 March, and 18z 10 March 2016. Inset figures and annotations point to locations of societal impacts from the cold air outbreak.

The origin of the bitter cold beneath the deep upper-level trough was investigated through backward trajectories which show this air mass primarily originated over the subtropical and middle latitude Pacific (Fig. 5.4). These trajectories suggest that this event had a different synoptic character than many of the cold air outbreaks that impact Mexico which often originate in Canada with a strong anticyclone and move rapidly along the lee side of the Rockies due to interaction of the terrain with the evolving synoptic flow (Colle and Mass 1995; Schultz et al. 1998). These lee-side cold air outbreaks are often referred to as Nortes (Magaña et al. 2003) and are discussed, for example, in Henry (1979), Reding (1992), Schultz et al. (1997), Pérez et al. (2014), and Luna-Niño and Cavazos (2018). The frequency and structure of cold surge activity varies with El Niño / Southern Oscillation (ENSO) (Magaña et al. 2003; Magaña and Ambrizzi 2005) with less cold surges during El Niño. This winter storm took place during the strong 2015-16 El Niño (e.g., L'Heureux et al. 2017; Dole et al. 2017) that will be described in the next section.

5.2 A Flavor of Strong El Niño

The winter of 2015-2016 featured one of the strongest El Niños on record (e.g., Blunden and Arndt 2016; L'Heureux et al. 2017; Santoso et al. 2017; Dole et al. 2017). Seasonal predictions of sensible weather made in the fall of 2015 were based heavily on this exceptional ENSO state. As discussed in Dole et al. 2017, the tendency for heavy rainfall to occur in California in association with strong El Niños in the past brought specific interest to this event given the region's persistent historic drought. However, the drought would not be quelled this winter (Fig. 5.3d). One wild card noted in seasonal outlooks was that SSTs across the North Pacific did not resemble the typical configuration of a positive Pacific Decadal Oscillation (PDO) that would normally accompany such an authoritative tropical regime (Newman et al. 2003). Above average SSTs controlled much of the subtropical and mid-latitude ocean, especially in a region eloquently labeled the "warm blob" between

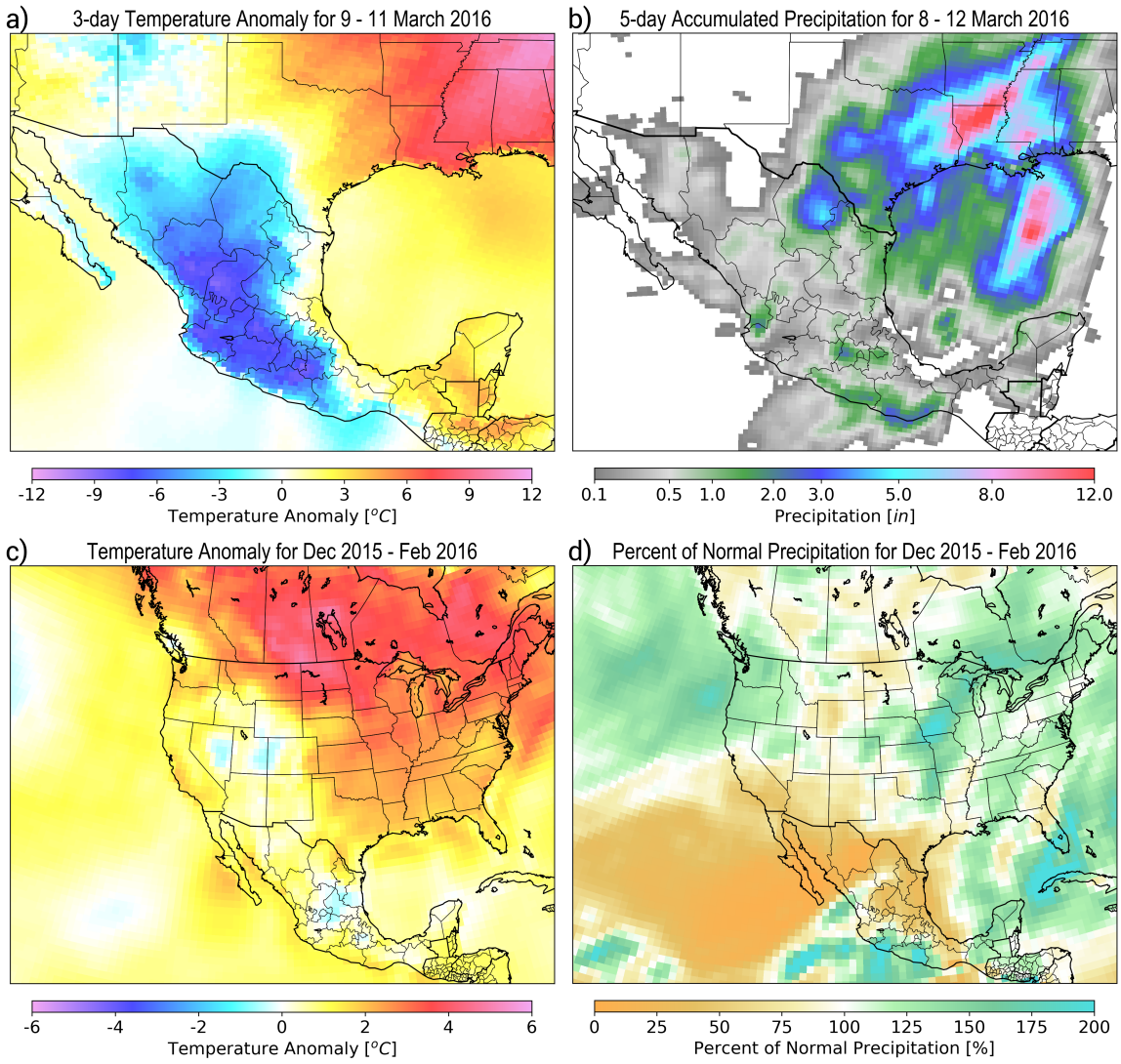

Figure 5.3: Summary of temperatures and precipitation during the March storm using North American Regional Reanalysis (Mesinger et al. 2006): a) 3-day 2m temperature anomaly for 9 to 11 March 2016, b) 5-day accumulated precipitation for 8 to 12 March. Summary of the winter of 2015-16 using ERA-Interim (Dee et al. 2011b): c) temperature anomaly for December 2015 through February 2016, d) precipitation percent of average for December 2015 through February 2016. All anomalies use a 1981-2010 climatology.

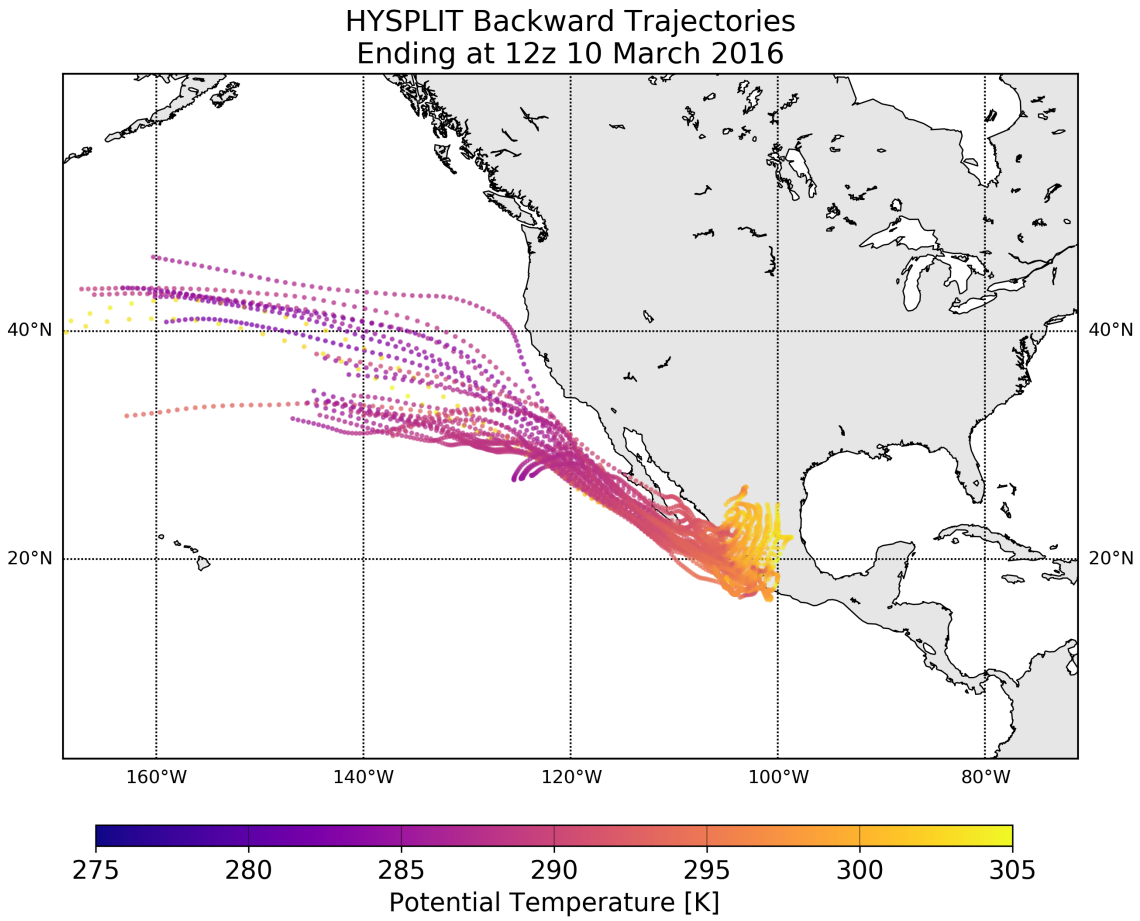

Figure 5.4: Backward trajectories for 120 hours starting from grid points between 1 km above ground level and 500 hPa, over central Mexico at 12 UTC on 10 March 2016 using NOAA ARL's HYSPLIT program (Stein et al. 2015). The input data was from the North American Regional Analysis. Each point is one hour, and the color refers to the potential temperature.

Hawaii and Baja California (e.g., Peterson et al. 2015). As a result, the meridional SST gradient was less than typically present with a strong El Niño.

Strong El Niños feature enhanced tropical convection in the central and eastern Pacific, associated with a dominant Hadley cell and attendant twin anticyclones at the subtropical tropopause (Ropelewski and Halpert 1987; Oort and Yienger 1996). Through conservation of angular momentum, the upper-level poleward branch of the Hadley cell powers an enhanced subtropical jet from the central Pacific across tropical/subtropical North America (Rosen et al. 1984). The latent heat release associated with tropical convection reduces stability above the level of maximum heating and pushes the tropopause upward along with a decrease in potential vorticity (PV). Strong divergence above the convection advects the low PV air out of the tropics. As these parcels trace poleward they encounter a northward-directed PV gradient as a result of increasing planetary vorticity by latitude, and can become large negative PV perturbations superimposed on the background flow field (Sardeshmukh and Hoskins 1988). In the presence of a jet stream with a significantly tightened PV gradient within the background flow, high wavenumber (short wavelength) Rossby waves, and their associated synoptic weather systems, are channeled downstream along the spine of the PV gradient maximum (Hoskins and Ambrizzi 1993). Low wavenumber Rossby wave activity emanating from the initial perturbation is free to propagate further poleward (e.g. Fig. 2 in Hoskins and Ambrizzi 1993).

In past strong El Niño events, the subtropical jet was fast and narrow yielding a large background PV gradient (Held and Hou 1980; Bell and Halpert 1998). This PV distribution means that the jet acts as a filter in which only the lowest wavenumber Rossby wave disturbances triggered from tropical convection can reach beyond the sub-tropics, essentially shadowing higher latitudes from the shorter wavelengths. The most common manifestation of this Rossby wave dispersion is the Pacific / North American (PNA) pattern (Wallace and Gutzler 1981), in which a planetary-scale wave response emanates northeastward from enhanced convection over the equatorial Pacific. As a result of this filtering effect, the winters

with an augmented subtropical jet would be dominated by low wavenumber perturbations in the mid-latitudes.

In stark contrast to this painting of a canonical strong El Niño, the winter of 2015-2016 was characterized by a weaker thermal gradient in SSTs due to the warm waters across portions of the subtropics and middle latitudes. Utilizing two ensembles of climate simulations, Quan et al. (2018) note the importance of differences in the boundary conditions outside of the ENSO core-region and a weaker and poleward-shifted upper level low anomaly over the north Pacific compared to the typical ENSO teleconnection. We suggest that the wider expanse of warm waters may link to their conclusions, in addition to producing a wider and weakened Hadley cell yielding a less-dominant subtropical jet. These shifts can all contribute to a weaker poleward-directed PV gradient in the subtropics, and as a result, Rossby wave activity and related storm tracks and patterns of rainfall could be expected to have different behavior in the subtropics and mid-latitudes than past strong El Niño winters. Flow patterns through 2015-16 were thus likely to be characterized by a mix of both low and high wavenumber activity, and greater impact on significant weather coming from internal variability. The importance of this internal variability in determining the relationship between ENSO and rainfall on the west coast of North America has been expressed by Deser et al. (2018).

In order to examine differences in the behavior of Rossby wave activity dependent on the structure of the Pacific jets and PV field, we treat the atmosphere as a refractive medium that guides the path of Rossby wave activity of varying wavelengths. Similar to geometric optics, the group velocity of Rossby wave activity can be described as following rays that track and bend according to an index of refraction, n (Hoskins and Karoly 1981; Hoskins and Ambrizzi 1993). Where n is a real number, the basic state flow supports the existence of Rossby wave activity of a given zonal wavenumber, k. An imaginary n, or negative n^2, identifies where this wave activity is evanescent, and at n^2 equal to zero this wave activity is reflected or absorbed (Held 1983). A wave guide for waves of a given k is thus defined by

a band of positive n^2 flanked to the north and south by negative n^2 (e.g. Fig. 2 in Hoskins and Ambrizzi (1993)). Originally from Matsuno (1970) and later derived by O'Rourke and Vallis (2016), n^2 can be written as

$$n^2 = \frac{1}{\overline{u} - c}\frac{\partial \overline{q}}{\partial \phi} - \frac{k^2}{cos^2(\phi)} \tag{5.1}$$

where u is the zonal wind, c is the zonal component of the Rossby wave phase velocity, $\frac{\partial q}{\partial \phi}$ is the meridional gradient in PV, and the overbar indicates the basic state, which in this study is defined by a one-month time-average. The zonal wavenumber of Rossby wave activity, k, is a constant for which n^2 is evaluated. The wave train during February and March 2016 featured circumglobal wavenumbers between 5 to 7 (which can be visually confirmed with the Hovmoller diagram in Fig. **??**a). Specifically, wavenumber 5 is at an important intersection where the wave is long enough to have a slow phase speed, but short enough to have dynamical significance for synoptic-scale weather. Additionally, it has been demonstrated to be associated with extreme ridges near the west coast of North America (Teng and Branstator 2017). For these reasons, in this study we evaluate n^2 for stationary zonal wavenumber 5 wave activity in 2016 and compare to past years using NCEP/NCAR reanalysis.

The frequencies of n^2 above and below zero in a given subset climatology provides some insight into the probability that Rossby wave activity of wavenumber 5 can be supported and guided eastward. The influence of ENSO on this metric is examined using a composite difference (El Niño minus La Niña) in the frequency of $n^2 < 0$ (Fig. 5.6a). From this analysis, there is a large region of significant positive difference in the central equatorial Pacific that is a product of a shifted Walker Circulation, where winds tied to large-scale convective outflow in the upper levels of the atmosphere are westerly during La Niña and easterly during El Niño. Over the Atlantic the subtropical jet wave guide is strongly favored during El Niño (Fig. 5.6a, red shading), and over the contiguous United States the polar jet wave guide is favored during La Niña (Fig. 5.6a, blue shading). Meanwhile, the differences

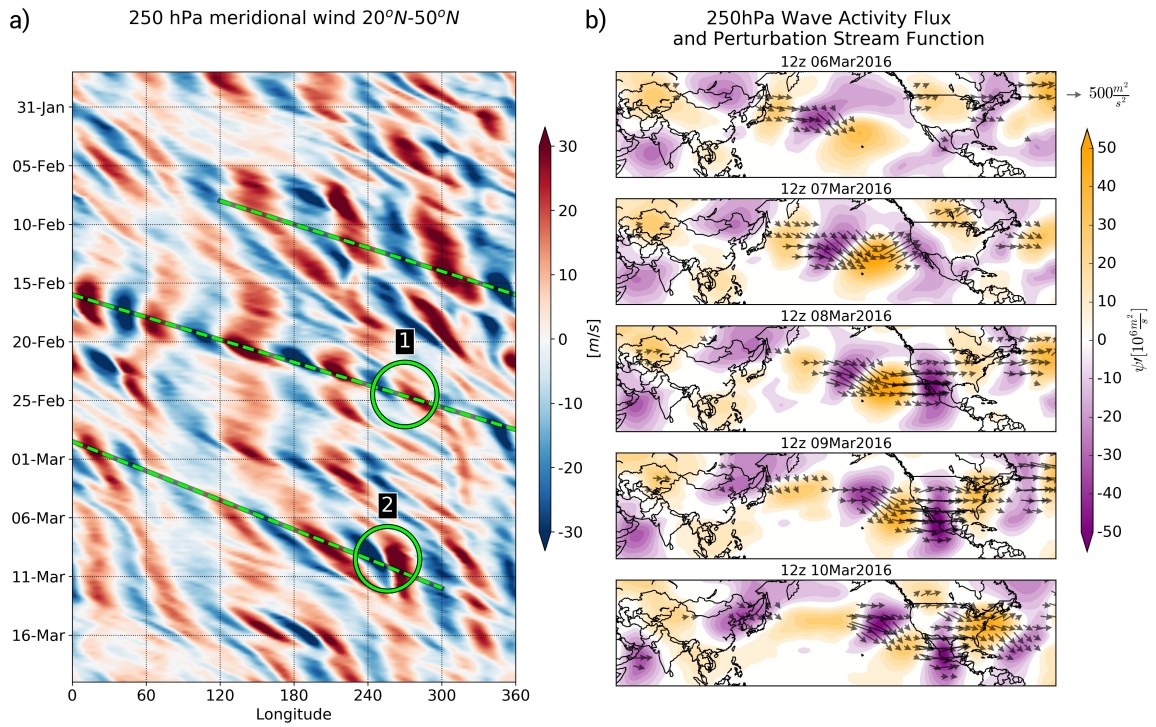

Figure 5.5: a) Hovmoller diagram of 6-hourly 250 hPa meridional wind from NCEP/NCAR Reanalysis, averaged between $20^oN - 50^oN$, for February and March 2016. The dashed green line marks the primary RWP during this period. The green circles denote two significant weather events directly connected to the RWP: (1) A tornado outbreak in the Southeast US on 23-24 February, and (2) the historic Mexico trough on 7-11 March. b) 250 hPa perturbation stream function (color fill) and wave activity flux (vectors) for 6 March through 10 March 2016.

are generally not statistically significant over the extratropical Pacific, suggesting little influence from ENSO on the pathways of Rossby wave activity upstream of North America. This lack of significant association within ENSO states lends itself to internal variability (Deser et al. 2017) leading to different time-mean patterns between ENSO cases.

A climatology of strong El Niño winters shows an indecisive Pacific as well (Fig. 5.6b). Large parts of the subtropics and mid-latitudes with frequencies between 0.3 and 0.7 indicate areas that have seen both positive and negative values of n^2; where there is diversity in the location of wave guides. This variability means that even within the subset of strong El Niños, the path of Rossby wave activity out of the tropics and in the mid-latitudes can vary yielding a range of influence in North America. The refractive index analysis demonstrates how the mid-latitude Rossby wave response associated with ENSO can vary beyond the canonical pattern. Indeed there can be considerable variability in the winter-time extratropical patterns and resulting sensible weather that coincides with the same low-frequency tropical forcing. While it may be tempting to dismiss this as noise on top of a canonical ENSO regime, this dismissal rejects the critical interactions that occur between the prevalent ENSO forcing, the distribution of basic state PV, and mid-latitude Rossby wave dynamics. Now we ask what are the connections between these players and how they shaped an unusual El Niño winter including the historic winter storm in Mexico and the lack of extreme rainfall in California.

During February 2016, the mid-latitude wave guide was well-defined in the western Pacific and shifted poleward from climatology (Fig. 5.7a). East of the dateline, the wave guide bent equatorward, and merged with the subtropical wave guide in the eastern Pacific into Mexico. We illustrate the theoretical path of Rossby wave activity using the ray tracing framework established in Hoskins and Karoly (1981). The group velocity for barotropic Rossby waves is derived as $\vec{c_g} = \frac{\partial \omega}{\partial \vec{K}}$ from the dispersion relation, $\omega = \overline{u}k - \overline{q}\frac{k}{|\vec{K}|^2}$ where $\vec{K} = k\hat{i} + l\hat{j}$ is the wavenumber vector. Ray paths are constructed by integrating forward $\frac{dx}{dt} = c_{gx}$ and $\frac{dy}{dt} = c_{gy}$ for a given constant k and l that is evaluated at each time step. Rossby

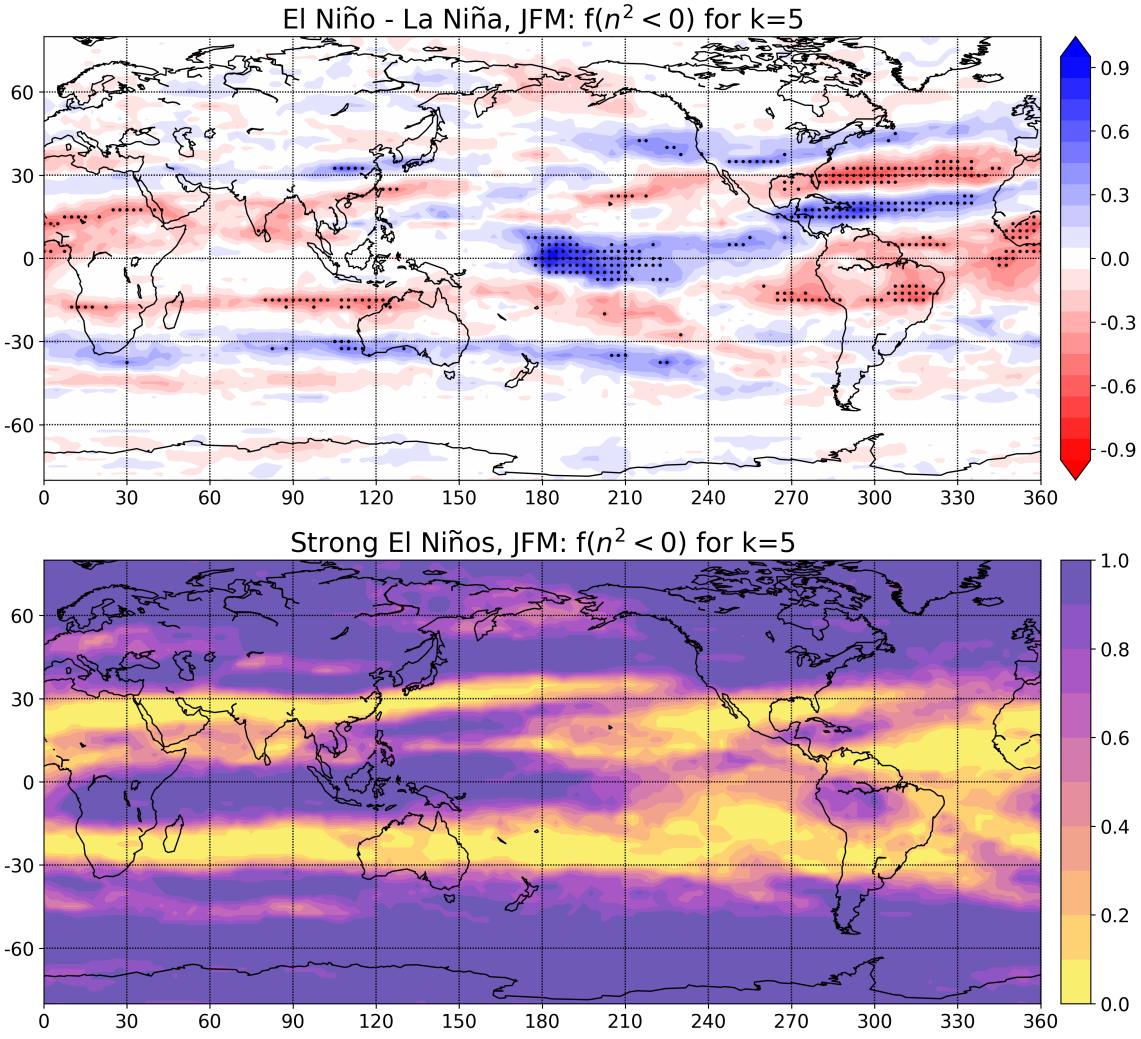

Figure 5.6: Spatial distribution of the frequency of negative refractive index for zonal wavenumber 5. a) Difference between top 10 El Niño vs La Niña years in January-March. Stippling indicates significance at 95% confidence. Negative values (shaded red) correspond to wavenumber 5 activity favored during El Niño, whereas positive values (shaded blue) indicate wave activity favored during La Niña. b) Composite of the frequency of negative refractive index during strong El Niños (1958, 1973, 1983, 1992, 1998) for January-March. Low values, near zero, correspond with conditions that nearly always sustain wavenumber 5 activity. High values, near one, correspond with conditions that nearly never sustain wavenumber 5 activity. Regions with values near 0.5 indicate variability within the climatology.

wave activity generated or reinvigorated over East Asia and the West Pacific baroclinic zone travels eastward in the mid-latitude wave guide, and splits near 210^oE, with shorter waves turning equatorward into the subtropics (Fig. 5.7b). Wave sources in the tropics result in planetary-scale wave activity tracking poleward across the eastern Pacific into Canada (Fig. 5.7c; low wavenumber, yellow and orange lines). Synoptic-scale wave activity meanwhile gets channeled within the subtropical wave guide (Fig. 5.7c; high wavenumber, red and purple lines), merging with wave activity from the mid-latitudes into Mexico. It is the nature of the mid-latitude wave guide and subtropical wave guide, and the merger of the two in the eastern Pacific as described in Wirth et al. (2018), that is key in producing a favorable environment for long-lasting groups of high-amplitude Rossby waves known as Rossby wave packets (RWPs). The role of RWPs in the extreme weather events in 2016 will be discussed in the next section.

5.3 Rossby Wave Activity

During the winter of 2015-16, there were two extended periods of elevated Rossby wave activity with multiple RWPs circling the northern hemisphere mid-latitudes. The first period, while not a focus of this study, is briefly described to introduce the role of RWPs in high-impact events this winter. This period featured a RWP tracking from the Pacific across the western hemisphere, during mid-December through early January. The RWP was responsible for the amplification of ridging over the Northeast US in late December, causing record breaking warmth. A downstream trough amplified over the North Atlantic, subsequently breaking cyclonically poleward and the wave train culminated in a highly anomalous anticyclone over the Kara Sea by the first week of January. The amplification of this high latitude ridging resulted in a breakdown of the tropospheric polar vortex, manifested in the Arctic Oscillation (AO) tumbling from a daily record high over +4 sigma in the third week of December to -4 sigma by mid-January. Record warmth flooded the Arctic in association with this ridge (Cullather et al. 2016). Meanwhile the negative annular mode

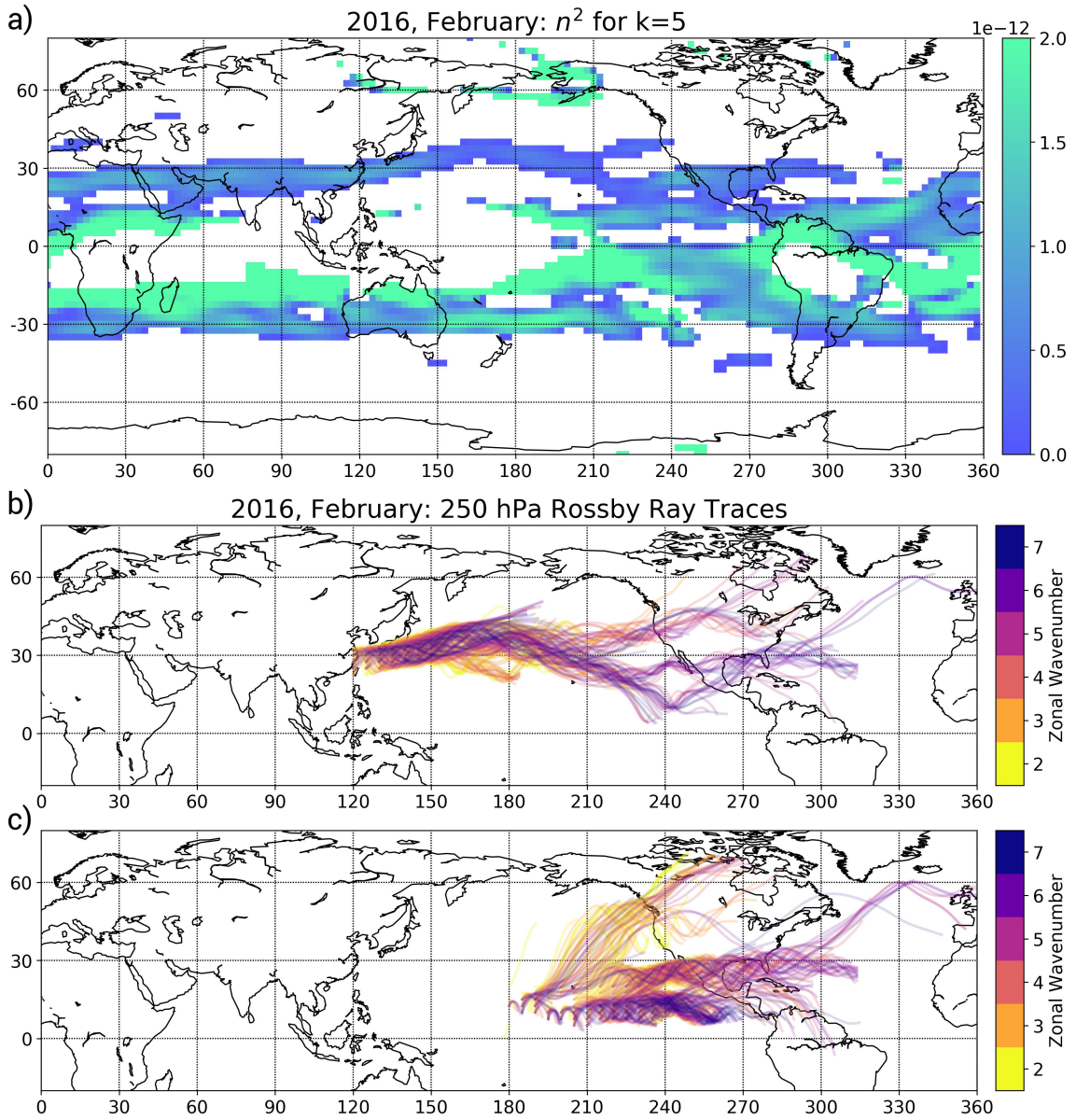

Figure 5.7: Basic state analysis for preferred Rossby wave activity propagation in February 2016, using the average 250 hPa winds for the month. a) Refractive index for zonal wavenumber 5. b) Rossby ray traces integrated forward every 60 seconds for 5 days following the equations of Hoskins and Karoly (1981), for zonal wavenumbers 2 through 7 as indicated by their color. Rays are initialized from a matrix of points every 2.5^o latitude and 5^o longitude in the mid-latitude western Pacific. c) Same as (b), but for rays initialized in the tropical Pacific.

preceded a crippling blizzard in the Mid Atlantic US on 22-24 January. Widespread one to three feet of snow and blizzard conditions paralyzed travel, knocked out power to more than half a million people, and resulted in 55 fatalities (Uccellini 2016).

The second period of elevated Rossby wave activity featured two RWPs circling the mid-latitude northern hemisphere concurrently from the end of January through the first half of March. The two RWPs were the catalysts for multiple high impact weather events through February and March (Fig. 5.5a), including a tornado outbreak in the Southeast US on 23-24 February. A total of 65 tornadoes were reported over the two days, resulting in 7 fatalities (SPC tornado database; Schaefer and Edwards 1999). The same RWP maintained coherence while circling the globe once more through the first week of March, reaching the eastern Pacific and North America by 7 March.

At this point in March, a Madden-Julian Oscillation (MJO) wave propagating into the western hemisphere combined with low-frequency ENSO forcing to enhance the anomalous tropical convection over the eastern Pacific (Blunden and Arndt 2016). The seasonal and sub-seasonal forcing drove broad twin anticyclones on either side of the equator. The extratropical RWP re-energized (Fig. 5.5b) as it reached the Pacific wave guide (Fig. 5.7). The RWP continued into the western hemisphere and turned southeastward as illustrated by the positive (southwest to northeast) tilt of the trough axis in Fig. 5.5b, consistent with the pathway defined by the ray traces in Fig. 5.7b. As the RWP moved downstream, it constructively interfered with the large-scale anticyclone in the subtropical North Pacific, resulting in both amplification and shortening of the wavelength of the ridge. Subsequent anticyclonic wave breaking toward Mexico accompanied the passage of the RWP downstream. On the northeast edge of the ridge, air dragged from the cyclonic shear side of the jet carved a trough along the US West Coast toward Baja California (Fig. 5.5b).

With an upper level ridge anchored over the eastern Pacific in association with tropical forcing, and the RWP turning equatorward toward Mexico between 8 and 10 March (Fig. 5.5b), the downstream trough continued amplifying southward. By 10 March, this trough

had cut off over central Mexico with geopotential heights in the center of the 500 hPa low below 5600 meters. The anomaly extremum, centered near $20^oN/103^oW$, dipped to around 9 standard deviations below average (Fig. 5.1a). The depth of this low far exceeded the previous all-time record 500 hPa height minimum over central Mexico in NCEP/NCAR reanalysis (Fig. 5.1b). The RWP continued eastward, amplifying a ridge downstream over the eastern US.

These RWPs can be diagnosed using the wave activity flux (WAF) from Takaya and Nakamura (2001c) as demonstrated in Wolf and Wirth (2017). We take this approach to qualitatively examine propagation of the RWP in the beginning of March (Fig. 5.5b). To quantitatively assess the aggregate measure of RWP frequency and magnitude during this period of time and past years, the WAF for stationary eddies (Takaya and Nakamura 1997) is evaluated where the background winds are westerly and averaged over a 30-day moving window, and then averaged spatially across the mid-latitude Pacific and the northern hemisphere. These measures were among the highest on record observed during this period according to the climatology calculated from the NCAR/NCEP reanalysis from 1950 to 2016 (Fig. 5.8). Past strong El Niños (Fig. 5.8a,b, red lines) exhibited above normal magnitudes of WAF in the northern hemisphere and Pacific in October, which 2016 mimicked. Moving into December, these years regress toward the middle of the climatological envelope (Fig. 5.8a,b, gray lines). Decreasing wave activity in January and early February is noted in the overall climatology, which is consistent with mid-winter suppression in the amplitude of baroclinic waves (**?**). The strong Niño years tended to exhibit an even more pronounced minimum in the North Pacific (Fig. 5.8b), which was then followed by consistently below normal WAF in the latter half of winter. In stark contrast, the mid-winter suppression in 2016 was cut short and replaced with a period of wave activity at record high levels in the northern hemisphere (Fig. 5.8a, blue line) and near records over the Pacific (Fig. 5.8b, blue line). Average WAF over the Pacific was around 50% higher than any of

the strong Niño cases. None of these past cases featured any exceptional levels of WAF in the latter half of winter comparable to February 2016.

5.4 Predictability

While the overall performance of numerical weather prediction is improving (e.g., Thorpe 2004, Shapiro et al. 2010), the ability to accurately predict individual extreme events is of highest consequence. This skill in predicting extremes is a concern not only because of the anomalous nature of the atmosphere at that time, but also the increased importance of the forecast to the public. Rossby wave packets have been shown to be a key to both high impact weather events (Shapiro and Thorpe 2004; Wirth and Eichhorn 2014), as well as influence on medium to long range predictability (Grazzini and Vitart 2015). For the three-month period from January through March, both the GFS and ECMWF had its best performance during the month of February (Fig. 5.9), coinciding with the time of the elevated RWP activity. In March, elevated forecast skill (Fig. 5.9) occurs during the passage of the strong RWP responsible for the Mexico trough (Fig. 5.5a), whereas weaker RWPs crossing the Pacific around 1 March and again around 15 March (Fig. 5.5a) are associated with reduced forecast skill, especially by the middle of the month.

The coherence of the wave train across the Pacific is a key factor in the forecast around the mid-latitude northern hemisphere during this period. The ensemble mean and spread for the meridional wind at 250 hPa are shown in Fig. 5.10 for NOAA's Global Ensemble Forecast System (GEFS) and the ECMWF Ensemble Prediction System (EPS) for lead times up to 10 days. These forecast systems show striking skill in predicting aspects of the RWP even at the 10-day lead time. For example, the trough over Mexico is consistently evident in both the GEFS and EPS along with a downstream ridge over the eastern U.S. and a trough over the western Atlantic. Both ensemble means depict a strong trough over Mexico between day-8 and day-10 (bottom of Fig. 5.10), and already imply a potentially extreme event (Fig. 5.11). In addition, seasonal ensemble systems depicted the trough beyond 10

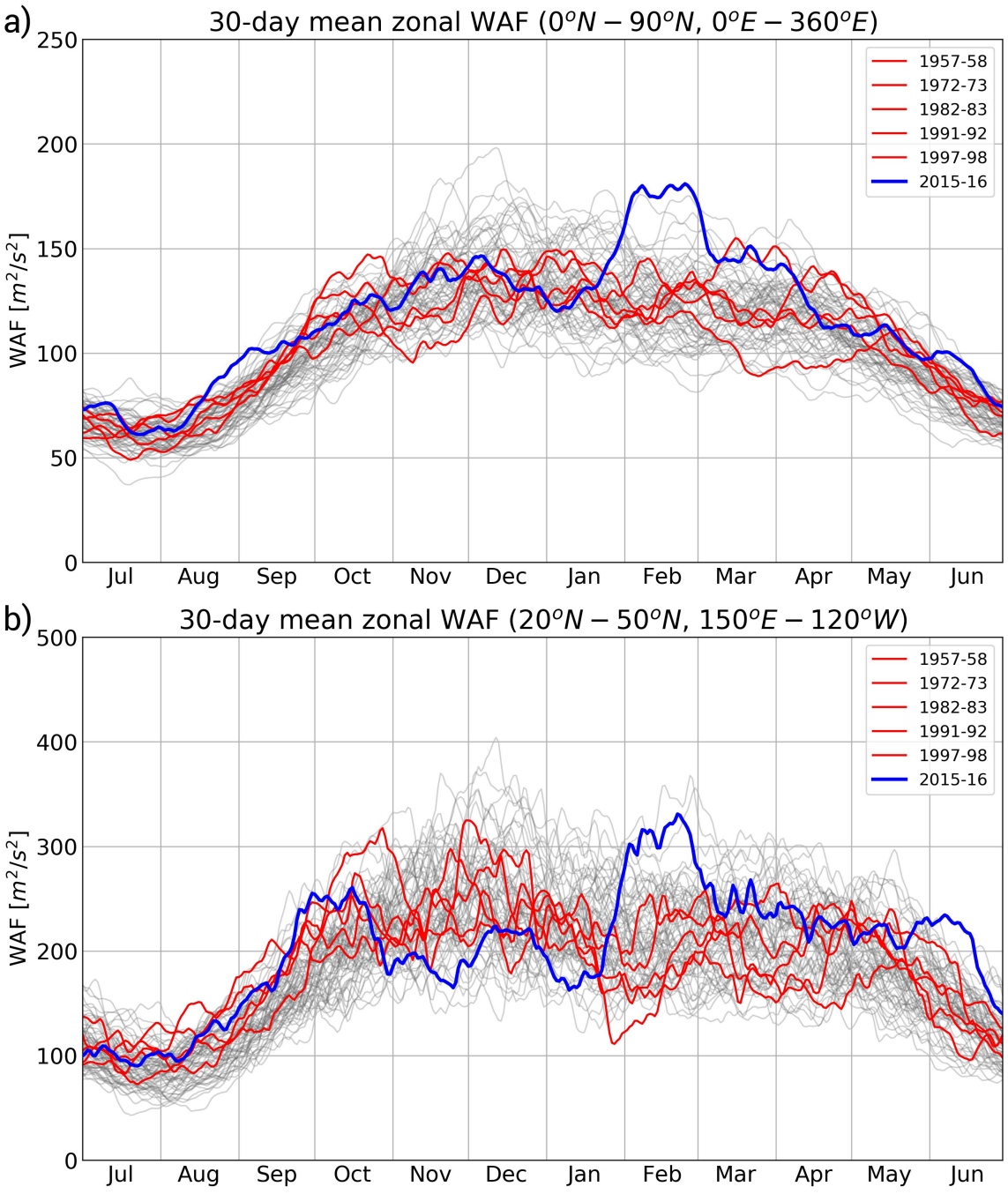

Figure 5.8: 30-day running-mean zonal component of wave activity flux at 250 hPa averaged over (a) the northern hemisphere, and (b) the mid-latitude North Pacific ($20^oN - 50^oN$, $150^oE - 120^oW$) calculated from daily NCEP/NCAR Reanalysis. Each year is plotted in gray (from 1 July to 30 June) from 1950 through 2016. Strong El Niños in January-March (1958, 1973, 1983, 1992, 1998) are plotted in red. 2015-16 is plotted in blue.

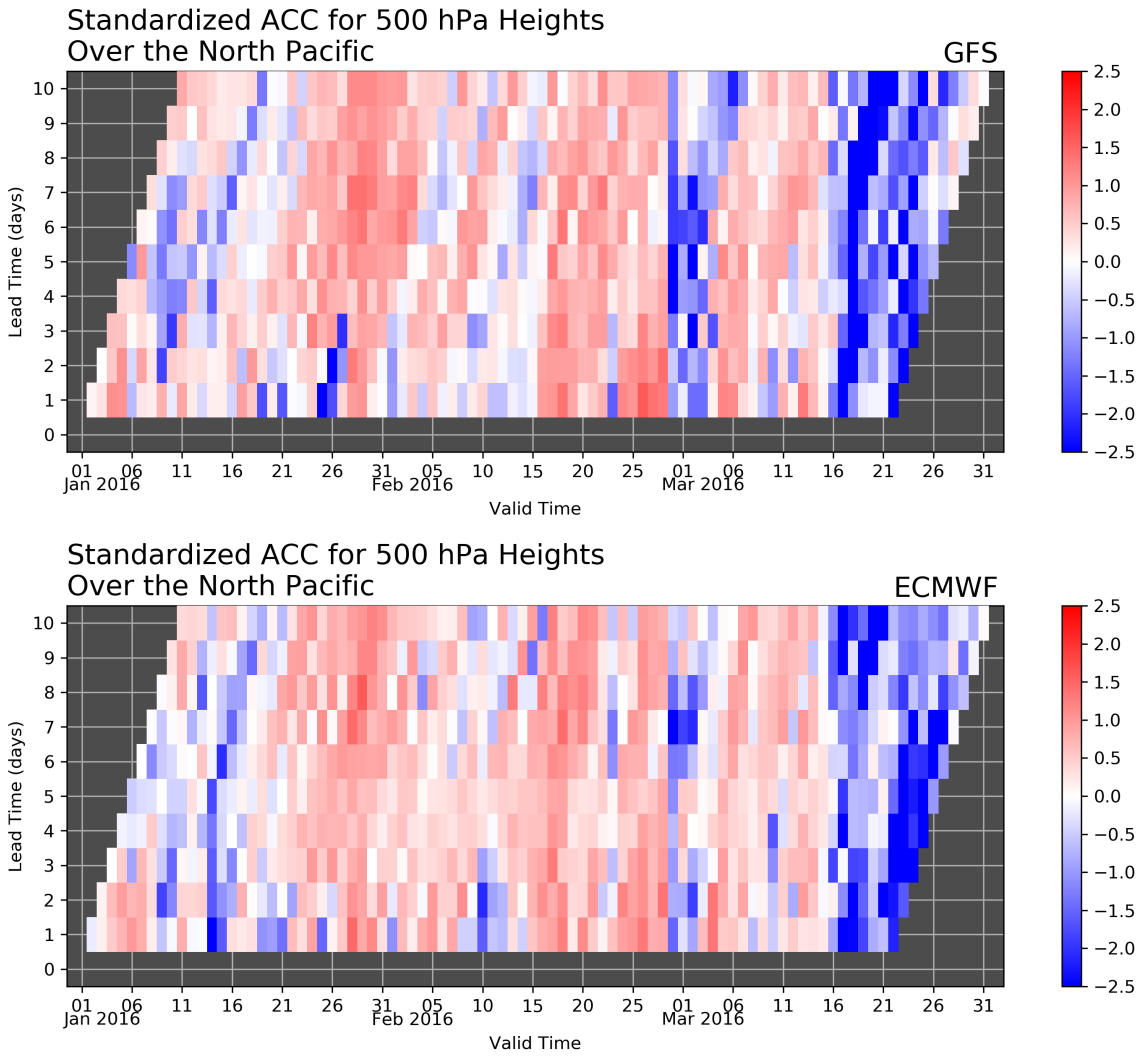

Figure 5.9: GFS (top) and ECMWF (bottom) 500 hPa height anomaly correlation coefficient (ACC) over the North Pacific ($10^oN - 60^oN$, $120^oE - 270^oW$), standardized by lead-time against the average and standard deviation of ACC during the 3-month period. Positive (negative) values indicate a forecast performance that is better (worse) than the 3-month average for the given lead-time.

days as well (not shown). This skill in capturing the general pattern as shown in Fig. 5.10 is in agreement with a study from Grazzini and Vitart (2015) indicating increased predictability is associated with long-lived RWPs. However, there is still uncertainty contained within the medium-range forecast. The ensemble spread of the meridional wind shown by the contours in Fig. 5.10 is maximized between the northerly and southerly phases of the wave over North America (e.g., see EPS between 96 and 240 hours). This placement indicates differences in the phase location of the troughs and ridges within the RWP. All waves are amplified within an RWP regardless of phase. If two sets of waves, such as a forecast and an analysis, within the same RWP have phase differences, errors from those differences will also amplify within the packet.

After recognition of the existence of the trough, the next question is its amplitude. We hypothesize that the depth of the trough over Mexico is tied to the intensity of the RWP moving across the Pacific. Using both the GEFS and EPS ensembles, we investigate the significance of this link by the sensitivity of the 500 hPa trough to 250 hPa winds. The depth of the trough is given by the negative of 500 hPa heights (such that a higher number indicates a deeper trough) in the central Mexico domain outlined in Fig. 5.1a. The sensitivity of the trough to the RWP is represented by the correlation of 250 hPa meridional wind at each grid point to the negative of 500 hPa heights over central Mexico, across the members of the ensemble (Fig. 5.12). The GEFS in particular demonstrates strong dependence of the Mexico trough on the upstream RWP as indicated by the train of significant correlation of alternating signs across the Pacific. In both the EPS and GEFS, positive correlations over Mexico are shifted west from the ensemble mean southerlies downstream of the trough. These phase-shifted correlations suggest a sensitivity of the depth of the trough to both the longitude of the trough axis, as well as its half-wavelength. Following the positions of correlation extrema in Fig. 5.12, ensemble members with the lowest geopotential heights over Mexico were a product of a shorter wavelength trough, as indicated by less distance between the correlation extrema than between the ensemble mean wind extrema. The same

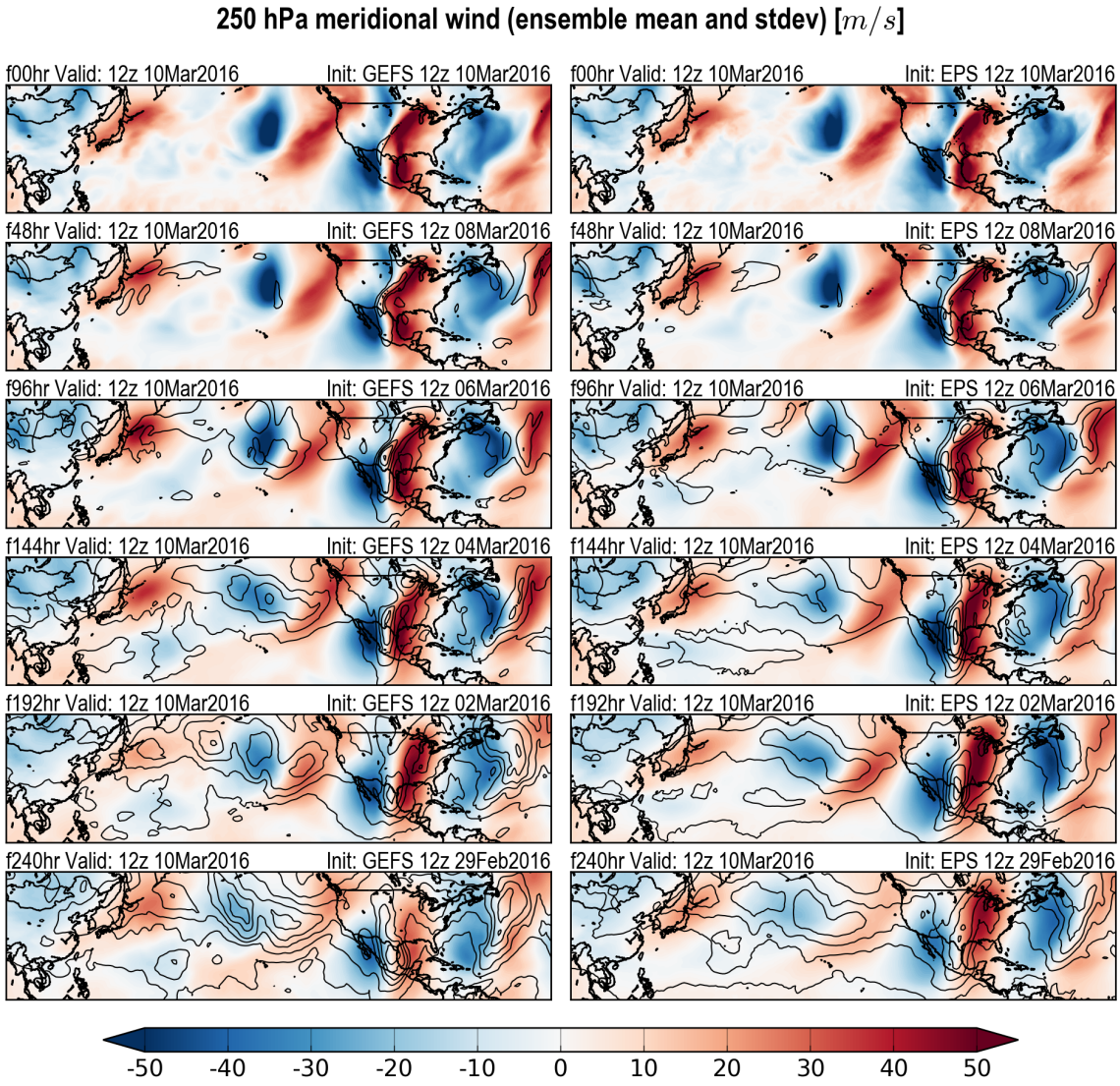

Figure 5.10: Ensemble mean (fill) and spread (contoured every 5 m/s) of 250 hPa meridional wind forecasts from the GEFS (left) and EPS (right) for 12z 10 March 2016. Lead-time starts at 0 hours at the top, and incrementally increases by 48 hours, to 240 hours at the bottom.

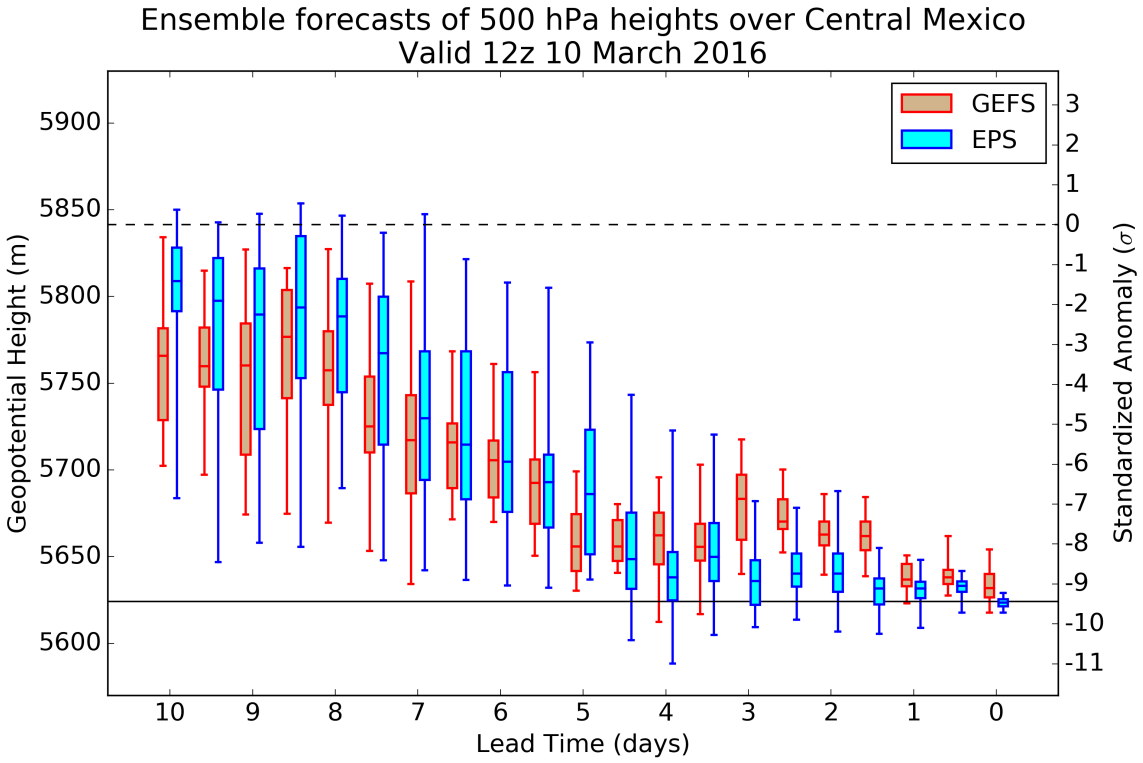

Figure 5.11: Ensemble forecasts from GEFS (red) and EPS (blue) for 500 hPa heights over central Mexico valid 12z 10 March 2016. The boxes indicate the 25th to 75th percentile range, and the whiskers indicate the full range. The horizontal dashed line indicates the climatology from ERA-Interim and the solid line indicates the 12z 10 March 2016 verification from ERA-Interim.

comparison also indicates the members with a deeper trough anchored the trough further west and closer to the eastern Pacific subtropical ridge. The sensitivity to phase is also important given that the greatest ensemble spread was associated with the phase of synoptic features across the Pacific (Fig. 5.10).

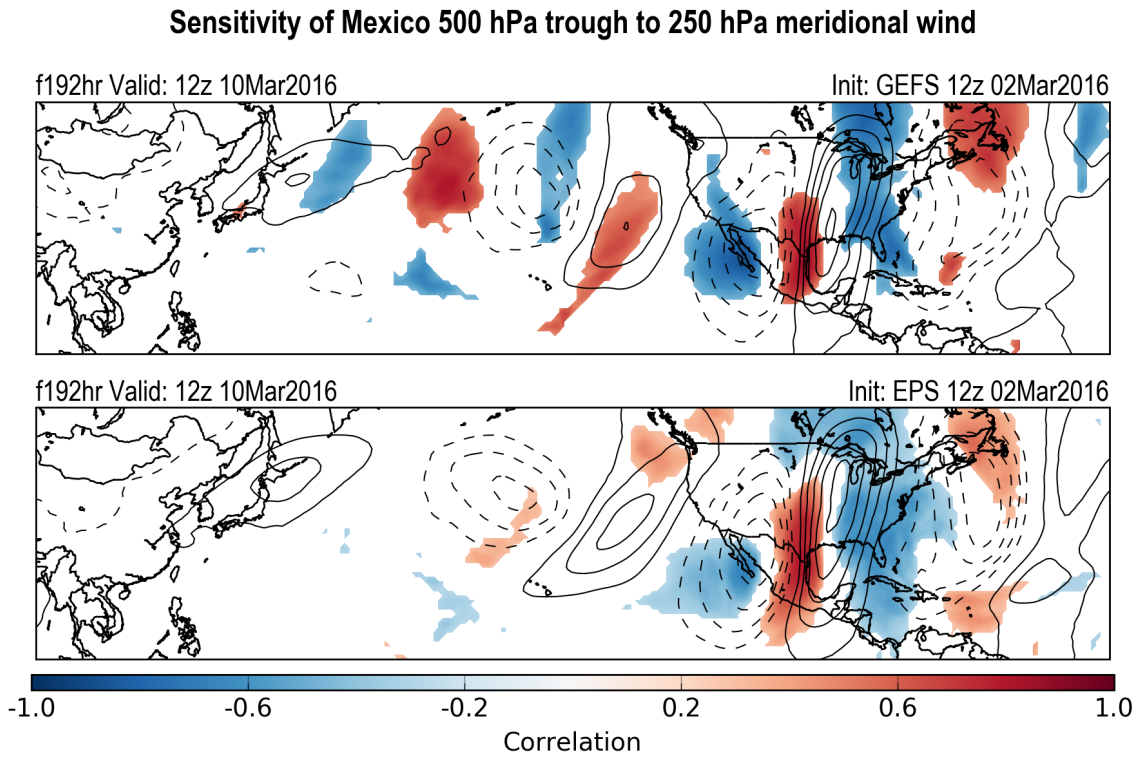

Figure 5.12: Ensemble sensitivity for the depth of the 500 hPa trough (negative of geopotential height) over central Mexico to 250 hPa meridional winds in the day-8 forecast from GEFS (top) and EPS (bottom). The correlation at each gridpoint is given by the color fill, with only the values above the 95% confidence threshold plotted. Ensemble mean forecast 250 hPa meridional winds are contoured every 5 m/s, excluding the zero wind line.

In order to directly and quantitatively evaluate the handling of the RWP in the models, we use the zonal component of WAF area-averaged across the mid-latitude Pacific domain. Figure 5.13 depicts the inter-quartile range (IQR), defined as the range between the 25th and 75th percentiles, of the GEFS forecast area-averaged WAF as a function of lead-time. The passage of RWPs is represented by the sinusoidal rise and fall in the averaged WAF. At

10-day lead-time, the IQR is successful at capturing the verified WAF during the passage of the RWP between 7 and 10 March (Fig. 5.13). However, in the medium-range forecast, spread decreases substantially as indicated by the length of the bars shrinking at subsequent lead times. While the medium-range GEFS appropriately recognizes the passage of the RWP in early March, the amplitude is significantly underdone. At only 3-day lead-time, the amplitude of the RWP in the GEFS mean is about 25% lower than the analysis.

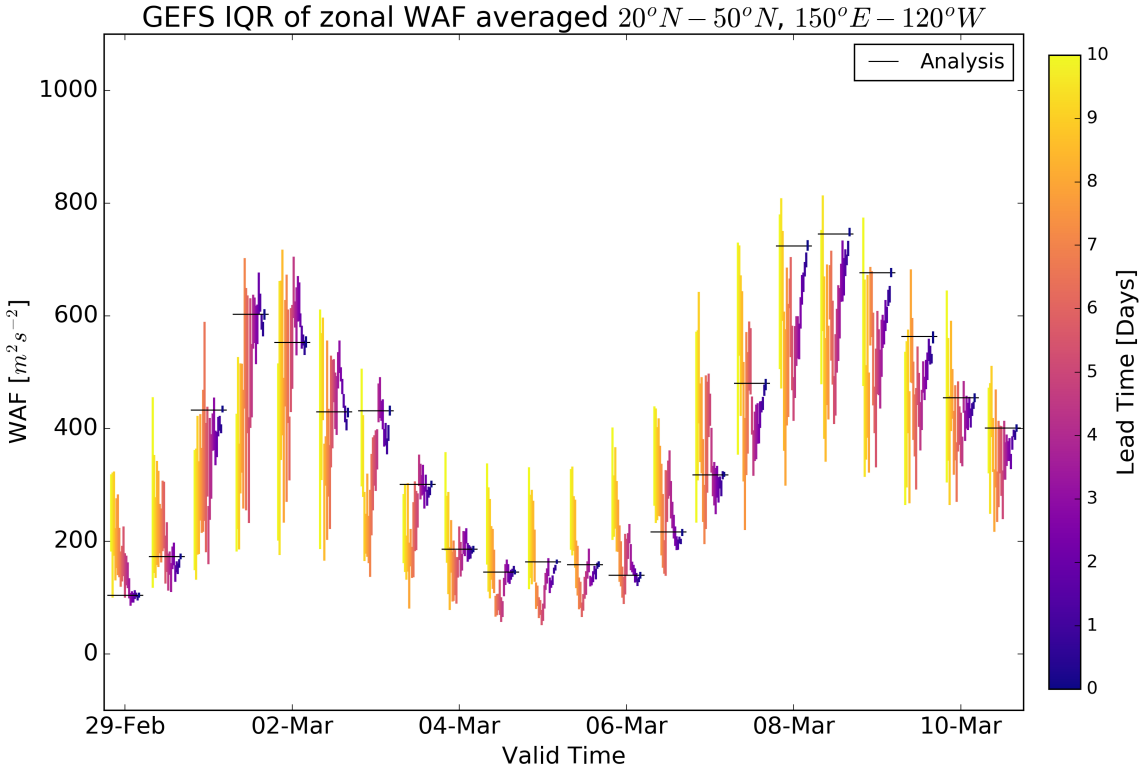

Figure 5.13: GFS ensemble IQR of zonal WAF averaged over the mid-latitude North Pacific (20^oN-50^oN, 150^oE-120^oW). End points of each vertical line indicate the 25th and 75th percentiles of the ensemble forecast. Color indicates the lead time of the forecast. Black horizontal lines indicate the analysis.

As a result of the relatively weaker modeled RWP (Fig. 5.13), the GEFS forecasts of 500 hPa heights over central Mexico indicate a trough that is less amplified than the

verification and exhibit less spread at day-6 to day-2 lead-time (Fig. 5.11). We see that the ensemble systems captured the existence of a trough over Mexico at day-8 to day-10 lead time (Fig. 5.10), with the IQR of geopotential heights extending to around 4 standard deviations below normal in both forecast systems (Fig. 5.11). The GEFS forecast lower heights than the EPS from day-10 to day-5. Despite the consensus for a trough, the depth and equatorward extent of the trough do not begin to be captured until day-5 for the GEFS, and day-4.5 for the EPS. The EPS tends to lag the GEFS by 12 hours in trends, though by day-4 consistently forecast lower heights than the GEFS for the remainder of forecast runs (Fig. 5.11). In summary, the expectation of an extreme event for central Mexico had approximately five days of lead time.

5.5 Summary

The winter of 2015-2016 will be known for many things, including one of the strongest El Niños in recorded history. Additionally, it will be known for unexpected El Niño behavior. For example, the much-needed plentiful rainfalls projected by seasonal forecasts did not occur over California and Baja California (Fig. 5.3d). In addition, the typical low-frequency mid-latitude pattern emanating from tropical convection associated with a strong El Niño, was absent. In its place was an active wave guide with short wavelength, high amplitude troughs and ridges around the mid-latitude northern hemisphere, including a period of record-level wave activity flux. A product of the active wave guide was a record breaking trough that impacted Mexico with a wide variety of detrimental societal, economic, and environmental impacts. This study demonstrates the important role of the nature of the jet streams over the Pacific in regulating the response of the atmosphere to tropical convection. In this case, the extreme event over Mexico was not associated with a typical cold air outbreak moving from Canada to Mexico along the lee of the Rockies, as in past studies (e.g., Colle and Mass 1995; Magaña et al. 2003; Henry 1979; Reding 1992; Schultz et al. 1997;

Pérez et al. 2014), but instead resulted from an interaction between tropical convection and a middle latitude RWP both injecting Rossby wave activity into the subtropical jet.

We can gain insight into the influence of the overall structure of the atmosphere as a refractive medium for Rossby wave activity, including fast narrow jet streams acting as wave guides. El Niño tropical convection did not play its typical role in California during this period, extending the historic drought. The combination of differences in tropical convection between El Niño years, and the differences in the nature of the wave guides, means a quite different response can occur over North America. However, the situation is not so simple as differences in seasonal and sub-seasonal tropical convection affecting the nature of the jet streams. The structure of the entire environmental PV field will be molded by other external conditions like subtropical and mid-latitude SSTs, winds in the stratosphere, and internal dynamics in the angular momentum budget such as mountain and friction torque and eddy fluxes (e.g. Li and Wu 2010). In the case of the 2015-16 winter, we identify the unusually warm water outside of the ENSO region as one possible factor impacting the structure of PV and path of Rossby wave activity, persuading observed sensible weather to diverge from past strong El Niños, consistent with Quan et al. (2018). Recent studies utilizing ensembles of climate model simulations by Deser et al. (2017) and Deser et al. (2018) demonstrate the variability in sensible weather that is possible in ENSO events. Our study reinforces this idea and elaborates on the pivotal role of the shape and characteristics of the wave guides in the Pacific in determining the downstream response to tropical convection over North America.

With the presence of a well-defined wave guide, the antecedent condition of long-lived RWPs coincided with increased forecast skill, consistent with studies on relationships between RWPs and intrinsic predictability (Grazzini and Vitart 2015). The RWP also acted to amplify and shorten low-frequency waves which are typically easier to predict given persistence. Therefore, proper handling of these features allowed for the Mexico trough to be captured by medium-range NWP out to 10 days, along with signals at even longer

lead-time within sub-seasonal ensembles. While the existence of the RWP was properly modeled, NWP struggled to capture the strength of the RWP. The amplitude of the trough is shown to be dependent on the strength of the RWP itself. Ramifications of these discrepancies go beyond just the amplitude of the waves, including also wavelength, phase speed, and the timing of wave breaking. Consistent with this idea was maximum ensemble spread around wave nodes, indicating phase uncertainty. The spread associated with phase uncertainty is amplified by the RWP, making the wave packet a potential forecast skill liability.

The historic winter storm that impacted Mexico in March 2016 demonstrates the importance of our understanding of Rossby wave dynamics across all scales, and acknowledgement of variability beyond the canonical pictures of ENSO. This event, and the unique El Niño winter that facilitated it, should be a highlighted case in the endeavor to both (1) extend our limits of predictability for extreme high impact weather, and (2) improve our skill at sub-seasonal and seasonal timescales.

Chapter 6

Summary and Discussion

While the overall skill of medium-range numerical weather prediction steadily improves, two important challenges emerge: understanding, anticipating, and mitigating forecast dropouts or busts; and the predictability of extreme high-impact weather events. Our work to address both of these challenges begins with a framework of Rossby wave diagnostics.

6.1 Error Growth and Forecast Busts

This dissertation takes advantage of both PV diagnostics and the framework of Rossby wave activity flux and ray tracing to analyze the life cycle of upscale error growth in NWP. Starting with the potential vorticity equation, we derived an original equation for potential vorticity error tendency that removes non-linear error-interaction terms. From this equation, we were able to fit the kinematic error terms into the same phase-independent wave activity flux formulation as Takaya and Nakamura (2001b), allowing for migratory waves on a zonally-varying base state. Two new diagnostics were born from this process: a phase-independent error amplitude, and a error wave activity flux. These diagnostics were then applied to ten years of ECMWF forecasts. We found seasonal differences in the geographical distribution of errors and then focused on the late spring and early summer based on the findings from Rodwell et al. (2013) that central United States convection was responsible for initial error growth in bust cases.

Composite averages across the northern hemisphere show that near-tropopause rotational errors develop preferentially first over the central and eastern United States within the first two days in all forecasts. A second area of early error growth is seen near Japan. Both these regions of error extend eastward in their respective downstream waveguides. By day-4, errors begin expanding equatorward and poleward. The composites highlight

problem areas in all forecasts. The next question is where errors of consequence grow in bust cases, and how we might distinguish these cases from good forecasts. Composite difference plots compared the worst 10 percent of day-6 forecasts over Europe to the best 10 percent, and found no significance in the first 2 days. It is not until day-3 lead time that significant differences appear, with larger errors in bust cases over the northern Atlantic. This area of significant error expands downstream into the the northeast Atlantic and Europe during days 4 through 6. The important finding is that while the initial errors are largest on average over the central and eastern United States, their amplitude does not demarcate whether a bust will occur later in the forecast. Not until errors reach the Atlantic waveguide is there a systematic bifurcation in the skill of the forecast.

These results suggest that medium-range forecast performance is not distinguished by errors in the early stages of the forecast, but rather by the sensitivity of the downstream environment. There is a fairly rich history of work on error growth in model systems, sensitivity to small errors, and general limits to predictability. In addition, there is a growing body of literature on practical error growth for given regional cases. This dissertation is a study in the spatial and temporal variability of intrinsic predictability. The study begins with the investigation of the medium-range bust forecasts described above, and then applies the full suite of developed diagnostic tools to the evolution of the atmosphere in June 2015. This period of time coincided with the PECAN (Plains Elevated Convection at Night) field campaign and also included multiple ECMWF medium-range forecast busts. A series of MCSs rolled across the US northern Plains, bringing a swath of damaging severe weather. Meanwhile, tropical storm Bill moved inland across the Southeast. The upper level diabatic outflow from these features provided multiple punches to the entrance of the Atlantic waveguide. Using a set of MPAS runs initialized at sequential times with Gaussian noise, we analyze the source of errors at different times in the forecast and how they evolve. This case study reaffirms the importance of divergent wind impinging on the sharp PV gradient over the northern Atlantic in the amplification and upscale growth of errors.

To place these findings within the context of past studies, Lillo and Parsons (2017) noted the role of the interaction between diabatic processes and the wave guide in forecast busts over Europe associated with regime change across the Arctic and middle latitudes. Several other studies (e.g., Grazzini and Isaksen 2002; Rodwell et al. 2013, Rodwell et al. 2018; Parsons et al. 2019a) have proposed that medium range forecast busts are associated with MCS activity over North America near the wave guide. Our investigation, however, found no statistically significant difference in errors early in the simulation over North America between poor versus good forecast simulations. Thus, the subsequent diabatic magnification of errors downstream over the North Atlantic plays a critical role in the occurrence of forecast busts as statistical differences were noted in error growth over the North Atlantic. Our systematic investigation of good vs. poor forecasts and our numerical experiments amplify recent investigations (e.g., Gray et al. 2014; Madonna et al.,Martínez-Alvarado et al. 2016, Grams et al. 2018, Baumgart et al. 2018, Baumgart et al. 2019) that highlight the importance of errors occurring when diabatic processes influencing the jet stream are poorly represented in the forecast model. Our systematic approach is an important step in illustrating the importance of these diabatic errors over the North Atlantic as many of the previously mentioned investigations relied of case studies.

To place these results within the context of temporal evolution of forecast error and predictability, there are three dimensions of time to consider (Fig. 6.1). The first, most frequently discussed and best understood dimension, is lead-time . For any two forecasts, or forecast and observations, or two evolutions of the atmosphere in which small differences are imposed, these differences will increase in scale and magnitude with increasing lead-time. The second is run-time, which refers to the initialization time of a given forecast simulation. Errors may grow differently from one run-time versus the next due to the assimilation of new data for initialization or due to the simulations diverging toward more sensitive and less sensitive regimes. While that divergence is itself of interest to us or any user, it also can provide information about the future evolution of each simulation and

confidence therein. The third and final dimension is valid-time. Note that these three dimensions are related, i.e. *valid-time* = *run-time* + *lead-time*. Consider a situation in which errors are only a function of valid-time. Error is thus independent of run-time and lead-time; only dependent on their summation to a given valid-time. The mechanism driving the error growth must be specifically a function of the instantaneous flow configuration. Of course this is unrealistic or else there would be simulation initializations sharing the same error magnitude as ten-day forecasts. The same can be said for error that is strictly a function of run-time. Error as a function of lead-time is how we examine the performance of NWP from a climatological perspective through bulk statistics. However, as is the motivation behind this dissertation, there is considerable variability in forecast performance at a given lead-time.

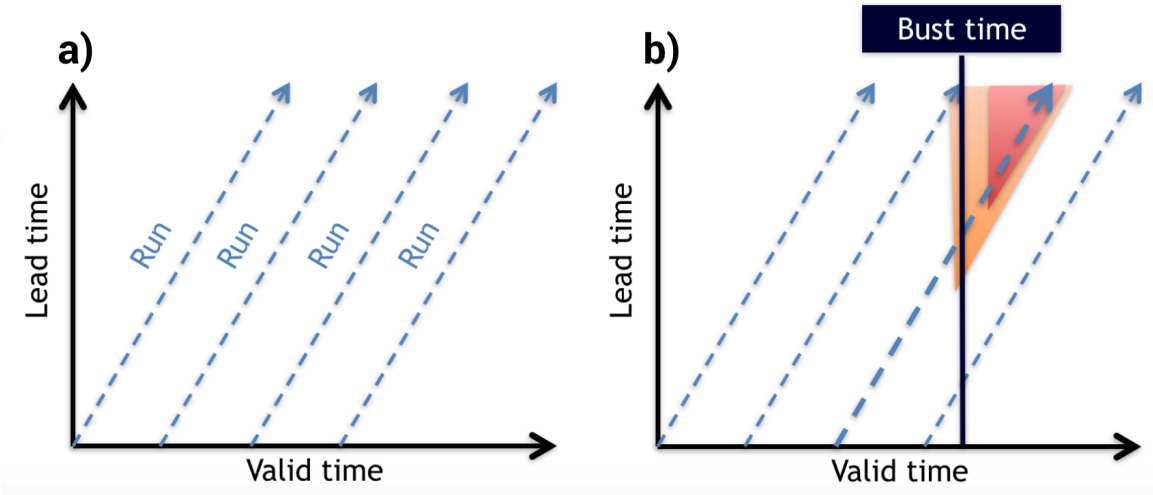

Figure 6.1: Lead-time chart schematic with valid time on the x-axis and lead-time on the y-axis, showing a) the structure of the chart with forecast runs on the diagonals, and b) the evolution of forecast error from the time of a forecast bust arising at a given valid time.

Studies on predictability horizons seek a lead-time at which error saturates at a particular scale and forecasts are no longer useful. This dissertation focuses instead on error and

uncertainty as a function of valid-time and run-time. Over the past decade, ensemble development has gained a significant role in NWP. Awareness, education, and increased utility of ensemble forecasts has followed. However, computational resources have dictated the limited size of and spatial resolution within ensemble systems Bauer et al. (2015).

6.2 Extreme Weather Events

Forecast busts are especially noticeable by the public when they coincide with high-impact sensible weather. Both busts and extreme weather events are facilitated by high-amplitude Rossby waves carried along on a waveguide. We return to the study by Grazzini and Vitart (2015) for some consolation that Rossby wave packets traveling along the long Pacific waveguide can increase intrinsic predictability downstream over North America. It follows that the synoptic-scale predictability of extreme weather events may in fact be higher than average. Our research interests in two recent extreme events resulted in two different foci of investigation: when Rossby wave packet behavior varies from the canonical response to interannual variability, and the sensitivity of sensible weather extremes to mesoscale perturbations.

In the first case, an historically deep trough over Mexico in March 2016 brought damaging winter weather far south across the country while also being responsible for devastating flooding rains in Louisiana. The storm occurred at the end of a winter which featured the strongest El Niño on record. Despite such a definitive base state, sensible weather chose to deviate strongly from canonical Niño relationships. For example, California was drier than normal, with much-needed rainfall staying to the north. The upstream flow pattern over the Pacific was characterized by a wider Hadley cell than would be expected with a strong Niño, and a mid-latitude waveguide that was frequently filled with wavenumber-6 and higher wave activity. In fact, during February wave activity grew to record levels; and much higher than during past Niño winters. Multiple high-impact weather events could be attributed to Rossby wave packets that were circling the globe, including an East Coast

heat wave, a blizzard, and a severe weather outbreak. The Mexico trough in March came at the end of a particularly strong Rossby wave packet. This RWP allowed for the extreme event to coincide with a period of overall high predictive skill over the North Pacific, which promptly decreased after the RWP activity subsided. The effect of the RWP was to amplify and shorten the wavelength of the low-frequency anomalous anticyclone over the eastern Pacific driven by El Niño forcing. Where models struggled was with the magnitude of the RWP, which trended stronger in the two days before the events. The outcome of the 2015-16 winter and our study of this extreme event emphasizes the importance of understanding the behavior of mid-latitude Rossby wave activity on multiple time scales. Synoptic wave activity is referred to sometimes dismissively as "internal variability", with the idea that it may be added linearly to a low-frequency base state without much change in the signal. However these interactions are not so simple, as is summarized in the Cross-cutting Themes section below.

The second extreme weather event we studied was a cold air outbreak that impacted the Midwest and Northeast at the end of January 2019. The antecedent large scale mid-latitude flow pattern was driven by MJO forcing moving across the Pacific and a significant stratospheric warming, which came together to produce ridging over western North America and into the Arctic. Downstream, the jet stream dived southward from northern Canada into the United States, which became a highway for a tropopause polar vortex to be ejected into the mid-latitudes. We investigated the importance of this TPV in the outcome of the cold air outbreak by running a set of simulations that perturb the initial strength of the TPV while over the Arctic. Our findings show that the cold air had a strong relationship to the strength of the TPV, with a stronger TPV resulting in colder temperatures and a more southward extent of the cold air. We also examined a climatology of TPV tracks and cold air outbreaks to establish the significance of a connection between the two. Our results show that TPVs exist 85 percent of the time within 1000 km of a CAO and that these TPVs tend to be higher amplitude, longer-lived and move further south than TPVs not associated with a

CAO. Thus while the large scale pattern can be conducive for below normal temperatures in the US, the location and severity of the cold is influenced by the characteristics of a mesoscale feature.

6.3 Cross-cutting Themes and broader implications

The primary focus on the bust problem is in the error evolution and amplification leading up to the time and location of the bust event. However the incipient error packet often has impacts on a larger scale following the bust. This characteristic is clearly evident in the Lillo and Parsons (2017) study showing that bust events were associated with different types of regime transition across both middle latitudes and the Arctic. Dynamically this result is consistent with errors in the treatment of mid-latitude Rossby waves, propagating and amplifying within the waveguide, and then breaking meridionally. Impingement of these error packets upon the Arctic, when they have already qualified as a bust in the mid-latitudes, coincide with timing of planetary-scale pattern changes and increased uncertainty therein. These dynamical regime shifts in the Arctic are likely to induce changes in TPV number, tracks, and bulk characteristics influence surface cyclone behavior, which impacts could influence Arctic sea ice.

Our investigation of the 11 April bust case of Rodwell et al. (2013) in Chapter 2 suggests that the flow associated with bust had error in wave activity flux near the exit region of the Atlantic wave guide propagating into the Arctic. In Chapter 3, the systematic investigation of the bust versus good forecasts also suggest that the location of the systematic error amplification occurs in the exit region of the Atlantic jet. In addition, the error amplitude in the investigation of the June 2015 bust in Chapter 3 also showed significant error propagating into the Arctic over the North Atlantic. In this exit region of the Atlantic waveguide, Rossby wave activity is dispersed meridionally associated with wave breaking (Michel and Rivière 2011). Following Lau and Holopainen (1984), the large scale response to forcing from transient eddies can be expressed as a combination of their momentum and

heat fluxes; the meridional and vertical components of wave activity flux respectively. The divergence of the meridional component of wave activity flux is equivalent to the northward flux of potential vorticity (Ren et al. 2011). This northward flux of potential vorticity and wavebreaking into the Arctic will affect TPV frequency and preferred tracks. Surface cyclone frequency and tracks are impacted accordingly. Momentum fluxes associated with wavebreaking feed back on the mid-latitude zonal flow (Lorenz and Hartmann 2003). Synoptic eddies interacting with the base state flow is a nonlinear process that accumulates over the span of days, and results in changes to the base state (Jin et al. 2006a,b; Ren et al. 2009). Heat fluxes associated with both poleward wavebreaking and surface cyclones, as well as the surface stress from cyclone winds, play a significant role in rapid sea ice loss events.

Our findings in the assessment of error growth in medium-range forecast busts and sources of predictability in extreme weather events highlights the need for understanding scale-interaction with Rossby wave activity and waveguides. The additions implications we have outlined in this section emphasizes the importance for all spatiotemporal scales and regions of the globe. One recent endeavor to improve our understanding of diabatic effects on the mid-latitude waveguide was a field campaign in the fall of 2016 called the North Atlantic Waveguide and Downstream Impact Experiment (NAWDEX; Schäfler et al. 2018). The aim was to sample disturbances interacting with the waveguide and associated downstream developing waves that result in high impact weather over Europe and in some cases reduced predictability. Included in the paper is a thorough overview of the importance of PV anomalies interacting with the waveguide, originating from diabatic processes within the warm conveyor belt of extratropical and transitioning cyclones, as well as TPVs migrating out of the arctic. The campaign occurred during a period in which the Atlantic jet was frequently disturbed. The constant wave activity, converging toward Europe, helped support a persistent blocking ridge over Scandinavia. This pattern also resulted in some complex wave evolutions over the Atlantic. Therein lies an issue with the initial analysis

of the cases during the campaign: compartmentalizing of each atmospheric evolution into upstream triggers, their dynamic interaction with the jet stream, subsequent development of disturbances, and downstream weather impacts. There is far more complexity that is necessary to address, especially when working with observations. But there is exceptional utility in these types of campaigns when coupled with operational NWP forecasts, and testing forecast sensitivity to the post factum assimilation of the new observations. One key concern mentioned in Schäfler et al. (2018) and highlighted in Parsons et al. (2019a) is the height of the divergent outflow layer relative to the jet stream. Whether it is an MCS over the US or a warm conveyor belt lifting over the North Atlantic, the dynamic interaction with the jet depends on the outflow layer reaching the jet level. In the cases discussed in Chapter 3, both continental MCS activity and downstream cyclogenesis over the North Atlantic played roles in introducing errors into the waveguide. The ability of data assimilation and NWP to properly resolve the divergence profile associated with these diabatic features is critical for the downstream forecast and up to the planetary scale at subsequent leadtimes, as discussed below.

Wave activity flux from the mid-latitudes to the Arctic influences distributions of heat and momentum, which can lead to large scale low-frequency pattern changes. These changes are typically associated with a bifurcation in the topology of atmospheric evolution, divided into a blocking mode versus a progressive mode. Pattern changes over the Arctic subsequently impact the mid-latitudes on subseasonal to seasonal (S2S) timescales (Jung et al. 2014; Zuo et al. 2016). Errors within the mid-latitude waveguide that infiltrate the higher latitudes can thus impact the low-frequency pattern, and result in greater error and uncertainty for S2S forecasts. The recent work by Woollings et al. (2018) notes the importance of an accurate representation of Rossby waves and atmospheric blocking to climate projections. The need for improved S2S and cliamte projections coupled with current short comings in the representation of the interaction between middle latitude Rossby waves and diabatic processes in state-of-the-art numerical weather prediction models is a

call for action for an increased research focus on the topics discussed in this dissertation. For example, the previous findings that NWP forecast busts are associated with an inability to predict regime changes across the Arctic and middle latitudes raises a clear concern for S2S and climate modeling. Another broader implication of our results that supports this idea is the importance of the interaction of the middle latitude wave guide and Rossby wave structure with tropical and Arctic systems in the production of extremes.

Since these errors highlight the importance of an accurate representation of diabatic processes, the improved treatment of these processes is a critical step forward. Currently operational global models are beginning to shift into horizontal resolution that is too small for parameterization schemes to produce the correct dynamical response while still too large to properly resolve convection. For example, the current resolution of the ECMWF model is 9km with experimental simulations at 5-km are being produced at 5-km to investigate these forecast busts. This representation of diabatic processes will also be a topic of interest as hybrid schemes are developed and machine learning gets more application in this arena. While deterministic models will move toward higher resolution, accurate representation of the interplay between diabatic processes and middle latitude Rossby waves will remain a challenge. Even as deterministic models move toward convective-resolving resolutions, ensembles will likely continue parameterizating convection, sacrificing horizontal resolution in order to maintain or increase ensemble size. Specific challenges may change, but the same limitations of upscale error growth remain. Interaction between large-scale pattern changes and mesoscale forcing upscale growth is a consistent source of forecast busts. As noted earlier (e.g., woollings2018blocking, the structure of Rossby waves and blocking is also an important topic for climate modeling.

Bibliography

Agee, E. M., and S. R. Gilbert, 1989: An aircraft investigation of mesoscale convection over lake michigan during the 10 january 1984 cold air outbreak. *Journal of the Atmospheric Sciences*, **46 (13)**, 1877–1897.

Andrews, D., and M. E. McIntyre, 1976: Planetary waves in horizontal and vertical shear: The generalized eliassen-palm relation and the mean zonal acceleration. *Journal of the Atmospheric Sciences*, **33 (11)**, 2031–2048.

Anthes, R. A., 1986: The general question of predictability. *Mesoscale Meteorology and Forecasting*, Springer, 636–656.

Archambault, H., and P. Harr, 2013: Recurving western north pacific tropical cyclones as precursors to high-latitude blocking. *AGU Fall Meeting Abstracts*.

Archambault, H. M., L. F. Bosart, D. Keyser, and J. M. Cordeira, 2013a: A Climatological Analysis of the Extratropical Flow Response to Recurving Western North Pacific Tropical Cyclones. *Monthly Weather Review*, **141 (7)**, 2325–2346, doi:10.1175/MWR-D-12-00257.1.

Archambault, H. M., L. F. Bosart, D. Keyser, and J. M. Cordeira, 2013b: A climatological analysis of the extratropical flow response to recurving western north pacific tropical cyclones. *Monthly weather review*, **141 (7)**, 2325–2346.

Archambault, H. M., D. Keyser, L. F. Bosart, C. A. Davis, and J. M. Cordeira, 2015: A composite perspective of the extratropical flow response to recurving western north pacific tropical cyclones. *Monthly Weather Review*, **143 (4)**, 1122–1141.

Bauer, P., A. Thorpe, and G. Brunet, 2015: The quiet revolution of numerical weather prediction. *Nature*, **525 (7567)**, 47–55.

Baumgart, M., P. Ghinassi, V. Wirth, T. Selz, G. C. Craig, and M. Riemer, 2019: Quantitative view on the processes governing the upscale error growth up to the planetary scale using a stochastic convection scheme. *Monthly Weather Review*, **147 (5)**, 1713–1731.

Baumgart, M., M. Riemer, V. Wirth, F. Teubler, and S. T. Lang, 2018: Potential vorticity dynamics of forecast errors: A quantitative case study. *Monthly Weather Review*, **146 (5)**, 1405–1425.

Bell, G. D., and M. S. Halpert, 1998: Climate assessment for 1997. *Bulletin of the American Meteorological Society*, **79 (5s)**, S1–S50.

Bengtsson, L., M. Ghil, and E. Källén, 1981: *Dynamic meteorology: data assimilation methods*, Vol. 330. Springer.

Berg, R., 2015: Tropical cyclone report, tropical storm bill, 16-18 june 2015. *Miami, FL: National Hurricane Center*.

Bierdel, L. B., 2017: On the relevance of rotational and divergent modes of motion to mesoscale dynamics and upscale error growth. Ph.D. thesis, lmu.

Biernat, K., L. Bosart, and D. Keyser, 2021: A climatological analysis of the linkages between tropopause polar vortices, cold pools, and cold air outbreaks over the central and eastern united states. *Monthly Weather Review*, **149 (8)**, 189–206.

Bjerknes, V., 1904: The problem of weather forecasting as a problem in mechanics and physics. *Meteorologische Zeitschrift*, **21**, 1–7.

Blackport, R., and J. A. Screen, 2020: Insignificant effect of arctic amplification on the amplitude of midlatitude atmospheric waves. *Science advances*, **6 (8)**, eaay2880.

Blunden, J., and D. S. Arndt, 2016: State of the climate in 2015. *Bulletin of the American Meteorological Society*, **97 (8)**, Si–S275.

Boer, G., 1994: Predictability regimes in atmospheric flow. *Monthly weather review*, **122 (10)**, 2285–2295.

Boer, G. J., and T. Shepherd, 1983: Large-scale two-dimensional turbulence in the atmosphere. *Journal of the Atmospheric Sciences*, **40 (1)**, 164–184.

Bosart, L. F., G. J. Hakim, K. R. Tyle, M. A. Bedrick, W. E. Bracken, M. J. Dickinson, and D. M. Schultz, 1996: Large-scale antecedent conditions associated with the 12–14 march 1993 cyclone ("superstorm'93") over eastern north america. *Monthly weather review*, **124 (9)**, 1865–1891.

Bosart, L. F., B. J. Moore, J. M. Cordeira, and H. M. Archambault, 2017: Interactions of north pacific tropical, midlatitude, and polar disturbances resulting in linked extreme weather events over north america in october 2007. *Monthly Weather Review*, **145 (4)**, 1245–1273.

Bougeault, P., and Coauthors, 2010: The thorpex interactive grand global ensemble. *Bulletin of the American Meteorological Society*, **91 (8)**, 1059–1072.

Bourke, W., 1972: An Efficient, One-Level, Primitive-Equation Spectral Model. *Monthly Weather Review*, **100 (9)**, 683–689, doi:10.1175/1520-0493(1972)100⟨0683:AEOPSM⟩2.3.CO;2.

Bourke, W., 1974: A Multi-Level Spectral Model. I. Formulation and Hemispheric Integrations. *Monthly Weather Review*, **102 (10)**, 687–701, doi:10.1175/1520-0493(1974)102⟨0687:AMLSMI⟩2.0.CO;2.

Boyle, J. S., and L. F. Bosart, 1983: A cyclone/anticyclone couplet over north america: An example of anticyclone evolution. *Monthly weather review*, **111 (5)**, 1025–1045.

Breaker, B. K., K. M. Watson, P. A. Ensminger, J. B. Storm, and C. E. Rose, 2016: Characterization of peak streamflows and flood inundation of selected areas in louisiana, texas, arkansas, and mississippi from flood of march 2016. Tech. rep., US Geological Survey.

Brower, L. P., E. H. Williams, P. Jaramillo-López, D. R. Kust, D. A. Slayback, and M. I. Ramírez, 2017: Butterfly mortality and salvage logging from the march 2016 storm in the monarch butterfly biosphere reserve in mexico. *American Entomologist*, **63 (3)**, 151–164.

Browning, K., A. Thorpe, A. Montani, D. Parsons, M. Griffiths, P. Panagi, and E. Dicks, 2000: Interactions of tropopause depressions with an ex–tropical cyclone and sensitivity of forecasts to analysis errors. *Monthly weather review*, **128 (8)**, 2734–2755.

Caballero, R., 2007: Role of eddies in the interannual variability of hadley cell strength. *Geophysical research letters*, **34 (22)**.

Caballero, R., and B. T. Anderson, 2009: Impact of midlatitude stationary waves on regional hadley cells and enso. *Geophysical Research Letters*, **36 (17)**.

Caplan, P. M., and G. H. White, 1989: Performance of the National Meteorological Center's Medium-Range Model. *Weather and Forecasting*, **4 (3)**, 391–400, doi: 10.1175/1520-0434(1989)004⟨0391:POTNMC⟩2.0.CO;2.

Cavallo, S. M., 2009: The structure and maintenance of tropopause polar vortices over the {Arctic}. Ph.D. thesis, University of Washington.

Cavallo, S. M., and G. J. Hakim, 2005: Life cycles of tropopause polar vortices, Cambridge, MA. American Meteorological Society 15th Conference on Atmospheric and Oceanic Fluid Dynamics.

Cavallo, S. M., and G. J. Hakim, 2009: Potential vorticity diagnosis of a tropopause polar cyclone. *Monthly Weather Review*, **137 (4)**, 1358–1371.

Cavallo, S. M., and G. J. Hakim, 2010a: Composite structure of tropopause polar cyclones. *Monthly Weather Review*, **138 (10)**, 3840–3857.

Cavallo, S. M., and G. J. Hakim, 2010b: The composite structure of tropopause polar cyclones from a mesoscale model. **138 (10)**, 3840–3857, doi:10.1175/2010MWR3371.1.

Cavallo, S. M., and G. J. Hakim, 2012: Radiative impact on tropopause polar vortices over the arctic. *Monthly Weather Review*, **140 (5)**, 1683–1702.

Cavallo, S. M., and G. J. Hakim, 2013: Physical mechanisms of tropopause polar vortex intensity change. *Journal of the Atmospheric Sciences*, **70 (11)**, 3359–3373.

Cellitti, M. P., J. E. Walsh, R. M. Rauber, and D. H. Portis, 2006: Extreme cold air outbreaks over the united states, the polar vortex, and the large-scale circulation. *Journal of Geophysical Research: Atmospheres*, **111 (D2)**.

Chang, E. K., 2005: The impact of wave packets propagating across asia on pacific cyclone development. *Monthly weather review*, **133 (7)**, 1998–2015.

Charney, J. G., 1949: ON A PHYSICAL BASIS FOR NUMERICAL PREDICTION OF LARGE-SCALE MOTIONS IN THE ATMOSPHERE. *Journal of Meteorology*, **6 (6)**, 372–385, doi:10.1175/1520-0469(1949)006⟨0372:OAPBFN⟩2.0.CO;2.

Charney, J. G., 1971: Geostrophic turbulence. *Journal of the Atmospheric Sciences*, **28 (6)**, 1087–1095.

Clarke, S. J., S. L. Gray, and N. M. Roberts, 2019a: Downstream influence of mesoscale convective systems. part 1: influence on forecast evolution. *Quarterly Journal of the Royal Meteorological Society*, **145 (724)**, 2933–2952.

Clarke, S. J., S. L. Gray, and N. M. Roberts, 2019b: Downstream influence of mesoscale convective systems. part 2: Influence on ensemble forecast skill and spread. *Quarterly Journal of the Royal Meteorological Society*, **145 (724)**, 2953–2972.

Colle, B. A., and C. F. Mass, 1995: The structure and evolution of cold surges east of the rocky mountains. *Monthly Weather Review*, **123 (9)**, 2577–2610.

Colucci, S. J., and J. C. Davenport, 1987: Rapid surface anticyclogenesis: Synoptic climatology and attendant large-scale circulation changes. *Monthly weather review*, **115 (4)**, 822–836.

Courtier, P., J.-N. Thépaut, and A. Hollingsworth, 1994: A strategy for operational implementation of 4d-var, using an incremental approach. *Quarterly Journal of the Royal Meteorological Society*, **120 (519)**, 1367–1387.

Cressman, G., and W. Hubert, 1957: A study of numerical forecasting errors. *Monthly Weather Review*, **85 (7)**, 235–242.

Cressman, G. P., 1963: *A three-level model suitable for daily numerical forecasting*. US Department of Commerce, Weather Bureau, National Meteorological Center.

Cullather, R. I., Y.-K. Lim, L. N. Boisvert, L. Brucker, J. N. Lee, and S. M. Nowicki, 2016: Analysis of the warmest arctic winter, 2015–2016. *Geophysical Research Letters*, **43 (20)**.

Curry, J., 1987: The contribution of radiative cooling to the formation of cold-core anticyclones. *Journal of the atmospheric sciences*, **44 (18)**, 2575–2592.

Curry, J. A., J. L. Schramm, W. B. Rossow, and D. Randall, 1996: Overview of arctic cloud and radiation characteristics. *Journal of Climate*, **9 (8)**, 1731–1764.

Daley, R., 1992: Estimating Model-Error Covariances for Application to Atmospheric Data Assimilation. *Monthly Weather Review*, **120 (8)**, 1735–1746, doi:10.1175/1520-0493(1992)120⟨1735:EMECFA⟩2.0.CO;2.

Davies, H. C., and M. Didone, 2013: Diagnosis and dynamics of forecast error growth. *Monthly weather review*, **141 (7)**, 2483–2501.

Dee, D. P., and Coauthors, 2011a: The era-interim reanalysis: Configuration and performance of the data assimilation system. *Quarterly Journal of the royal meteorological society*, **137 (656)**, 553–597.

Dee, D. P., and Coauthors, 2011b: The ERA-Interim reanalysis: configuration and performance of the data assimilation system. *Quarterly Journal of the Royal Meteorological Society*, **137 (656)**, 553–597, doi:10.1002/qj.828.

Deser, C., I. R. Simpson, K. A. McKinnon, and A. S. Phillips, 2017: The northern hemisphere extratropical atmospheric circulation response to enso: How well do we know it and how do we evaluate models accordingly? *Journal of Climate*, **30 (13)**, 5059–5082.

Deser, C., I. R. Simpson, A. S. Phillips, and K. A. McKinnon, 2018: How well do we know enso's climate impacts over north america, and how do we evaluate models accordingly? *Journal of Climate*, **(2018)**.

Dirren, S., M. Didone, and H. Davies, 2003: Diagnosis of "forecast-analysis" differences of a weather prediction system. *Geophysical research letters*, **30 (20)**.

Dole, R. M., and Coauthors, 2017: Advancing science and services during the 2015-16 el niño: The noaa el niño rapid response field campaign. *Bulletin of the American Meteorological Society*, **(2017)**.

Donahue, A. S., and P. M. Caldwell, 2018: Impact of physics parameterization ordering in a global atmosphere model. *Journal of Advances in Modeling Earth Systems*, **10 (2)**, 481–499.

Downton, M. W., and K. A. Miller, 1993: The freeze risk to florida citrus. part ii: Temperature variability and circulation patterns. *Journal of Climate*, **6 (2)**, 364–372.

Durran, D. R., and M. Gingrich, 2014: Atmospheric predictability: Why butterflies are not of practical importance. *Journal of the Atmospheric Sciences*, **71 (7)**, 2476–2488.

Evensen, G., 1994: Sequential data assimilation with a nonlinear quasi-geostrophic model using monte carlo methods to forecast error statistics. *Journal of Geophysical Research: Oceans*, **99 (C5)**, 10 143–10 162.

Fiedler, F., and H. A. Panofsky, 1970: Atmospheric Scales and Spectral Gaps. *Bulletin of the American Meteorological Society*, **51 (12)**, 1114–1120, doi:10.1175/1520-0477(1970)051⟨1114:ASASG⟩2.0.CO;2.

Franzke, C., T. Woollings, and O. Martius, 2011: Persistent circulation regimes and preferred regime transitions in the north atlantic. *Journal of the atmospheric sciences*, **68 (12)**, 2809–2825.

Gabriel, A., and D. Peters, 2008: A diagnostic study of different types of rossby wave breaking events in the northern extratropics. *Journal of the Meteorological Society of Japan. Ser. II*, **86 (5)**, 613–631.

Gage, K., 1979: Evidence far ak- 5/3 law inertial range in mesoscale two-dimensional turbulence. *Journal of the Atmospheric Sciences*, **36 (10)**, 1950–1954.

Gajanan, M., 2019: 21 people died of the cold during the polar vortex, showing just how dangerous it was. Time, URL http://time.com/5518469/21-people-died-cold-polar-vortex/.

Geerts, B., and Coauthors, 2017: The 2015 plains elevated convection at night field project. *Bulletin of the American Meteorological Society*, **98 (4)**, 767–786.

Giannakaki, P., and O. Martius, 2016: An object-based forecast verification tool for synoptic-scale rossby waveguides. *Weather and Forecasting*, **31 (3)**, 937–946.

Gkioulekas, E., 2006: A theoretical study of the cascades of 3d, 2d, and qg turbulence.

Grams, C. M., L. Magnusson, and E. Madonna, 2018: An atmospheric dynamics perspective on the amplification and propagation of forecast error in numerical weather prediction models: A case study. *Quarterly Journal of the Royal Meteorological Society*, **144 (717)**, 2577–2591.

Gray, S. L., C. Dunning, J. Methven, G. Masato, and J. M. Chagnon, 2014: Systematic model forecast error in rossby wave structure. *Geophysical Research Letters*, **41 (8)**, 2979–2987.

Grazzini, F., and L. Isaksen, 2002: North american increments. *ECMWF OD/RD Memo*.

Grazzini, F., and F. Vitart, 2015: Atmospheric predictability and rossby wave packets. *Quarterly Journal of the Royal Meteorological Society*.

Grell, G. A., J. Dudhia, D. R. Stauffer, and Coauthors, 1994: A description of the fifth-generation penn state/ncar mesoscale model (mm5).

Hakim, G. J., 2000: Climatology of coherent structures on the extratropical tropopause. *Monthly weather review*, **128 (2)**, 385–406.

Hakim, G. J., 2005: Vertical structure of midlatitude analysis and forecast errors. *Monthly weather review*, **133 (3)**, 567–578.

Hakim, G. J., and A. K. Canavan, 2005: Observed cyclone–anticyclone tropopause vortex asymmetries. *Journal of the atmospheric sciences*, **62 (1)**, 231–240.

Harr, P. A., and R. L. Elsberry, 2000: Extratropical transition of tropical cyclones over the western north pacific. part i: Evolution of structural characteristics during the transition process. *Monthly Weather Review*, **128 (8)**, 2613–2633.

Haurwitz, B., 1940: The motion of atmospheric disturbances on the spherical earth. *J. mar. Res*, **3 (5)**, 254–267.

Held, I. M., 1983: Stationary and quasi-stationary eddies in the extratropical troposphere: Theory. Citeseer, 127–168 pp.

Held, I. M., and A. Y. Hou, 1980: Nonlinear axially symmetric circulations in a nearly inviscid atmosphere. *Journal of the Atmospheric Sciences*, **37 (3)**, 515–533.

Henry, W., 1979: Some aspects of the fate of cold fronts in the gulf of mexico. *Monthly Weather Review*, **107 (8)**, 1078–1082.

Holton, J. R., 1976: A semi-spectral numerical model for wave-mean flow interactions in the stratosphere: Application to sudden stratospheric warmings. *Journal of the Atmospheric Sciences*, **33 (8)**, 1639–1649.

Hong, S.-Y., and H.-L. Pan, 1996: Nonlocal boundary layer vertical diffusion in a medium-range forecast model. *Monthly weather review*, **124 (10)**, 2322–2339.

Hopson, T., 2014: Assessing the ensemble spread–error relationship. *Monthly Weather Review*, **142 (3)**, 1125–1142.

Hoskins, B. J., and T. Ambrizzi, 1993: Rossby Wave Propagation on a Realistic Longitudinally Varying Flow. *Journal of the Atmospheric Sciences*, **50 (12)**, 1661–1671, doi:10.1175/1520-0469(1993)050⟨1661:RWPOAR⟩2.0.CO;2.

Hoskins, B. J., and D. J. Karoly, 1981: The Steady Linear Response of a Spherical Atmosphere to Thermal and Orographic Forcing. *Journal of the Atmospheric Sciences*, **38 (6)**, 1179–1196, doi:10.1175/1520-0469(1981)038⟨1179:TSLROA⟩2.0.CO;2.

Hoskins, B. J., M. McIntyre, and A. W. Robertson, 1985: On the use and significance of isentropic potential vorticity maps. *Quarterly Journal of the Royal Meteorological Society*, **111 (470)**, 877–946.

Iacono, M. J., J. S. Delamere, E. J. Mlawer, M. W. Shephard, S. A. Clough, and W. D. Collins, 2008: Radiative forcing by long-lived greenhouse gases: Calculations with the aer radiative transfer models. *Journal of Geophysical Research: Atmospheres*, **113 (D13)**.

Jin, F., L. Pan, and M. Watanabe, 2006a: Dynamics of synoptic eddy and low-frequency flow interaction. part i: A linear closure. *Journal of the atmospheric sciences*, **63 (7)**, 1677–1694.

Jin, F., L. Pan, and M. Watanabe, 2006b: Dynamics of synoptic eddy and low-frequency flow interaction. part ii: A theory for low-frequency modes. *Journal of the atmospheric sciences*, **63 (7)**, 1695–1708.

Jones, S. C., and Coauthors, 2003: The Extratropical Transition of Tropical Cyclones: Forecast Challenges, Current Understanding, and Future Directions. *Weather and Forecasting*, **18 (6)**, 1052–1092, doi:10.1175/1520-0434(2003)018⟨1052:TETOTC⟩2.0.CO;2.

Judt, F., 2018: Insights into atmospheric predictability through global convection-permitting model simulations. *Journal of the Atmospheric Sciences*, **75 (5)**, 1477–1497.

Jung, T., M. A. Kasper, T. Semmler, and S. Serrar, 2014: Arctic influence on subseasonal midlatitude prediction. *Geophysical Research Letters*, **41 (10)**, 3676–3680.

Kiladis, G. N., and S. B. Feldstein, 1994: Rossby wave propagation into the tropics in two gfdl general circulation models. *Climate dynamics*, **9 (4)**, 245–252.

Klemp, J. B., 2011: A terrain-following coordinate with smoothed coordinate surfaces. *Monthly weather review*, **139 (7)**, 2163–2169.

Kolmogorov, A. N., 1941: The local structure of turbulence in incompressible viscous fluid for very large reynolds numbers. *Dokl. Akad. Nauk SSSR*, Vol. 30, 299–303.

Konrad, C. E., 1996: Relationships between the intensity of cold-air outbreaks and the evolution of synoptic and planetary-scale features over north america. *Monthly weather review*, **124 (6)**, 1067–1083.

Konrad, C. E., and S. J. Colucci, 1989: An examination of extreme cold air outbreaks over eastern north america. *Monthly Weather Review*, **117 (12)**, 2687–2700.

Konrad II, C. E., 1998: Persistent planetary scale circulation patterns and their relationship with cold air outbreak activity over the eastern united states. *International Journal of Climatology: A Journal of the Royal Meteorological Society*, **18 (11)**, 1209–1221.

Kraichnan, R. H., 1967: Inertial ranges in two-dimensional turbulence. *The Physics of Fluids*, **10 (7)**, 1417–1423.

Kunz, T., K. Fraedrich, and F. Lunkeit, 2009: Synoptic scale wave breaking and its potential to drive nao-like circulation dipoles: A simplified gcm approach. *Quarterly Journal of the Royal Meteorological Society: A journal of the atmospheric sciences, applied meteorology and physical oceanography*, **135 (638)**, 1–19.

Lambert, S., and P. Merilees, 1978: A study of planetary wave errors in a spectral numerical weather prediction model. *Atmosphere-Ocean*, **16 (2)**, 197–211, doi:10.1080/07055900.1978.9649027.

Lau, N.-C., and E. O. Holopainen, 1984: Transient eddy forcing of the time-mean flow as identified by geopotential tendencies. *Journal of the Atmospheric Sciences*, **41 (3)**, 313–328.

Lewis, J. M., and J. C. Derber, 1985: The use of adjoint equations to solve a variational adjustment problem with advective constraints. *Tellus A*, **37 (4)**, 309–322.

Li, J., and G. Wu, 2010: Atmospheric angular momentum transport and balance in the agcm-samil. *Advances in Atmospheric Sciences*, **27 (5)**, 1183–1192.

Lillo, S. P., S. M. Cavallo, D. B. Parsons, and C. Riedel, 2021: The role of a tropopause polar vortex outbreak in the generation of the january 2019 extreme arctic outbreak. *Journal of the atmospheric sciences*, **78**, accepted with minor revisions.

Lillo, S. P., and D. B. Parsons, 2017: Investigating the dynamics of error growth in ecmwf medium-range forecast busts. *Quarterly Journal of the Royal Meteorological Society*, **143 (704)**, 1211–1226.

Lillo, S. P., D. B. Parsons, and M. Peña, 2019: Dynamics behind a record-breaking trough over mexico and internal atmospheric variability during el niño. *Bulletin of the American Meteorological Society*, **(2019)**.

Lilly, D., and E. Petersen, 1983: Aircraft measurements of atmospheric kinetic energy spectra. *Tellus A*, **35 (5)**, 379–382.

Lindborg, E., 1999: Can the atmospheric kinetic energy spectrum be explained by two-dimensional turbulence? *Journal of Fluid Mechanics*, **388**, 259–288.

Ling, J., and C. Zhang, 2013: Diabatic heating profiles in recent global reanalyses. *Journal of Climate*, **26 (10)**, 3307–3325.

Lorenz, D. J., and D. L. Hartmann, 2003: Eddy–zonal flow feedback in the northern hemisphere winter. *Journal of climate*, **16 (8)**, 1212–1227.

Lorenz, E. N., 1963: Deterministic Nonperiodic Flow. *Journal of the Atmospheric Sciences*, **20 (2)**, 130–141, doi:10.1175/1520-0469(1963)020⟨0130:DNF⟩2.0.CO;2.

Lorenz, E. N., 1969: The predictability of a flow which possesses many scales of motion. *Tellus*, **21 (3)**, 289–307.

Lorenz, E. N., 1982: Atmospheric predictability experiments with a large numerical model. *Tellus*, **34 (6)**, 505–513.

Luna-Niño, R., and T. Cavazos, 2018: Formation of a coastal barrier jet in the gulf of mexico due to the interaction of cold fronts with the sierra madre oriental mountain range. *Quarterly Journal of the Royal Meteorological Society*, **144 (710)**, 115–128.

L'Heureux, M. L., and Coauthors, 2017: Observing and predicting the 2015/16 el niño. *Bulletin of the American Meteorological Society*, **98 (7)**, 1363–1382.

Madonna, E., M. Boettcher, C. M. Grams, H. Joos, O. Martius, and H. H Wernli, ????: Verification of north atlantic warm conveyor belt outflows in ecmwf forecasts. *Quarterly Journal of the Royal Meteorological Society*, **141 (689)**.

Magaña, V., and T. Ambrizzi, 2005: Dynamics of subtropical vertical motions over the americas during el niño boreal winters. *Atmósfera*, **18 (4)**, 211–235.

Magaña, V. O., J. L. Vázquez, J. L. Pérez, and J. B. Pérez, 2003: Impact of el niño on precipitation in mexico. *Geofísica internacional*, **42 (3)**, 313–330.

Mapes, B. E., and R. A. Houze Jr, 1995: Diabatic divergence profiles in western pacific mesoscale convective systems. *Journal of Atmospheric Sciences*, **52 (10)**, 1807–1828.

Martínez-Alvarado, O., E. Madonna, S. L. Gray, and H. Joos, 2016: A route to systematic error in forecasts of rossby waves. *Quarterly Journal of the Royal Meteorological Society*, **142 (694)**, 196–210.

Massey, F. J., 1951: The Kolmogorov-Smirnov test for goodness of fit. *Journal of the American statistical Association*, **46 (253)**, 68–78.

Matsuno, T., 1970: Vertical propagation of stationary planetary waves in the winter northern hemisphere. *Journal of the atmospheric sciences*, **27 (6)**, 871–883.

McAvaney, B. J., W. Bourke, and K. Puri, 1978: A Global Spectral Model for Simulation of the General Circulation. *Journal of the Atmospheric Sciences*, **35 (9)**, 1557–1583, doi:10.1175/1520-0469(1978)035⟨1557:AGSMFS⟩2.0.CO;2.

Melhauser, C., and F. Zhang, 2012: Practical and intrinsic predictability of severe and convective weather at the mesoscales. *Journal of the Atmospheric Sciences*, **69 (11)**, 3350–3371.

Mesinger, F., and Coauthors, 2006: North american regional reanalysis. *Bulletin of the American Meteorological Society*, **87 (3)**, 343–360.

Michel, C., and G. Rivière, 2011: The link between rossby wave breakings and weather regime transitions. *Journal of the Atmospheric Sciences*, **68 (8)**, 1730–1748.

Miller, K. A., and M. W. Downton, 1993: The freeze risk to florida citrus. part 1: Investment decisions. *Journal of Climate*, **6 (2)**, 354–363.

Morgan, M. C., and J. W. Nielsen-Gammon, 1998: Using tropopause maps to diagnose midlatitude weather systems. *Monthly weather review*, **126 (10)**, 2555–2579.

Myrick, D., 2017: Global forecast systems (gfs) upgrade: Effective july 19, 2017. Tech. rep., National Centers for Environmental Prediction, National Weather Service, NOAA, U.S. Department of Commerce.

Nastrom, G., and K. Gage, 1983: A first look at wavenumber spectra from gasp data. *Tellus A*, **35 (5)**, 383–388.

Nastrom, G., K. Gage, and W. Jasperson, 1984: Kinetic energy spectrum of large-and mesoscale atmospheric processes. *Nature*, **310 (5972)**, 36.

Nastrom, G., and K. S. Gage, 1985: A climatology of atmospheric wavenumber spectra of wind and temperature observed by commercial aircraft. *Journal of the atmospheric sciences*, **42 (9)**, 950–960.

Newman, M., G. P. Compo, and M. A. Alexander, 2003: Enso-forced variability of the pacific decadal oscillation. *Journal of Climate*, **16 (23)**, 3853–3857.

Ngan, K., and G. Eperon, 2012: Middle atmosphere predictability in a numerical weather prediction model: Revisiting the inverse error cascade. *Quarterly Journal of the Royal Meteorological Society*, **138 (666)**, 1366–1378.

Nielsen-Gammon, J. W., and D. A. Gold, 2008: Potential vorticity diagnosis of the severe convective regime. part ii: The impact of idealized pv anomalies. *Monthly weather review*, **136 (5)**, 1582–1592.

NWS, 2019: January 30-31, 2019: Record to near-record cold in northern illinois. NOAA's National Weather Service, URL https://www.weather.gov/lot/RecordColdJan2019.

Obukhov, A., 1949: The local structure of atmospheric turbulence. *Dokl. Akad. Nauk. SSSR*, Vol. 67, 643–646.

Oort, A. H., and J. J. Yienger, 1996: Observed interannual variability in the hadley circulation and its connection to enso. *Journal of Climate*, **9 (11)**, 2751–2767.

O'Rourke, A. K., and G. K. Vallis, 2016: Meridional rossby wave generation and propagation in the maintenance of the wintertime tropospheric double jet. *Journal of the Atmospheric Sciences*, **73 (5)**, 2179–2201.

Palmer, C. E., 1959: The stratospheric polar vortex in winter. *Journal of Geophysical Research*, **64 (7)**, 749–764.

Papritz, L., E. Rouges, F. Aemisegger, and H. Wernli, 2019: On the thermodynamic preconditioning of arctic air masses and the role of tropopause polar vortices for cold air outbreaks from fram strait. *Journal of Geophysical Research: Atmospheres*, **124 (21)**, 11 033–11 050.

Parsons, D. B., S. P. Lillo, C. P. Rattray, P. Bechtold, M. J. Rodwell, and C. M. Bruce, 2019a: The role of continental mesoscale convective systems in forecast busts within global weather prediction system. *Atmosphere*, **10 (11)**, 681.

Parsons, D. B., S. P. Lillo, C. P. Rattray, P. Bechtold, M. J. Rodwell, and C. M. Bruce, 2019b: The role of continental mesoscale convective systems in forecast busts within global weather prediction systems. *Atmosphere*, **10 (11)**, 681.

Pedlosky, J., 1998: *Geophysical Fluid Dynamics*, Vol. 84. 2nd ed., Springer, 728 pp.

Pérez, E. P., V. Magaña, E. Caetano, and S. Kusunoki, 2014: Cold surge activity over the gulf of mexico in a warmer climate1. *Frontiers in Earth Science*, **2**, 19.

Peterson, W., M. Robert, and N. Bond, 2015: The warm blob continues to dominate the ecosystem of the northern california current. *PICES Press*, **23 (2)**, 44.

Plumb, R. A., 1985: On the three-dimensional propagation of stationary waves. *Journal of the Atmospheric Sciences*, **42 (3)**, 217–229.

Pope, S. B., and S. B. Pope, 2000: *Turbulent flows*. Cambridge university press.

Provenzale, A., 1999: Transport by coherent barotropic vortices. *Annual review of fluid mechanics*, **31 (1)**, 55–93.

Pyle, M. E., D. Keyser, and L. F. Bosart, 2004: A diagnostic study of jet streaks: Kinematic signatures and relationship to coherent tropopause disturbances. *Monthly weather review*, **132 (1)**, 297–319.

Quan, X.-W., M. Hoerling, L. Smith, J. Perlwitz, T. Zhang, A. Hoell, K. Wolter, and J. Eischeid, 2018: Extreme california rains during winter 2015/16: A change in el niño teleconnection? *Bulletin of the American Meteorological Society*, **99 (1)**, S49–S53.

Rabier, F., and Z. Liu, 2003: Variational data assimilation: theory and overview. *Proc. ECMWF Seminar on Recent Developments in Data Assimilation for Atmosphere and Ocean, Reading, UK, September 8–12*, 29–43.

Reding, P. J., 1992: The central american cold surge: An observational analysis of the deep southward penetration of north american cold fronts. Tech. rep., TEXAS A AND M UNIV COLLEGE STATION.

Ren, H.-L., F.-F. Jin, J.-S. Kug, and L. Gao, 2011: Transformed eddy-pv flux and positive synoptic eddy feedback onto low-frequency flow. *Climate dynamics*, **36 (11-12)**, 2357–2370.

Ren, H.-L., F.-F. Jin, J.-S. Kug, J.-X. Zhao, and J. Park, 2009: A kinematic mechanism for positive feedback between synoptic eddies and nao. *Geophysical Research Letters*, **36 (11)**.

Richardson, L. F., 1922: *Weather prediction by numerical process*. Cambridge University Press, URL https://archive.org/details/weatherpredictio00richrich.

Riemer, M., and S. C. Jones, 2010: The downstream impact of tropical cyclones on a developing baroclinic wave in idealized scenarios of extratropical transition. *Quarterly Journal of the Royal Meteorological Society*, **136 (648)**, 617–637.

Riemer, M., S. C. Jones, and C. A. Davis, 2008: The impact of extratropical transition on the downstream flow: An idealized modelling study with a straight jet. *Quarterly Journal of the Royal Meteorological Society: A journal of the atmospheric sciences, applied meteorology and physical oceanography*, **134 (630)**, 69–91.

Rivière, G., and I. Orlanski, 2007: Characteristics of the atlantic storm-track eddy activity and its relation with the north atlantic oscillation. *Journal of the Atmospheric Sciences*, **64 (2)**, 241–266.

Rodwell, M. J., D. S. Richardson, D. B. Parsons, and H. Wernli, 2018: Flow-dependent reliability: A path to more skillful ensemble forecasts. *Bulletin of the American Meteorological Society*, **99 (5)**, 1015–1026.

Rodwell, M. J., and Coauthors, 2012: A case study of occasional poor medium-range forecasts for Europe. 16–24.

Rodwell, M. J., and Coauthors, 2013: Characteristics of Occasional Poor Medium-Range Weather Forecasts for Europe. *Bulletin of the American Meteorological Society*, **94 (9)**, 1393–1405, doi:10.1175/BAMS-D-12-00099.1.

Rogers, J. C., and R. V. Rohli, 1991: Florida citrus freezes and polar anticyclones in the great plains. *Journal of Climate*, **4 (11)**, 1103–1113.

Ropelewski, C. F., and M. S. Halpert, 1987: Global and regional scale precipitation patterns associated with the el niño/southern oscillation. *Monthly weather review*, **115 (8)**, 1606–1626.

Rosen, R. D., D. A. Salstein, T. M. Eubanks, J. O. Dickey, and J. A. Steppe, 1984: An el nino signal in atmospheric angular momentum and earth rotation. *Science*, **225 (4660)**, 411–414.

Rossby, C.-G., 1939: Relation between variations in the intensity of the zonal circulation of the atmosphere and the displacements of the semi-permanent centers of action. *J. mar. Res.*, **2**, 38–55.

Rotunno, R., and C. Snyder, 2008: A generalization of lorenz's model for the predictability of flows with many scales of motion. *Journal of the Atmospheric Sciences*, **65 (3)**, 1063–1076.

Sanders, F., and J. R. Gyakum, 1980: Synoptic-dynamic climatology of the "bomb". *Monthly Weather Review*, **108 (10)**, 1589–1606.

Santoso, A., M. J. Mcphaden, and W. Cai, 2017: The defining characteristics of enso extremes and the strong 2015/2016 el niño. *Reviews of Geophysics*, **55 (4)**, 1079–1129.

Sardeshmukh, P. D., and B. J. Hoskins, 1988: The generation of global rotational flow by steady idealized tropical divergence. *Journal of the Atmospheric Sciences*, **45 (7)**, 1228–1251.

Schaefer, J., and R. Edwards, 1999: The spc tornado/severe thunderstorm database. *Preprints, 11th Conf. on Applied Climatology, Dallas, TX, Amer. Meteor. Soc*, Vol. 6.

Schäfler, A., and Coauthors, 2018: The north atlantic waveguide and downstream impact experiment. *Bulletin of the American Meteorological Society*, **99 (8)**, 1607–1637.

Scherrer, S. C., C. Appenzeller, P. Eckert, and D. Cattani, 2004: Analysis of the spread–skill relations using the ecmwf ensemble prediction system over europe. *Weather and Forecasting*, **19 (3)**, 552–565.

Schultz, D. M., W. E. Bracken, and L. F. Bosart, 1998: Planetary-and synoptic-scale signatures associated with central american cold surges. *Monthly Weather Review*, **126 (1)**, 5–27.

Schultz, D. M., W. E. Bracken, L. F. Bosart, G. J. Hakim, M. A. Bedrick, M. J. Dickinson, and K. R. Tyle, 1997: The 1993 superstorm cold surge: Frontal structure, gap flow, and tropical impact. *Monthly Weather Review*, **125 (1)**, 5–39.

Schwierz, C., S. Dirren, and H. C. Davies, 2004: Forced waves on a zonally aligned jet stream. *Journal of the atmospheric sciences*, **61 (1)**, 73–87.

Screen, J. A., C. Deser, and L. Sun, 2015: Reduced risk of north american cold extremes due to continued arctic sea ice loss. *Bulletin of the American Meteorological Society*, **96 (9)**, 1489–1503.

Selz, T., and G. C. Craig, 2015: Upscale error growth in a high-resolution simulation of a summertime weather event over europe. *Monthly Weather Review*, **143 (3)**, 813–827.

Shapiro, M., T. Hampel, and A. Krueger, 1987: The arctic tropopause fold. *Monthly Weather Review*, **115 (2)**, 444–454.

Shapiro, M., and Coauthors, 2010: An earth-system prediction initiative for the twenty-first century. *Bulletin of the American Meteorological Society*, **91 (2010)**, 1377–1388.

Shapiro, M. A., and A. J. Thorpe, 2004: Thorpex international science plan. *WMO/TD*, **1246**.

Shuman, F. G., 1989: History of Numerical Weather Prediction at the National Meteorological Center. *Weather and Forecasting*, **4 (3)**, 286–296, doi:10.1175/1520-0434(1989)004⟨0286:HONWPA⟩2.0.CO;2.

Shuman, F. G., and J. B. Hovermale, 1968: An operational six-layer primitive equation model. *Journal of Applied Meteorology*, **7 (4)**, 525–547.

Simmons, A., R. Mureau, and T. Petroliagis, 1995: Error growth and estimates of predictability from the ecmwf forecasting system. *Quarterly Journal of the Royal Meteorological Society*, **121 (527)**, 1739–1771.

Skamarock, W. C., 2004: Evaluating mesoscale nwp models using kinetic energy spectra. *Monthly weather review*, **132 (12)**, 3019–3032.

Skamarock, W. C., J. B. Klemp, M. G. Duda, L. D. Fowler, S.-H. Park, and T. D. Ringler, 2012: A multiscale nonhydrostatic atmospheric model using centroidal voronoi tesselations and c-grid staggering. *Monthly Weather Review*, **140 (9)**, 3090–3105.

Stein, A., R. R. Draxler, G. D. Rolph, B. J. Stunder, M. Cohen, and F. Ngan, 2015: Noaa's hysplit atmospheric transport and dispersion modeling system. *Bulletin of the American Meteorological Society*, **96 (12)**, 2059–2077.

Stensrud, D. J., 1996: Effects of Persistent, Midlatitude Mesoscale Regions of Convection on the Large-Scale Environment during the Warm Season. *Journal of the Atmospheric Sciences*, **53 (23)**, 3503–3527, doi:10.1175/1520-0469(1996)053⟨3503:EOPMMR⟩2.0.CO;2.

Stensrud, D. J., 2013: Upscale Effects of Deep Convection during the North American Monsoon. *Journal of the Atmospheric Sciences*, **70 (9)**, 2681–2695, doi:10.1175/JAS-D-13-063.1.

Stensrud, D. J., and J. L. Anderson, 2001: Is Midlatitude Convection an Active or a Passive Player in Producing Global Circulation Patterns? *Journal of Climate*, **14 (10)**, 2222–2237, doi:10.1175/1520-0442(2001)014⟨2222:IMCAAO⟩2.0.CO;2.

Sun, Y. Q., and F. Zhang, 2016: Intrinsic versus practical limits of atmospheric predictability and the significance of the butterfly effect. *Journal of the Atmospheric Sciences*, **73 (3)**, 1419–1438.

Swinbank, R., and Coauthors, 2016: The tigge project and its achievement. *Bulletin of the American Meteorological Society*, **97 (1)**, 49–67.

Szapiro, N., and S. Cavallo, 2018: Tpvtrack v1. 0: a watershed segmentation and overlap correspondence method for tracking tropopause polar vortices. *Geoscientific Model Development*, **11 (12)**, 5173–5187.

Takaya, K., and H. Nakamura, 1997: A formulation of a wave-activity flux for stationary rossby waves on a zonally varying basic flow. *Geophysical research letters*, **24 (23)**, 2985–2988.

Takaya, K., and H. Nakamura, 2001a: A Formulation of a Phase-Independent Wave-Activity Flux for Stationary and Migratory Quasigeostrophic Eddies on a Zonally Varying Basic Flow. *Journal of the Atmospheric Sciences*, **58 (6)**, 608–627, doi:10.1175/1520-0469(2001)058⟨0608:AFOAPI⟩2.0.CO;2.

Takaya, K., and H. Nakamura, 2001b: A Formulation of a Phase-Independent Wave-Activity Flux for Stationary and Migratory Quasigeostrophic Eddies on a Zonally Varying Basic Flow. *Journal of the Atmospheric Sciences*, **58 (6)**, 608–627, doi:10.1175/1520-0469(2001)058⟨0608:AFOAPI⟩2.0.CO;2.

Takaya, K., and H. Nakamura, 2001c: A formulation of a phase-independent wave-activity flux for stationary and migratory quasigeostrophic eddies on a zonally varying basic flow. *Journal of the atmospheric sciences*, **58 (6)**, 608–627.

Teng, H., and G. Branstator, 2017: Causes of extreme ridges that induce california droughts. *Journal of Climate*, **30 (4)**, 1477–1492.

Teubler, F., and M. Riemer, 2016: Dynamics of rossby wave packets in a quantitative potential vorticity–potential temperature framework. *Journal of the Atmospheric Sciences*, **73 (3)**, 1063–1081.

Thompson, G., R. M. Rasmussen, and K. Manning, 2004: Explicit forecasts of winter precipitation using an improved bulk microphysics scheme. part i: Description and sensitivity analysis. *Monthly Weather Review*, **132 (2)**, 519–542.

Thorncroft, C. D., B. J. Hoskins, and M. E. McIntyre, 1993: Two paradigms of baroclinic-wave life-cycle behaviour. *Quarterly Journal of the Royal Meteorological Society*, **119 (509)**, 17–55, doi:10.1002/qj.49711950903.

Thorpe, A. J., 1985: Diagnosis of balanced vortex structure using potential vorticity. **42 (4)**, 397–406.

Thorpe, A. J., 1986: Synoptic scale disturbances with circular symmetry. **114 (7)**, 1384–1389.

Thorpe, A. J., 2004: Weather forecasting: A centenary perspective. *Weather*, **59 (12)**, 332–335.

Tiedtke, M., 1989: A comprehensive mass flux scheme for cumulus parameterization in large-scale models. *Monthly Weather Review*, **117 (8)**, 1779–1800.

Tribbia, J., and D. Baumhefner, 2004: Scale interactions and atmospheric predictability: An updated perspective. *Monthly weather review*, **132 (3)**, 703–713.

Tulloch, R., and K. Smith, 2006: A theory for the atmospheric energy spectrum: Depth-limited temperature anomalies at the tropopause. *Proceedings of the National Academy of Sciences*, **103 (40)**, 14 690–14 694.

Tung, K. K., and W. W. Orlando, 2003: The k- 3 and k- 5/3 energy spectrum of atmospheric turbulence: Quasigeostrophic two-level model simulation. *Journal of the atmospheric sciences*, **60 (6)**, 824–835.

Uccellini, L. W., 2016: Service assessment: The historic nor'easter of january 2016.

Vavrus, S., J. Walsh, W. Chapman, and D. Portis, 2006: The behavior of extreme cold air outbreaks under greenhouse warming. *International Journal of Climatology: A Journal of the Royal Meteorological Society*, **26 (9)**, 1133–1147.

Vinnichenko, N. K., 1970: The kinetic energy spectrum in the free atmosphere-1 second to 5 years. *Tellus*, **22 (2)**, 158–166, doi:10.1111/j.2153-3490.1970.tb01517.x.

Wallace, J. M., and D. S. Gutzler, 1981: Teleconnections in the geopotential height field during the northern hemisphere winter. *Monthly Weather Review*, **109 (4)**, 784–812.

Walsh, J. E., A. S. Phillips, D. H. Portis, and W. L. Chapman, 2001: Extreme cold outbreaks in the united states and europe, 1948–99. *Journal of Climate*, **14 (12)**, 2642–2658.

Wandishin, M. S., J. W. Nielsen-Gammon, and D. Keyser, 2000: A potential vorticity diagnostic approach to upper-level frontogenesis within a developing baroclinic wave. *Journal of the atmospheric sciences*, **57 (24)**, 3918–3938.

Waugh, D. W., A. H. Sobel, and L. M. Polvani, 2017: What is the polar vortex and how does it influence weather? *Bulletin of the American Meteorological Society*, **98 (1)**, 37–44.

Wheeler, D., V. Harvey, D. Atkinson, R. Collins, and M. Mills, 2011: A climatology of cold air outbreaks over north america: Waccm and era-40 comparison and analysis. *Journal of Geophysical Research: Atmospheres*, **116 (D12)**.

Whitaker, J. S., and A. F. Loughe, 1998: The relationship between ensemble spread and ensemble mean skill. *Monthly weather review*, **126 (12)**, 3292–3302.

Wilks, D. S., 2006: *Statistical methods in the atmopsheric sciences*. 2nd ed., Academic Press, 627 pp.

Winters, A. C., D. Keyser, L. F. Bosart, and J. E. Martin, 2020: Composite Synoptic-Scale Environments Conducive to North American Polar–Subtropical Jet Superposition Events. *Monthly Weather Review*, **148 (5)**, 1987–2008.

Winters, A. C., and J. E. Martin, 2017: Diagnosis of a north american polar–subtropical jet superposition employing piecewise potential vorticity inversion. *Monthly Weather Review*, **145 (5)**, 1853–1873.

Wirth, V., and J. Eichhorn, 2014: Long-lived rossby wave trains as precursors to strong winter cyclones over europe. *Quarterly Journal of the Royal Meteorological Society*, **140 (680)**, 729–737.

Wirth, V., M. Riemer, E. K. Chang, and O. Martius, 2018: Rossby wave packets on the midlatitude waveguide—a review. *Monthly Weather Review*, **(2018)**.

Wolf, G., and V. Wirth, 2017: Diagnosing the horizontal propagation of rossby wave packets along the midlatitude waveguide. *Monthly Weather Review*, **145 (8)**, 3247–3264.

Woollings, T., and Coauthors, 2018: Blocking and its response to climate change. *Current Climate Change Reports*, **4 (3)**, 287–300.

Zhang, C., Y. Wang, and K. Hamilton, 2011: Improved representation of boundary layer clouds over the southeast pacific in arw-wrf using a modified tiedtke cumulus parameterization scheme. *Monthly Weather Review*, **139 (11)**, 3489–3513.

Zhang, F., N. Bei, R. Rotunno, C. Snyder, and C. C. Epifanio, 2007a: Mesoscale predictability of moist baroclinic waves: Convection-permitting experiments and multistage error growth dynamics. *Journal of the Atmospheric Sciences*, **64 (10)**, 3579–3594.

Zhang, F., C. Snyder, and R. Rotunno, 2002: Mesoscale predictability of the "surprise" snowstorm of 24–25 january 2000. *Monthly Weather Review*, **130 (6)**, 1617–1632.

Zhang, F., C. Snyder, and R. Rotunno, 2003: Effects of moist convection on mesoscale predictability. **60**, 1173–1185.

Zhang, H., G. M. McFarquhar, S. M. Saleeby, and W. R. Cotton, 2007b: Impacts of {Saharan} dust as {CCN} on the evolution of an idealized tropical cyclone. **34**, doi: 10.1029/2007GL029876.

Zheng, M., 2016: *Growth of Errors and Uncertainties in Medium Range Ensemble Forecasts of US East Coast Cool Season Extratropical Cyclones*.

Zuo, J., H.-L. Ren, J. Wu, Y. Nie, and Q. Li, 2016: Subseasonal variability and predictability of the arctic oscillation/north atlantic oscillation in bcc_agcm2. 2. *Dynamics of Atmospheres and Oceans*, **75**, 33–45.